



HAL
open science

Cellular structures for shape morphing

Maïka Saint-Jean

► **To cite this version:**

Maïka Saint-Jean. Cellular structures for shape morphing. Mechanics of materials [physics.class-ph]. Université Paris sciences et lettres, 2022. English. NNT : 2022UPSLS058 . tel-04064246

HAL Id: tel-04064246

<https://pastel.hal.science/tel-04064246>

Submitted on 11 Apr 2023

HAL is a multi-disciplinary open access archive for the deposit and dissemination of scientific research documents, whether they are published or not. The documents may come from teaching and research institutions in France or abroad, or from public or private research centers.

L'archive ouverte pluridisciplinaire **HAL**, est destinée au dépôt et à la diffusion de documents scientifiques de niveau recherche, publiés ou non, émanant des établissements d'enseignement et de recherche français ou étrangers, des laboratoires publics ou privés.



THÈSE DE DOCTORAT

DE L'UNIVERSITÉ PSL

Préparée au laboratoire PMMH,
Physique et Mécanique des Milieux Hétérogènes
ESPCI

Structures cellulaires à changement de forme
Cellular structures for shape morphing

Soutenue par

Maïka Saint-Jean

Le 8 décembre 2022

École doctorale n°564

Physique en Île-de-France

Spécialité

Physique

Composition du jury :

Matteo CICOTTI Professeur, ESPCI	<i>Président du jury</i>
Dominic VELLA Professeur, Université d'Oxford	<i>Rapporteur</i>
Catherine QUILLIET Maître de conférence, Université Grenoble Alpes	<i>Rapporteuse</i>
Sébastien NEUKIRCH Directeur de recherche, Sorbonne Université	<i>Examineur</i>
Sophie RAMANANARIVO Assistant professeur, Polytechnique	<i>Examinatrice</i>
Etienne REYSSAT Chargé de recherche, ESPCI	<i>Directeur de thèse</i>
José BICO Maître de conférence, ESPCI	<i>Co-directeur de thèse</i>
Benoît ROMAN Directeur de recherche, ESPCI	<i>Co-encadrant de thèse</i>

Merci !

Je ne suis pas très douée pour les remerciements mais je vais essayer de n'oublier personne, après plus de trois ans au PMMH cela fait beaucoup de monde à remercier! Merci à tous les gens que j'ai croisé de près ou de loin au cours de cette thèse pour avoir fait de ces trois ans de thèse - qui peuvent être long ou court suivant les jours - une super expérience pour moi. Avec l'arrivée de la pandémie ce n'était pas gagné mais votre accompagnement m'a permis de m'épanouir au cours de ces dernières années.

J'aimerais commencer par remercier l'AID pour le demi financement qui m'a permis de réaliser cette thèse et Marie-Christine Saint-Catherine qui m'a suivi du côté de l'AID. Je souhaiterais ensuite remercier mon jury sans qui le titre de docteur n'aurait pu m'être remis. Mes deux rapporteurs Dominic Vella et Catherine Quilliet qui ont eu la gentillesse de lire mon manuscrit et me faire remonter des remarques pertinentes. Mes examinateurs Matteo Cicotti, Sébastien Neukirch et Sophie Ramanarivo pour avoir écouté ma soutenance et permis une discussion enrichissante. Merci aussi Sébastien pour tes corrections détaillées et les discussions du modèle mécanique. Je souhaiterais aussi remercier les jurys invités: Marie-Christine Sainte-Catherine et Alessandro Benedetto.

Ce travail de thèse n'aurait pas pu se faire sans l'aide et l'encadrement du laboratoire. Merci d'abord à mes encadrants de thèse pour leur accompagnement et leur soutien pendant ces trois années de thèse malheureusement ponctuées par la pandémie: Etienne merci de m'avoir laissée être ta première « vraie » doctorante avec ton HDR fraîchement empochée, merci pour toutes ces relectures (de document que je n'envoyais pas toujours très en avance) et toutes nos discussions. José merci de m'avoir initialement laissée entrer dans l'équipe Mecawet pour mon stage de 1A et pour les discussions autour de la vie et de la science. Enfin merci Benoît pour toute ces discussions et tes petits coup de pousse avec toujours de nouvelles références, nouvelles vidéos et astuces surtout sur les imprimantes 3D et pour tes gâteaux au citron bergamote. Merci aussi pour les différentes collaborations auquel j'ai pu prendre part. Thanks Hillel for all the discussions and your precious help on the diamond project. Thanks Tom for the interesting Monday discussion and the tour of the lab. Merci Pierre-Brice pour la collaboration sur les "bullomorphes". Thanks Yasaman and Tiffany for the discussion about curve foldings. Thanks Noga, Ofri and Arielle for the help on the "negative pressure" project. Mais l'encadrement d'une thèse ne comprend pas que l'accompagnement scientifique : merci Fred et Claudette de vous occuper si bien de toute la partie administrative des commandes et des missions (même quand les demandes ne sont pas fait très en avance), merci Philippe et Damien pour tout ce que vous faites pour le laboratoire, merci Damien pour ta patience et ton aide sur les films de savons. Merci aussi à l'atelier pour leur aide. Merci aussi à mon comité de suivi de thèse qui m'a été suivi durant ces trois ans: Antonin Eddi et Costantino Creton.

Le bon déroulement d'une thèse passe aussi par les gens côtoyés au quotidien. Merci à tous les non permanents passés et actuels qui font que le PMMH est un lieu si accueillant et agréable pour toutes les nouvelles recrues (merci aussi aux permanents qui y contribuent aussi!). Merci d'abord à toute l'équipe Mecawet passée et présente : Hadrien, Marie et Ludo vous m'avez tout d'abord accueillie en stage de 1A et donné envie de revenir en thèse quelques années plus tard. Manu merci de m'avoir encouragée à venir dans l'équipe et de m'avoir initiée aux matériaux qui changent de forme, merci aussi pour tes conseils même quand tu avais quitté le labo et tes talents de pâtissier. Manon merci de m'avoir intégrée dès le début dans le laboratoire et merci pour l'énergie que tu apportais à l'équipe. Tian thank you for these 3 years of PHD, always sharing new ideas and cultural knowledge. Pierre-Brice merci pour ces gâteaux trop peu nombreux et ces discussions autour des films de savon. Merci Maud (ou Manonb bis ?) pour avoir pris la suite de Manon et avoir continué à répandre de la bonne humeur dans l'équipe, maintenant c'est toi la 'vieille' du groupe (le téléphone est tout à toi). Gracias Alejandro for your help on many technical issues (unfortunately I did not take time to improve my Spanish). Merci aussi aux 3 nouvelles recrues Antoine, Joo-won et Nathan pour votre aide dans les dernières préparations de thèse.

Merci aux Biomim chez qui je suis souvent passée pendant mes pauses. Merci Roméo pour les discussions de science et pâtisserie (tu me dois pas encore un gâteau ?). Merci à l'armée de nouveaux Biomim qui a suivi, Baptiste, Gatien et Tristan de m'avoir partagé vos expériences quand j'avais besoin de pause, j'essayerai de continuer à passer pour vérifier que ça avance. Merci Camille pour les discussions pâtisseries et autres sucreries ainsi que les dégustations. Merci à toute la vague de doctorants qui a commencé sa thèse avec moi: Mathieu, Zhibo, Cholé merci de t'être si bien occupée des doctorants pour faire du PMMH un super laboratoire, Manon j'ai passé un super moment à Chicago, Sébastien merci pour ses discussions pendant la rédaction qui te faisait rentrer trop tard pour trouver un franprix ouvert, Magda thanks for the discussion at lunch and the sharing about Polish culture, Lars thanks for the sharing about 3D printer, Mousse merci pour les discussions autour des nouveaux jeux et énigme du jour. Merci aux membres de mon bureau Mousse, Chloé, Baptiste, Alinéor, Joseph de m'avoir gardé une place fantôme, j'espère que le prochain occupant sera plus présent. Merci aux nombreux membres de la team Crous avec qui j'ai pu partager de nombreux midis, ces repas vont me manquer. Une pensée à Matthias qui a tenté de me faire arriver plus tôt au laboratoire sans grand succès et qui m'a transmis le template de ce manuscrit. Merci Valentin pour ces discussions (et d'accepter que j'ai très souvent raison). Merci au « club aquarelle » et toi Fred qui le fait vivre, cela m'a permis de me détendre en période de rédaction, j'espère que je pourrais repasser de temps en temps.

Merci Marion pour toutes ces discussions et échanges de tips sur la thèse, il va maintenant falloir que je trouve une autre binôme. Merci à la team coin coin/cinéma : Marine, Suzy pour toutes les sorties cinéma/pizza (on va finir par pouvoir faire cet escape game !). Merci Lisa et Gregoire. Merci aussi à toute ma famille qui m'a soutenue au cours ces 3 ans et qui j'espère a compris un peu mieux ma thèse après ma soutenance. Merci Maman pour toutes les préparations du pot. Merci Nahia pour toutes nos discussions. Enfin merci Rodrigue d'avoir été là tout du long, pour avoir écouté toutes mes histoires, avoir fait un détour tous les matins pour m'accompagner et aidé quand la rédaction n'avancait pas.

Je finirais par dire une dernière fois merci à tous les gens que j'ai côtoyés pendant ma thèse sans qui l'expérience aurait été pas été aussi enrichissante en espérant tous continuer à vous revoir.

Table of contents

General introduction	1
Résumé français	5
0.1 Changement de forme par changement de phase	5
0.2 Changement de forme par fermeture de structures cellulaires	7
0.3 Sculpter des films de savons	9
1 Introduction to shape morphing	11
1.1 Geometry and morphing	11
1.1.1 Bi-layer effect	12
1.1.2 Geometry of surface shaping	15
1.1.2.a Gauss' <i>theorema egregium</i>	15
1.1.2.b Metrics changing strategies	17
1.2 Active shape changing due to internal mechanisms	19
1.3 Cellular structures for shape morphing	21
2 Untethered shape morphing by phase transition	23
2.1 Change shape with expanding material	24
2.2 Experimental set up	27
2.2.1 Preparation of the material	27
2.2.2 Adjusting the fabrication procedure	29
2.2.2.a Selecting a volatile liquid	29
2.2.2.b Mixing techniques	29
2.2.2.c Heating processes	30
2.2.3 From homogeneous expansion to shape-change: preparation of the samples	31
2.3 Lines and chevrons	32
2.3.1 From lines to chevrons	32
2.3.2 Mechanical properties of chevrons under traction	33
2.3.3 Parallel lines and aligned chevrons	38
2.3.3.a Influence of density d of the chevrons	39

Table of contents

2.3.3.b	Influence of angle θ on the strain	42
2.3.3.c	Influence of thickness t of the Mylar sheet	43
2.3.3.d	Effect of temperature	44
2.3.4	Programming 3D-shapes	46
2.4	Diamonds network	49
2.4.1	Network of aligned diamonds	50
2.4.2	3D-shapes	57
2.4.2.a	Logarithmic spirals	57
2.4.2.b	Continuous variation of the diamonds angle	61
2.5	Conclusion	63
3	Changing shape by closing cellular structures	65
3.1	Introduction	66
3.2	Fabrication process	67
3.2.1	3D printing of structures	67
3.2.2	Selecting the final angle: blocker mechanism	70
3.3	Programming with blockers	72
3.3.1	Aligned diamonds with different blockers	73
3.3.2	Axisymmetric actuation	74
3.3.3	General inverse problem	80
3.3.4	Programming the curvature	82
3.4	Mechanical properties of cellular plates	83
3.4.1	Mechanical properties under traction/compression	83
3.4.2	Mechanical properties: bending of cellular networks	89
3.5	Activation with vacuum	94
3.5.1	Network of aligned diamonds under vacuum	95
3.5.2	3D shapes with vacuum	100
3.6	Rectangular unit cells	103
3.6.1	3D shapes with angular sectors	104
3.6.2	3D shapes from logarithmic spirals	105
3.7	Conclusion	106
4	Sculpting soap films	109
4.1	Introduction	109
4.2	Unit cell and principle	111
4.2.1	Networks of aligned cells	112
4.2.1.a	Case of in plane deformation	113
4.2.1.b	Case of 3D deformation	114
4.2.1.c	Phase diagram and soap experiments	117

4.3	Deploying 3D structures	122
4.3.1	Aligned rectangles on a disk	122
4.3.1.a	Cells elongated along the radial direction	123
4.3.1.b	Rectangles elongated in the orthoradial direction	125
4.3.2	Logarithmic spirals	127
4.3.3	Influence of the curvature of “rectangular” cells	131
4.4	Other types of cells	134
4.5	Conclusion	135
 Conclusion		 137
 References		 141
 Appendix A Code for sample drawing		 149
A.1	Code for blockers	149
A.2	Code for axisymmetric case	150
A.2.1	Construction of logarithmic spiral	150
A.2.2	Algorithm axisymmetric shapes	151

General introduction

This PhD work is dedicated to the design, geometry and mechanics of shape-changing structures. There is currently a strong interest in the scientific community for "morphing" materials. It might be explained by the fact that this problem gathers questions that are now relevant for several different communities.

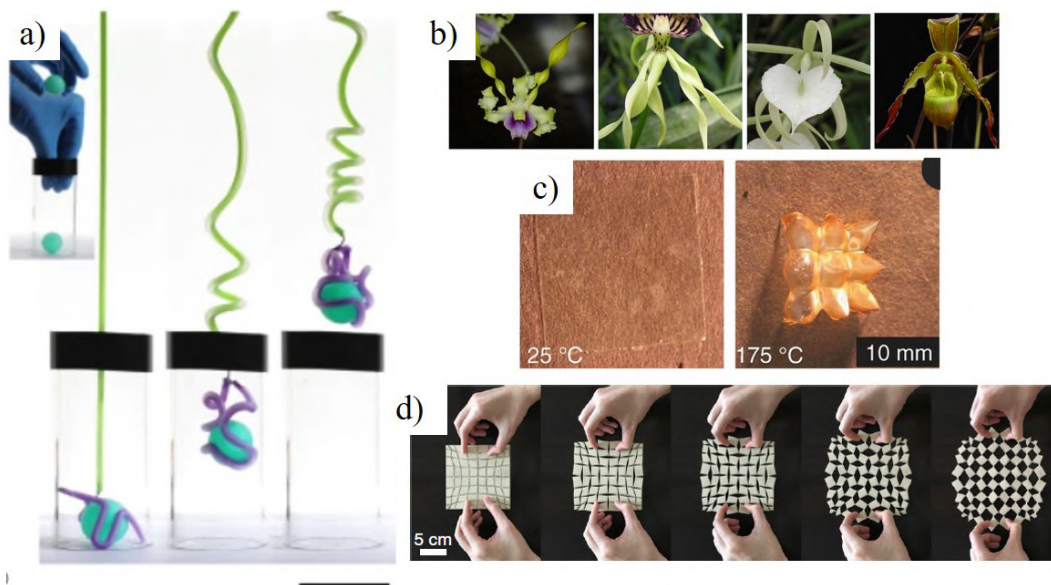


Figure 1 Examples of shape morphing materials. a) A soft robot grabbing a ball [1]. b) Different morphologies of long orchids due to differential growth [2]. c) Shape changing of a thin layer of liquid crystal elastomer [3]. d) Deployment of a kirigami tessellation [4]

For example, the emergence of *soft robotics* [5] in the last decade opens a new paradigm. In contrast with standard robotics, where stiff members (the supports) are articulated and actuated by separate active devices (motors), in soft robotics, the material is both the motor and the support, so that “the material is the machine” [6]. By relying on continuously changing shapes, soft robots can be designed to crawl into narrow places [7] or gently grip fragile objects [1, 8], (figure 1a). Based on techniques and materials initially developed for micro-fluidics, soft robotics provides simple, resilient, lightweight and low-cost devices using fabrication techniques that become every year more accessible [1]. But it also leads to the question of the mechanics of continuous materials capable of distributed actuation.

General introduction

In a second stream of research, the study of instabilities in *non-linear physics*, which started in the 1980's, naturally lead to a fascination for morphogenesis in biology, and the mechanical instabilities resulting from differential growth [9]. Such phenomena lead to the self-shaping of slender biological organs [2, 10–12] (figure 1b). Instabilities were also recognized as a way to obtain fast change in shape (much faster than the actuation time-scale) with the beautiful example of the Venus Flytrap [13], a plant capable of capturing an insect without the fast activity of a muscle. It is also noted that sometimes very complex shapes may be obtained from rather simple growth law [14], emphasizing the crucial and subtle role of geometry in morphing processes.

An active area of *Material Science* is devoted to the development and study of “active” materials: materials that undergo deformation as a response to an external stimulus (which in fact is responsible for the energy input). For example, liquid crystal elastomers [15] and shape memory polymers [16] reorganize their molecular conformations when heated above a critical temperature, or dielectric elastomers [17, 18] expand when their surface is charged. There are many more examples of such material which can actively mechanically deform upon activation (light, temperature, solvent, electric or magnetic field...). Material scientists also investigated how to control spatially the deformation (its orientation and/or its magnitude), so they can produce complex 3D shapes. For example, in figure 1c, a specific pattern of orientation of the deformation in a sheet of liquid crystal elastomer takes a complex 3D shape when heated.

The last decade has also witnessed the development of *mechanical metamaterials*. These architected materials were first introduced to give them controllable (and often anomalous) wave propagation properties resulting from internal structure having similar scale as the wavelength. Soon, an interest arose for such “programmable” materials outside the domain of wave propagation, and several groups started investigating strategies to program a material’s mechanical response (the stress-strain law) [19]. An example of shape-changing metamaterial is presented in figure 1d, where a planar square is manually expanded into a disk. In this field, a fundamental question is therefore to “design” a material (using internal structures), an approach that we will follow in this PhD.

Several of these converging fields are making extensive use of *digital fabrication* techniques, such as 3D printers, laser cutters,... These devices become standard tools because they are fast and easy to use. They can be adapted to many materials, from traditional 3D printing filaments to elastomers, metals or other materials. They can also be used at different scales, from nano to macro and even to meter scale. Rapid prototyping opens the lead to new kinds of structures that were not accessible before and generates new scientific questions. In particular, the new trend of 4D printing emerges. It consists in 3D printing samples that are activable and that can evolve in time [20].

In term of applications, shape-changing materials open many possibilities. New prototypes could be used through tortuous paths, for example in mini-invasive surgery, as a shape-changing object can adapt to the body. Another advantage of such structures is that they can be easily manufactured in a simple geometry and deploy their shape later. By being designed in the first place as flat or undeployed, they could bring huge improvement for both storage and transport in the initial state. However there are not so many industrial applications of shape-changing materials (if we exclude the classical bimetallic

strip [21]). This might be due to the fact that material programming processes are often complex and not easily scalable to an industry. Another limitation for applications in most of the shape-changing concepts is that they lead to systems that are very soft and generally small (see for example the scale bar in figure 1c)

In this manuscript we question the possibility of designing relatively large (tens of cm) and stiff shape-changing systems using simple materials, simple actuation (thermal, pressure, direct force through wires, or surface tension) and standard rapid prototyping techniques (laser cutting and 3D-printing). The complexity of the design and the versatility of programming lies in the geometry of a structure, composed of a network of slender members arranged into cellular structures, that is designed to restrict or guide an otherwise featureless deformation. A recurring pattern of this work is the diamond-shaped unit structure (center in figure 2), but we will also consider other elementary cell geometries (chevrons and rectangles, in figure 2) as they lead to different elementary deformations.

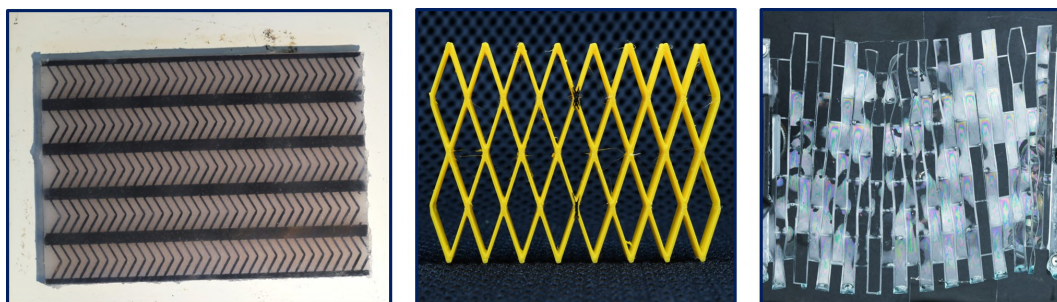


Figure 2 Main experimental systems used throughout this work. *Left*: a reinforcing mesh of chevrons embedded in a thermally activable elastomer matrix. *Center*: networks of diamonds, 3D printed out of thermoplastic polyurethane (TPU), can be externally activated. *Right*: a network of rectangles laser cut in a Mylar sheet is covered by soap films which deform it. All pictures are about 10 cm wide.

The manuscript is divided in four parts:

In a first part (chapter 1), we start with a brief introduction on the physics and geometry of shape changing process, and give examples from the literature. In a second part (chapter 2), we present a new method for shape morphing based on phase change and restrictive networks that include diamond networks. In (chapter 3), we study a second experimental system that uses thicker 3D printed networks as activable structures that are able to morph into 3D structures. Finally, in (chapter 4) we investigate the role of surface tension (soap films) in the design of ephemeral 3D shapes out of thin planar networks.

Résumé français

Les structures qui changent de forme trouvent des applications dans de nombreux domaines technologiques. Cependant, le passage d'une surface plane à une forme en trois dimensions est soumis à des conditions géométriques bien précises : il n'est pas possible de changer la courbure de Gauss d'une surface sans modifier les distances dans son plan. Cette propriété peut en revanche être exploitée pour changer de forme en variant localement la direction et/ou l'intensité de déformations spontanées. Dans ce but, nous utilisons des structures cellulaires à géométrie et motifs variables pour induire et guider des déformations dans le plan qui conduisent à des transformations tridimensionnelles de la structure. Ces structures cellulaires sont produites par prototypage rapide (impression 3D, découpeuse laser ...) et utilisent des systèmes d'activation simples (pression, chaleur, fils tendus ou tension de surface). Un motif élémentaire récurrent de cette thèse est le losange, mais d'autres motifs comme des chevrons, des rectangles ou des lignes sont utilisés et permettront d'obtenir différentes déformations élémentaires.

Au cours de cette thèse, nous avons utilisé trois systèmes qui mettent en œuvre des techniques d'activation différentes. Dans une première partie nous avons utilisé des structures cellulaires fines pour contraindre les déformations d'une matrice gonflant par changement de phase. Dans une deuxième partie, nous avons étudié un dispositif expérimental qui repose sur des structures plus épaisses, imprimées en 3D, qui sont activées des fils ou une mise sous vide dans une poche. Enfin, dans une troisième partie, nous avons cherché à utiliser la tension de surface à travers des films de savon pour créer des formes 3D éphémères.

Pour tous les systèmes, des formes simples comme des cônes et anti-cônes ont été programmées pour donner des exemples de formes élémentaires à courbure de Gauss positive ou négative. Une manière simple de programmer des cônes est de permettre une croissance radiale plus forte que la croissance azimutale. Au contraire en induisant une croissance radiale plus faible qu'une croissance azimutale, on produit un anti-cône. Le principe de cette méthode sera appliqué pour tester les différents systèmes.

0.1 Changement de forme par changement de phase

Dans cette première partie, nous avons utilisé une matrice qui subit de grandes déformations par changement de phase. Ce matériau, développé par Miriyev *et al.* [22], est composé d'élastomère et d'éthanol. L'éthanol est mélangé à l'élastomère avant la réticulation de celui-ci. Une fois réticulé, des gouttes d'éthanol se trouvent piégées dans la matrice. Lorsque la matrice est chauffée au delà de 80°C,

Résumé français

l'éthanol se met à bouillir et la pression à l'intérieur des cavités augmente amenant à un gonflement global de la matrice. Cette expansion est réversible et quand la température redescend, la matrice élastique revient à sa forme initiale.

Comme les gouttes sont globalement réparties de manière homogène dans la matrice, le gonflement est homogène sur tout l'échantillon. Ainsi, en chauffant le matériau, il subit seulement une homothétie et ne change pas de forme. Pour changer de forme, il faut rendre le gonflement de la matrice non homogène. Pour cela, nous avons choisi de contraindre son gonflement en incluant de minces réseaux inextensibles dans la matrice. Ces réseaux sont obtenus par découpe laser des feuilles de Mylar de 30 μ m. Il sont ensuite insérés de part et d'autre de la matrice pour que la déformation soit symétrique (figure 1).

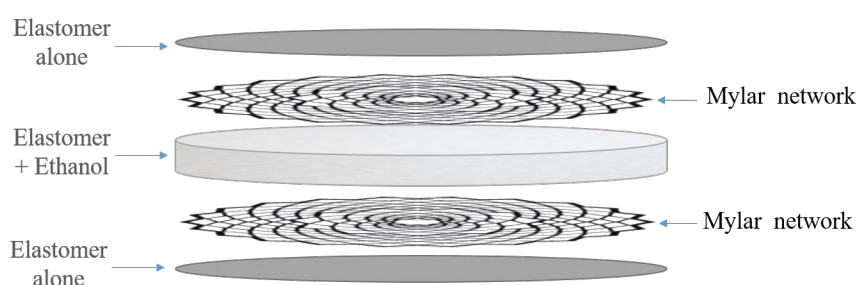


Figure 1 Confection des échantillons. Au centre se trouve la matrice active élastomère/éthanol qui gonfle quand le matériau est chauffé. Des réseaux inextensibles identiques sont déposés de part et d'autre de la matrice pour contraindre sa déformation. Enfin, à l'extérieur de l'échantillon, des couches d'élastomère pur sont coulées pour limiter les fuites d'éthanol.

En changeant les motifs des réseaux, il est ainsi possible de programmer différentes formes. Dans un premier temps, des réseaux sont composés de larges lignes parallèles également espacées reliées par des chevrons. Quand la matrice est activée, la déformation le long des lignes est bloquée, la matrice ne peut donc gonfler que dans la direction perpendiculaire aux lignes. Différents échantillons tests ont été utilisés pour mesurer l'influence des chevrons sur la déformation des échantillons. Il en ressort que l'angle et la densité des chevrons reliant les lignes n'agit qu'au second ordre, la déformation étant majoritairement guidée par le motif des lignes.

Au lieu d'utiliser des lignes parallèles entre elles qui n'autorisent qu'une simple déformation dans le plan, les lignes peuvent être agencées différemment. Pour obtenir un cône, le réseau est composé de cercles concentriques reliés par des chevrons. Le gonflement n'ayant lieu que perpendiculairement aux lignes, les rayons de l'échantillon tendent à augmenter alors que les périmètres restent constants (figure 2). À l'inverse, si les lignes sont disposées en étoiles et reliées par des chevrons, un anti-cône est obtenu.

Un autre type de motif élémentaire est utilisé : le losange. Quand le losange est activé, il se déforme de manière couplée selon ses deux diagonales : si l'une rétrécit, l'autre grandit. Dans le cas de l'activation par une matrice qui gonfle, les losanges tendent à devenir des carrés, ce qui maximise leur aire. Ainsi, la déformation est négative le long des grandes diagonales et positive le long des petites

0.2 Changement de forme par fermeture de structures cellulaires

diagonales. La déformation dépend de la géométrie des losanges et plus particulièrement de leur angle initial. Plus ils sont éloignés du losange, plus ils se déforment. Expérimentalement, les losanges tendent vers le carré mais ne l'atteignent pas.

Si ces losanges sont alignés, le système reste dans le plan. Mais si leur orientation dans l'espace est choisie avec soin il est possible de programmer des formes en 3 dimensions. Pour obtenir des cônes et des anti-cônes, le réseau de losange est formé par l'intersection de spirales logarithmiques orientées dans des directions opposées. Grâce aux propriétés de ces spirales, les losanges ainsi dessinés ont tous le même angle même si leur taille change. Si la grande diagonale des losanges est orientée dans la direction azimutale, une fois l'échantillon activé, il y aura une déformation négative dans la direction azimutale et une déformation positive dans la direction radiale, menant à l'apparition d'un cône (figure 2). Au contraire si la grande diagonale est orientée suivant les rayons, un anti-cône apparaît.

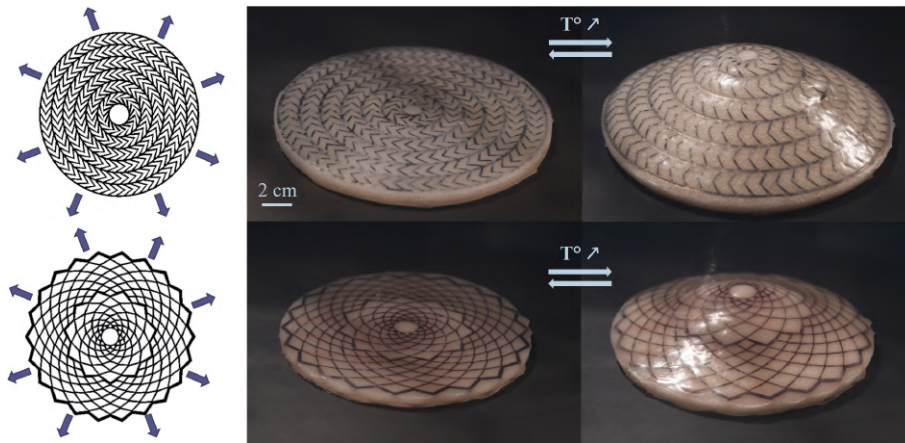


Figure 2 Exemples de formes 3D obtenues avec des lignes et chevrons (haut) et des losanges (bas).

Ainsi en utilisant une matrice actionnée par changement de phase, il est possible d'obtenir des formes 3D de manière réversible. Une des limites de cette méthode est la matrice en elle-même. D'un échantillon à un autre, les déformations sont différentes. Il est donc difficile de quantifier précisément la déformation des échantillons et de s'en servir pour programmer une forme précise.

0.2 Changement de forme par fermeture de structures cellulaires

Si dans la partie précédente, les réseaux cellulaires agissaient de manière restrictive en contraignant le gonflement d'une matrice, dans cette partie, les cellules des structures sont utilisées en compression. Au lieu de changer de forme par gonflement d'une matrice, les réseaux sont ici activés directement. Ces réseaux sont plus épais (~ 1 cm) et imprimés en TPU (thermoplastique polyuréthane) par impression 3D. Ils sont composés de losanges qui se ferment quand ils sont activés, menant à une déformation négative dans la direction de fermeture et positive dans la direction perpendiculaire. L'activation se fait soit par la pression, soit par la tension mécanique de fils parcourant la structure.

Résumé français

Dans un premier temps, nous avons choisi d'utiliser les fils comme moyen d'activation des cellules. Les fils passent à travers les cellules de la structure le long de la diagonale qui doit être fermée. Comme dans le système précédent, si les losanges sont alignés, la déformation reste dans le plan. Pour obtenir des formes en 3 dimensions, les losanges sont aussi construits par l'intersection de spirales logarithmiques. Toutefois, les formes obtenues sont inversées : si la grande diagonale des losanges est alignée selon les périmètres, un anti-cône apparaît lors de la fermeture des cellules, inversement si les losanges sont alignés avec les rayons, un cône apparaît.

Pour programmer des formes plus complexes, il faut varier localement la déformation de chaque cellule. Si on veut utiliser des losanges simples, il faut changer les paramètres géométriques de chaque losange (taille, angle, ...). Cependant l'utilisation de losanges de différentes formes et tailles rend le pavage de l'espace beaucoup plus compliqué et limite les possibilités. Une alternative à cela est d'insérer des cales à l'intérieur des losanges pour bloquer leur forme finale. Dans chaque demi-losange, trois triangles sont dessinés et se bloquent une fois au contact. En choisissant la taille de ces triangles il est possible de programmer la forme finale des losanges et donc la déformation à l'échelle de la cellule. Plus les cales sont grosses, plus la déformation est limitée.

Cette technique est utilisée pour programmer des formes plus complexes que des cônes et anti-cônes. Une des solutions pour créer des structures axisymétriques est d'utiliser comme base un réseau de losanges déterminé par des spirales logarithmiques pour avoir des cellules qui ont toutes le même angle initial. Un algorithme prend un profil en entrée, et calcule la déformation nécessaire pour chaque couronne de losanges et en déduit la taille des blocs. Avec cette méthode des objets, comme des sphères ou des ellipsoïdes peuvent être obtenus à partir d'une structure plane.

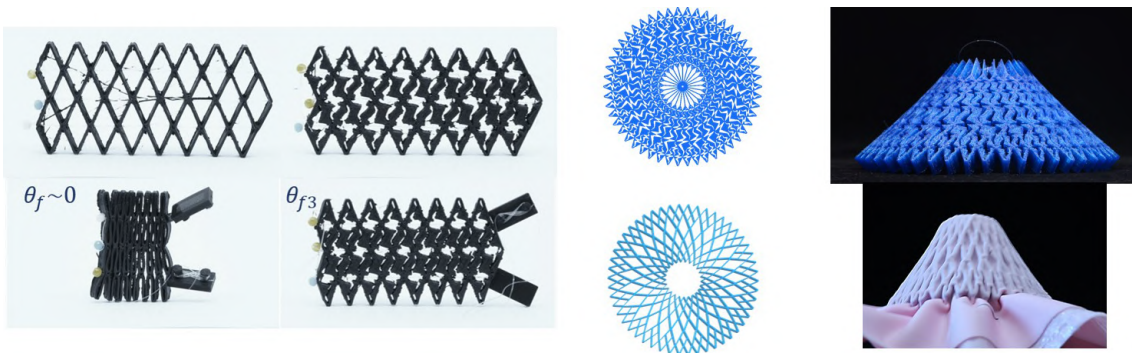


Figure 3 À gauche, des exemples de losanges alignés avec et sans cales dans leur état initial et après activation. À droite en haut, l'activation d'une structure par des fils pour obtenir un cône, en bas une structure activée par le vide pour donner un cône.

Une méthode plus générale peut être utilisée pour programmer des structures qui ne sont pas axisymétriques en utilisant un réseau de Tchebyshev. Ce travail a été réalisé en collaboration avec Hillel Aharoni du Weizmann Institute. Un maillage de losanges avec une longueur des côtés constante est dessiné sur une surface 3D et l'angle de chaque losange est mesuré sur cette forme 3D. L'angle final mesuré des losanges est ensuite encodé dans la taille des cales des losanges d'une grille de losanges

identiques et alignés. Une fois que les fils passés à travers toutes les cellules sont tendus, la forme 3D programmée apparaît.

Pour mieux comprendre le comportement de ces structures, une étude mécanique a été réalisée. Il en ressort que la mécanique de tels objets est gouvernée par la mécanique des petites poutres qui composent chaque losange.

Dans un second temps, ces structures imprimées en TPU sont placées dans des sacs en tissu étanches dans lequel le vide est fait. En mettant ces objets sous dépression, chaque cellule se ferme le long de sa petite diagonale. Quand le vide se fait, les losanges ne se ferment pas totalement car le tissu a tendance à s'engouffrer dans les cavités. La hauteur des échantillons doit être choisie de manière à ce que le tissu des deux côtés de l'échantillon ne rentre pas en contact mais que la structure soit suffisamment fine pour se courber dans la forme désirée. Cette technique d'activation ne permet cependant pas une mesure quantitative des déformations et ne permet donc pas de programmer de formes complexes.

0.3 Sculpter des films de savons

Dans ce dernier système, le moteur de la déformation est la tension de surface. Ce travail a été réalisé en collaboration avec Pierre-Brice Bintein et Rémi Abdallah. De minces réseaux de Mylar sont placés dans un bain d'eau savonneuse pour créer des films de savon dans les différentes cellules. Les réseaux utilisés sont composés de rectangles disposés en quinconce (figure 4 gauche). Quand un film de savon est tendu à l'intérieur des cellules, celles-ci se referment dans leur largeur alors que presque aucune déformation n'est observée dans la longueur. La déformation maximale qui peut être obtenue quand toutes les cellules sont fermées est de 50%, car seulement la moitié des cellules se referment sur chaque ligne. Les deux énergies en compétition sont l'énergie de la tension de surface et l'énergie élastique des cellules. Il existe deux modes de fermeture : une fermeture dans le plan (2D) et une fermeture hors-plan (3D) (figure 4 droite). Le passage de l'une à l'autre se fait en changeant les paramètres géométriques des cellules.

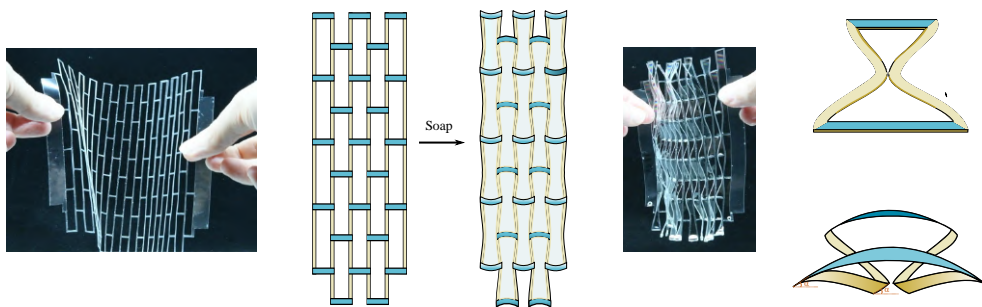


Figure 4 À gauche un réseau de cellules rectangulaires plongé dans de l'eau savonneuse. À droite, en haut, une cellule unité qui se déforme dans le plan, en bas, une cellule unité qui se déforme hors du plan.

Résumé français

Un diagramme de phase peut être tracé pour déterminer le comportement de chaque cellule quand elle est plongée dans l'eau savonneuse. L'étude fait apparaître deux nombres élasto-capillaires sans dimension qui expriment l'équilibre entre l'énergie de la tension de surface et l'énergie élastique de déformation de la cellule dans le plan :

$$A_{2D} = \frac{\mathcal{E}_{elast2D}}{\mathcal{E}_{soap}} \Big|_{contact} = \frac{Ee^3td}{\gamma L^4} \quad (1)$$

ou hors du plan:

$$A_{3D} = \frac{\mathcal{E}_{elast3D}}{\mathcal{E}_{soap}} = \frac{Et^3}{\gamma} \sqrt{\frac{ew}{dL^5}} \quad (2)$$

La majorité des cellules se déforment dans le plan même si cette déformation peut être très petite et non observable à l'œil nu. Cependant pour $A_{3D} < A_{3Dc}$, où A_{3Dc} est un nombre élasto-capillaire critique, une instabilité apparaît et les cellules se ferment hors plan.

Pour programmer des formes, la taille des cellules est choisie de sorte que les cellules se ferment totalement ou partiellement hors plan (3D). Au lieu de les aligner, les rectangles sont utilisés pour paver un disque. Dans un premier temps, les rectangles sont alignés dans la direction radiale. Quand ils sont plongés dans l'eau savonneuse, ils se ferment selon leur largeur ce qui induit une déformation négative dans la direction azimutale, induisant la formation cône. Au contraire, si les rectangles sont alignés dans la direction azimutale, un anti-cône apparaît quand la structure est plongée dans de l'eau savonneuse. Dans ce deuxième cas, les rectangles sont courbés pour pouvoir paver l'espace il faut donc utiliser une correction pour prédire les paramètres qui permettent la fermeture totale des cellules.

Ainsi, en utilisant des films de savons qui ont une courbure de Gauss négative (comme toute surface minimale) il est possible d'obtenir à la fois des structures avec une courbure de Gauss négative ou positive. Le caractère éphémère des films de savon rend les manipulations des échantillons compliquée et ne permet pas la création de formes très complexes. Les mêmes motifs en rectangle peuvent être utilisés avec la méthode décrite dans la précédente section. S'ils sont imprimés en 3D et ont une épaisseur suffisante, ils peuvent être activés par le vide et donner les mêmes formes qu'avec la présence du savon.



Figure 5 De gauche à droite, le dessin du réseau de Mylar, le réseau à l'équilibre piégé dans un film de savon, le réseau activé par le savon présent dans toutes les cellules et enfin le réseau soumis à son propre poids quand tous les films de savon ont éclaté. Les rectangles sont alignés radialement, ainsi un cône apparaît quand la structure est activée par les films de savon.

Chapter 1

Introduction to shape morphing

Cellular structures for shape morphing, what does it mean ?

Morphing comes from the ancient Greek *morphé* that means shape. The term morphing often refers to special effect in image animation whereas the term of shape morphing is more used in the soft robotic field. In this first chapter, we will first explain what mechanisms can be involved in a shape change and how to trigger them. We will then give examples of morphing object and their possible applications.

Contents

1.1	Geometry and morphing	11
1.1.1	Bi-layer effect	12
1.1.2	Geometry of surface shaping	15
1.2	Active shape changing due to internal mechanisms	19
1.3	Cellular structures for shape morphing	21

1.1 Geometry and morphing

Changing the shape of an object can be done following three elementary paths: subtractive, additive or deformation. In the subtractive way, the object is broken, or some material can be removed to obtain a new shape: this is the case of sculpture in stone. Another way of modifying the shape of an object is by assembling the new object with existing parts of another one, like a furniture (additive way). With these methods, the objects loose their integrity: new boundaries are created or suppressed.

In the following we focus on an alternative way: shaping that consists in a continuous non-destructive shape change. In order for objects to deform without breaking, they must be soft enough. Modifying the shape of bulk material requires large strains. Materials such as sand or modeling clay can withstand it, as they are plastic enough. However, modifying the shape of bulk material with high Young modulus like stone or wood leads to its failure, but such materials can be shaped if they are thin enough, or heated to become more ductile, such as iron that can be heated to be bent for sculptures (Figure 1.1).



Figure 1.1 Forged iron sculpture “The Comb of the wind” by Chillida (San Sebastian, Spain).

Thus, to design shape-changing objects, the constitutive material and the object scale are important. Objects must be stiff enough to maintain their shape, but soft enough to undergo a shape change. We will detail what “soft enough” means in the following section.

Until now, we have mentioned objects that change shape due to external forces, so that materials can adopt many shapes depending on the will and action of the operator. But shape change can be internally programmed, and then triggered. Doing so the final shape is always known and is not directly dependent on the will of the actor. Shape-change can be beautiful in itself and is very present in art (figure 1.2), but it can also be useful, for example in soft robotics where a continuous programmed deformation is very important. As mentioned, deforming a bulk is not easy whereas deforming a slender object is much easier, that is why there is a larger focus on the morphing of slender objects in the literature. Most of the shape change occur in 2 dimensions, and the objects are most of the time rods, or elongated beams. They rely on a "bi-layer" effect that we explain now.



Figure 1.2 Solstice, a kinetic clock that open and close with the hour from Animaro. The shape evolves in time.

1.1.1 Bi-layer effect

This very simple phenomenon is present in nature on many forms. For example, a pine cone can be opened or closed depending on the humidity rate [23]. When the pine cone are on the tree, they remain

closed and only open once they fall and dry, liberating the seeds to the ground. Every scale is composed of two parallel layers on top of each other that do not shrink by the same amount when the pine cone dries: one layer becomes shorter than the other one, and this mismatch in length causes a bending of the structure, opening the pine cone. The same strategy is used in art and design to create samples that are sensitive to humidity rate [24–26] (figure 1.3).

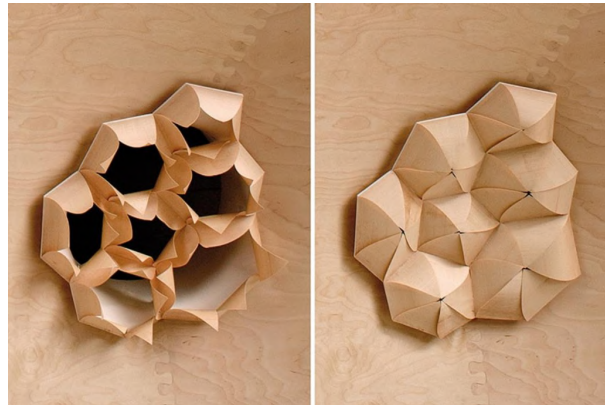


Figure 1.3 Photo of a HygroSkin aperture adapting to weather changes: open at low relative humidity rate (left) and closed at high relative humidity rate (right). Image by Achim Menges' group (2013).

This bi-layer effect first mechanically introduced by Timoshenko [21] described the bending of a beam composed of two layers of metal that do not have the same heat expansion rate. When the beam is heated, one layer gets longer than the other and again the material bend to satisfy the mismatch. In a bent sample, the outer layer is longer than the inner one and thus fits the mismatch (see figure 1.4).

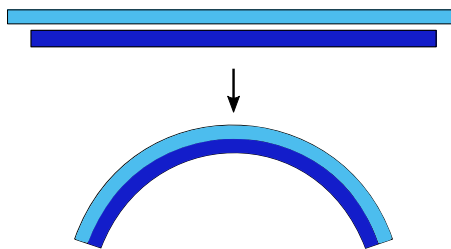


Figure 1.4 Bi-layer effect: two joint layers of materials with a dimensional mismatch tend to bend, placing the longer layer on the external part.

This effect is very powerful to bend slender structures and can be used to actuate. The activation can be done in many ways: temperature, humidity rate, pressure, light [27]. Being able to activate the samples provides a response in time that is often reversible. The bending actuation can be done with rods[28] or mesh of rods [29] that bend in order to create new structures by changing shape with temperature, or with pressure [1] for example. Strips can also be used and can be activated by humidity rate [30] or pressure [7].

Introduction to shape morphing

The size of the samples and their thickness are important in order for the effect to appear but another dimension can be added: the choice of the material. It can be stiff like wood or metal, or much softer. The last cited example used elastomer and internal pressure to create one of the first soft robots [7], opening the way to a large variety of actuators. Like an octopus, in soft robots, the change in shape occurs because of a distributed strain. Depending on the geometry, soft robots can move in complex, tortuous and narrow environment [7], or help grabbing delicate objects [8].

Such soft robots are bending because they are composed of two different layers that do not behave the same when the sample is activated. One layer, the restrictive one, does not change in length when the sample is activated. It can be composed of the stiffer or thicker material. The other part is meant to expand with the pressure and is often composed of cavities that expand like a balloon.

All these transformations occur because bending is strongly favored over stretching. Slender objects easily deform in bending rather than in stretching (elastic response). Considering a sample of length L , width d and thickness t , and assuming that its end is displaced by distance δ leading to a pure compression. The associated elastic energy scales as :

$$\mathcal{E}_{elastic} = EtdL \left(\frac{\delta}{L} \right)^2 = EtdL\epsilon^2 \quad (1.1)$$

If instead of compression, the sample keeps its length, it must bend with a deflection $\delta' \sim \sqrt{L^2 - (L - \delta)^2} \sim \sqrt{L\delta}$ when δ is small (figure 1.5), and the scaling of the associated bending energy is:

$$\mathcal{E}_{bending} = Et^3 dL \left(\frac{\delta'}{L^2} \right)^2 = Et^3 dL \frac{\delta L}{L^4} = E \frac{t^3 d}{L} \epsilon \quad (1.2)$$

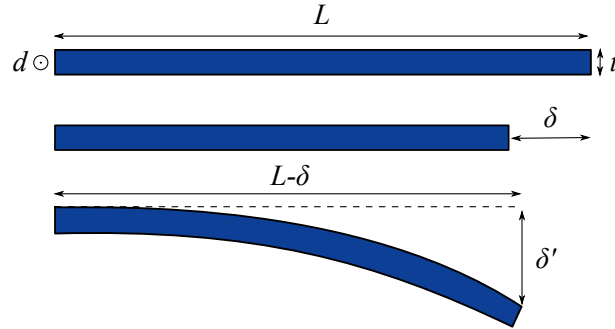


Figure 1.5 Scheme of a beam before and after bending instability.

For very small δ , the stretching energy (quadratic in δ) is lower than bending energy (linear in δ), and the beam remains straight and compressed. This is true until $\mathcal{E}_{elastic} \sim \mathcal{E}_{bending}$, which corresponds to a critical buckling strain on the order of $\epsilon_b = \left(\frac{t}{L} \right)^2$. Above this strain the beam prefers to bend than being compressed. In slender structures, the ratio $\frac{t}{L}$ is quite small that explains why most of the structures bend in the previous examples.

Up to now, we have described samples that bend in one direction, the shape changing is thus limited. To obtain 3D object, many bending beams have to be arranged together because, in order to get complex 3D shapes, samples have to be bent in more than one direction. Thus instead of using rods or beams, plate can be used. But if a simple bi-layer effect is used for a thin plate (with isotropic expansion of one layer), the bending will still occur in one direction [31]. In order to have bending in two directions of space, the deformation on the plate has to be more complex because of an important geometrical limitation that we review next.

1.1.2 Geometry of surface shaping

1.1.2.a Gauss' *theorema egregium*

Changing the shape of a plate has strong geometrical implications. A well-known example is the cartographer's problem: it is not possible to draw an accurate 2-dimensional map of the Earth. Projecting the spherical map onto a plane can only be done at the expense of deforming the continents or oceans. This fact was first explained by Gauss in a theorem that he considered as remarkable: the *theorema egregium*. This theorem states that it is not possible to change the Gaussian curvature of a surface without changing its metric, *i.e.* the distances between the points along the surface.

The Gaussian curvature K , is defined locally as the product of both principal curvatures K_1 and K_2 of a surface. If both curvatures have the same sign, the Gaussian curvature is positive: the archetypal example is the sphere (figure 1.6 left). If K_1 and K_2 have opposite signs, the Gaussian curvature is negative, which represents saddle shapes (figure 1.6 right). If at least one of the two principal curvatures is zero the Gaussian curvature is zero. The particular group of shapes that have zero Gaussian curvature everywhere is called developable surfaces, and includes all the shapes that can be obtained from a planar sheet without stretching or compressing it (planes, cylinders, cones...).

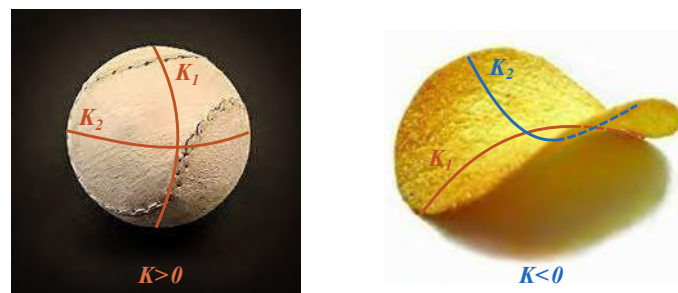


Figure 1.6 Example of positive (left) and negative (right) Gaussian curvature surface with respectively a pelota ball and a potato chip.

A simple manifestation of Gauss's theorem is that when a circle with radius r is drawn on surfaces with positive or negative Gaussian curvature, the perimeter is larger or smaller than $2\pi r$. The radius is measured along the surface as if the circle was drawn with a pen attached to the center with a flexible

Introduction to shape morphing

rope. Let us take the example of a sphere of radius R on which we draw a circle of radius $r = \phi R$ (see figure 1.7 left).



Figure 1.7 Circles on non-developable surfaces. On positive Gaussian curvature surfaces (left), circles with radius r have a perimeter shorter than $2\pi r$. Conversely, on negative Gaussian curvature surfaces (right) the perimeter is longer than $2\pi r$.

The actual perimeter of the circle is $2\pi r' = 2\pi R \sin \phi$ with R the radius of the sphere and ϕ the angle from the vertical. Writing the expansion for circles of radius much smaller than the sphere radius ($r \ll R$), the actual perimeter can be written:

$$P = 2\pi r' = 2\pi r \left(1 - \frac{1}{6} \frac{r^2}{R^2} + \mathcal{O} \left(\frac{r^4}{R^4} \right) \right) \quad (1.3)$$

or

$$P = 2\pi r \left(1 - \frac{1}{6} K r^2 + \mathcal{O} (K^2 r^4) \right) \quad (1.4)$$

This equation can be generalized to any shape [32] and reads:

$$P = 2\pi r \left(1 - \frac{K(P_i)}{6} r^2 + \mathcal{O} (r^4) \right) \quad (1.5)$$

where $K(P_i)$ is the Gaussian curvature measured at point P_i in the center of the circle.

With this equation, it can be seen that for positive Gaussian curvatures ($K > 0$), the perimeter is smaller than $2\pi r$. For the negative Gaussian curvatures ($K < 0$), the perimeter is larger than $2\pi r$. Finally, when the Gaussian curvature is zero, the perimeter is exactly $2\pi r$. We will repeatedly use this simple argument with radius and perimeter when analyzing and programming shape morphing in this manuscript.

Two particular shapes are present throughout this manuscript : cones and e-cones (where e stand for "excess"). These shapes are particular because at first glance it seems that they have zero Gaussian curvature, but it is not exactly the case. The two shapes seems to be ruled surfaces, i.e surfaces that can be described as a set of points swept by a moving straight line (figure 1.8, bottom) and in addition, they do have a zero Gaussian curvature. However that does not describe what is happening at the center of

both shapes. These singular regions bear concentrated Gauss curvature. The integral of the Gaussian curvature of these shape around any surface that contains the singular tip is constant and not zero.

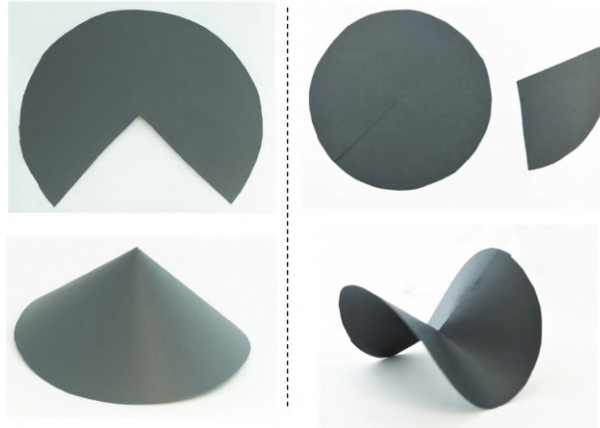


Figure 1.8 Example of a cone (left) and a e-cone (right).

For example, these surfaces can be obtained experimentally by adding or removing a section of a disk. By removing a section from a disk (figure 1.8, left), a cone is obtained, and we see that the perimeters indeed are smaller than they should be considering their distance to the center. Moreover, when a point runs along a closed curve containing the tip, it turns by an amount that less than 2π when returning to its initial position: there is a deficit angle. The Gaussian curvature of the sample is indeed positive.

If instead of removing it, an additional sector is added to a disk, an e-cone (excess cone) emerges [9], due to an excess of length for the perimeter and thus an excess of turning angle along a closed path. The Gaussian curvature of the sample is thus negative.

1.1.2.b Metrics changing strategies

Following Gauss theorem, in order to change shape, the metrics of the surfaces must evolve. This can be done in three different ways : making folds, or cuts, or using internal mechanisms.

Folding:

The most famous example of shape-changing with folds is origami: the Japanese art of paper folding. By choosing carefully the folding pattern of a sheet of paper, a wide variety of shapes can be obtained from very simple to very complex. Depending on the number of folds and their complexity, the final shape can go from the paper fortune teller to a bunny or a dome [33] (figure 1.9). These shapes are clearly non-developable (because they include non-zero Gaussian curvature) even though the paper sheet itself is very slender and therefore very close to be inextensible. This is because between each facet, material has been "tucked" inside, therefore modifying the apparent metric.

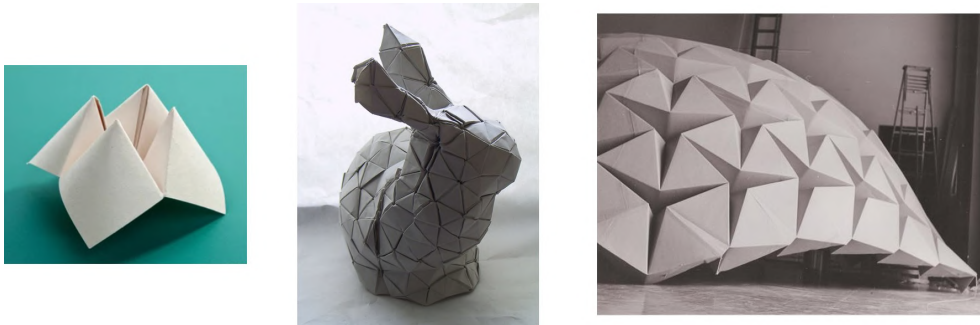


Figure 1.9 Regular paper fortune teller (left), bunny from Tomohiro Tachi[33] (center) and a dome by Ron Resch.

In addition to shape changing, origami can also help to design structures that are deployable [34]. An example of pattern that allow to create deployable structure is the Miura ori pattern [35]. Deployable pattern can be used for example in space [36] but can also be used to create motion in robots [37–39].

Another way of using fold is by using wrinkles. By wrinkling, a sheet can adapt and change its global Gaussian curvature. A spherical cap can adapt to a flat interface by making some wrinkles [40, 41] or in the other way, a planar sheet can take a spherical shape by wrinkling [42].

Cutting:

A famous art, also coming from Japan is using cuts to change the shape of a paper sheet: the kirigami art. Cuts are made on planar sheets, and by stretching these sheets, the cuts open, and a 3D shape may emerge. Depending on the local geometry of the cuts, the final shapes are totally different. For example, using a kind of cross patterns, a sphere can be mapped [43] (figure 1.10). By locally changing the cut pattern, complex shapes can be obtained [4, 44] when the structures are activated. The deformation of kirigami can also be used in soft robots, for example to make a soft robot crawl [45] or to grab fragile objects [46].

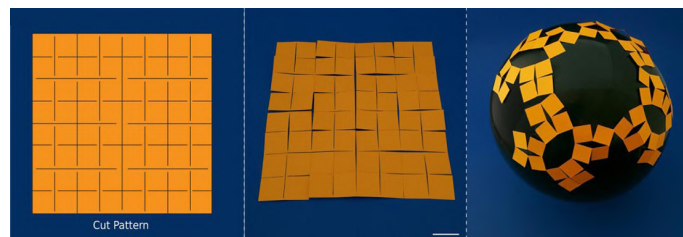


Figure 1.10 Shape obtained by cross cuts from [47] adapted from [43].

Contraction or extension along the surface

The change of metric that is necessary for morphing can occur with a differential expansion or shrinking of a material. By having a non-homogeneous shrinking or growth, the material undergoes a shape change.

1.2 Active shape changing due to internal mechanisms

Examples of such mechanism can be observed in nature, as for acetabularia, a small algae [48, 49] (figure 1.11). At the early stage of development of the plant, the radial growth is dominant, the algae adopts a conical shape. However at a later development stage, the dominant growth is circumferential, the algae thus go from conical to a flat state before becoming a saddle. By introducing a dominant radial growth, a conical shape appears whereas with a dominant circumferential growth, a saddle shape appears.

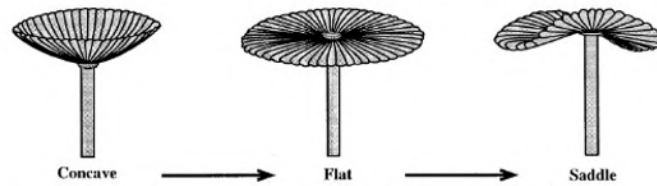


Figure 1.11 Evolution of the shape of the algae acetabularia (taken from [48]).

This type of shape morphing by differential growth can be obtained with different strategies and type of actuation that will be detailed in the following section.

1.2 Active shape changing due to internal mechanisms

Inspired by nature and the morphogenesis of plants, different strategies to mimic the differential growth have been developed:

Swelling hydrogels: Some hydrogels may swell when the physico-chemical conditions are varied. But shape change may only be obtained if the swelling is not homogeneous. Pioneering works used a spatial variation of the density of cross-links. A first method [50] proposed in 2007 by Klein *et al* uses different cross-link density in a NIPAM gels to create negative and positive Gaussian curvatures when the matrix is put in hot water. By locally tuning the swelling rate, the final shape can be designed. This first paper used material with different cross linking and was not precise enough to obtain precise shape. Using UV light to monitor the amount of reticulation helps design more complex shapes by being able to gradually change the density of cross-links [51, 52]. By using other types of polymers it is also possible to create hydrogels that evolve through time by modulating the cross linking ratio in time [53]. Using this method the path to the final shape can even be monitored [27].

Instead of a spatial distribution of swelling rate, some restrictive part (lines) can be used instead. These stiff line can be area with a large cross-link density [54] or a different stiffer material [55, 56]. Using 3D printing it is also possible to embed small fibers in the hydrogel that will constrain the expansion to their perpendicular direction [57]. By tuning the direction of these restrictive lines, the direction of swelling is defined and a 3D shape can emerge.

We see that it is possible to create Gaussian curvature with hydrogels using different techniques, however these techniques have some drawbacks : the structures are most of the time small and very soft,

and they need to be put in hot water to be activated with an actuation time limited by diffusion.

Liquid crystal elastomers: Liquid crystal elastomers (LCEs) are liquid crystalline polymer that are slightly cross-linked. They thus combine the elastic properties of a polymeric network and the organization of the liquid crystal phase [58]. They may exhibit a reversible shape change in response to heat, light or solvent. At room temperature, all the liquid crystals are aligned. When they are activated (heat, light or solvent), the polymer relaxes and an isotropic phase appears (there is no order anymore) so that the material undergoes a mechanical deformation. This strain may induce a global shape change as the metric is changed in an anisotropic way. By tuning the orientation of the liquid crystals at rest (along a director field), the local contraction and elongation are defined, and can be arranged to obtain 3D shapes. A shape change can be obtained using defects in the director field or continuous director fields [3, 59, 60] or by tuning locally the orientation of each liquid crystal, which gives access to a larger variety of shapes [15, 61]. Liquid crystal elastomers can also be printed, encoding the director field in the printing direction. By choosing carefully the printing path, 3D shapes can be obtained [62–64].

Dielectric elastomer: Dielectric elastomer are another way of activating expansion and thus a possible metric change. Dielectric elastomers are composed of a sheet of elastomer that is coated on both sides with soft electrodes (typically carbon powder). When a voltage is applied, electrostatic charges on both faces of the elastomer attract, and tend to reduce the membrane thickness, leading to a large in-plane expansion [65, 66] with strains up to 500% in some cases [67]. Applying a non-uniform voltage leads to out of plane deformation [18]. By spatially controlling the electric field, shapes such as cone or saddle can be obtained [68]. Inserting stiffer fiber also allow to obtain 3D shapes [17, 69, 70].

These different strategies to create Gauss curvature are used at small scale and remains relatively soft. It makes them not suitable for soft robots application at macro scale or even larger scales.

Inflatable structures: Another powerful actuation is pneumatic pressure. Pressure can be used to deploy large structures [71]. By inflating or deflecting objects, large expansion and shrinking can be observed. If the expansion is not uniform, the metric can be changed. As this type of actuation may develop large forces compared to the previous type of actuation, they are widely used in soft robotics to create crawlers or grippers by inflation [7, 8, 45, 72] or deflation [39, 73, 74].

But pneumatic actuation mostly rely on simple structure that only bend in one direction. Different strategies have been developed during the PhD of E. Siéfert [75] for inflatable structures which may bend in two directions. Two different systems were developed with extensible and inextensible material. In the first case, an elastomer matrix is cast with air channel inside: baromorphs. When these channels are inflated, they expand perpendicularly. By choosing the pattern of such channels, shapes with positive or negative Gaussian curvatures are obtained [76] (figure 1.12 top). In the second case, inextensible fabric are heat-sealed along path that delimits air channels. The sealing lines define the direction of shrinking,

as when the structure is inflated, the sealed lines get closer. It is possible to design the direction of these lines to obtain complex 3D shapes [77–80] (figure 1.12 bottom).

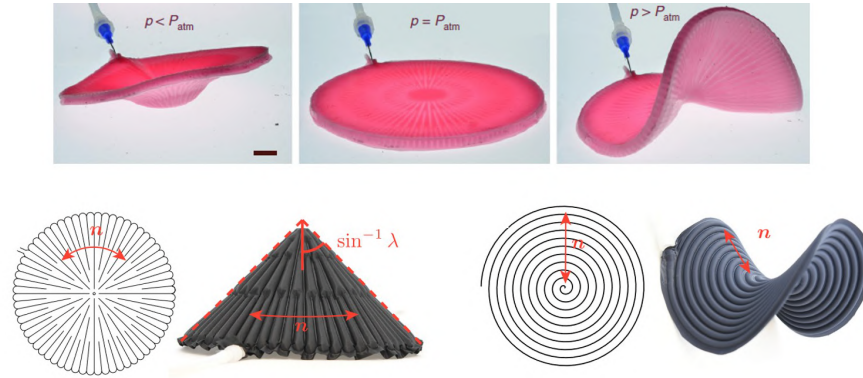


Figure 1.12 On top, baromorph upon deflation (right), at rest (center) and upon inflation (right). At the bottom, inflatable fabric structures with different sealing patterns [75].

We see that pressure can also be used to activate structures and made them deform. If constrained balloons are inflated they can adopt many different shapes [81].

Shape shift due to local unit cell morphing: An interesting strategy is to compose a sample out of a collection of small units that can be activated to create a 3D shape, instead of actuation of a continuous sample as a whole. Samples can be composed of active cells that deform with different speed, in order to create 3D shapes which deploy with a programmed deformation path [82]. By using the bistability of local unit cells of a network, complex shapes can be obtained and locked [83, 84]. Finally, using small cells with beams of different physical properties allows to create a bigger network that will deform. By using bilayer beams that respond to thermal expansion, the network can deploy in 2D [85] or in 3D [86] (figure 1.13). Deformation can also be due to the use of shape memory polymer in the cells [87].

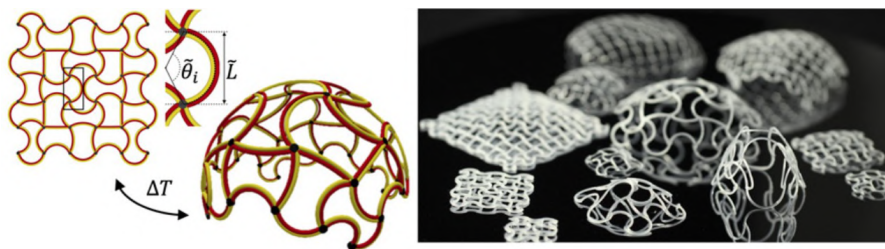


Figure 1.13 3D structures obtained from flat structure by increasing the temperature from [86].

1.3 Cellular structures for shape morphing

In this PhD work, we embrace the fact that to be able to transform into an interesting family of shapes, surfaces must undergo non-uniform (and possibly non-isotropic) expansion or shrinkage.

Introduction to shape morphing

We have reviewed above a variety of materials capable of undergoing such in-plane deformation in response to a stimulus. Many of them were difficult to manufacture and restricted to small scale.

We wish in this work to introduce new systems capable of shape-change, but we wish to restrict ourselves to systems that are easy to obtain through standard rapid prototyping techniques. Each of the three following chapter is devoted to a different system. The common feature is that the shape change will rely on the control of cellular networks which locally constrain the expansion or shrinkage of the structures, leading to 3D shapes.

Chapter 2

Untethered shape morphing by phase transition

Bread dough increases significantly its volume during baking as fermentation gases inflate into large bubbles. In a recent work from Miriyev *et al*, silicone elastomer materials containing micro droplets of volatile liquid have been found to expand in a similar way as the ambient temperature is raised above the boiling temperature of the liquid [22]. If the gas does not diffuse out of the material, the expansion process is reversible. When an internal structure limiting the deformation in certain direction is embedded in such expendable material, untethered shape changing objects can be obtained.

Contents

2.1	Change shape with expanding material	24
2.2	Experimental set up	27
2.2.1	Preparation of the material	27
2.2.2	Adjusting the fabrication procedure	29
2.2.3	From homogeneous expansion to shape-change: preparation of the samples	31
2.3	Lines and chevrons	32
2.3.1	From lines to chevrons	32
2.3.2	Mechanical properties of chevrons under traction	33
2.3.3	Parallel lines and aligned chevrons	38
2.3.4	Programming 3D-shapes	46
2.4	Diamonds network	50
2.4.1	Network of aligned diamonds	51
2.4.2	3D-shapes	58
2.5	Conclusion	64

2.1 Change shape with expanding material

If we look around us, we may realize that many materials undergo very large deformations upon activation in our daily life, especially in food. Various mechanisms are at play in the swelling of food materials under the influence of temperature or time. The use of baking soda or yeast is one of them. When we bake cakes, brioches or bread, the more the dough swells, the better. The mechanism involved to obtain large cellular structures in the dough is the same with yeast and baking soda: the release of carbon dioxide.

In the case of baking soda, the water present in the dough triggers an acid-base reaction which releases CO_2 . The heat of the oven shifts the chemical equilibrium toward the creation of more CO_2 . In the case of yeast, living organisms cause the fermentation of the sugar present inside the flour which generates alcohol and CO_2 . In both cases, as raw dough is easily deformable, the increase in gaseous CO_2 content creates cells that grow inside the dough which then solidifies at high temperature and remains inflated even after the CO_2 diffuses. Thus, thanks to an emission of gas, large expansions can be observed in the materials.



Figure 2.1 Leavened brioche after baking. The dough has expanded under the release of CO_2 during baking.

In other examples of food material, such as popcorn, the large expansion is due to water vapor pressure. Although dried, the grains of corn still contain a low level of moisture (10-15%). When the grains are heated (a temperature up to 180°C is needed), the water present inside the kernel boils and each small vapor bubble generates a high pressure vapor [88]. This increase in pressure makes the starch inside the kernel gelatinize and increase its volume. When the temperature is high enough, the pressure on the kernel makes it explode, the starch expands (just as the dough) and the familiar popcorn is obtained [89].

One last example of material expanding with gas/steam is the 'Keropok' or Krupuk cracker, a popular Asian crispy food and very common in Chinese restaurants in France. The dough is first prepared with

2.1 Change shape with expanding material

(tapioca) starch or flour, seasoning, flavor and water. This dough is rolled and cooked by boiling water, and as for popcorn, the starch gelifies and gets a new shape. This intermediate product is then cooled, sliced and dried in order to get small, round and stiff chips (figure 2.2 left). In a last step, this dried dough is fried in oil to obtain puffed crackers (figure 2.2 right). Even if the intermediate product is dried, a little amount of moisture remains. When it is fried, the residual water turns into vapor bubbles, and the increasing pressure leads to a very large plastic deformation of the sample [90] and the emergence of the puffed cracker (figure 2.2 right).



Figure 2.2 Crackers 'Keropok' in the intermediate state (left column) and after being fried (right column). When the crackers is fried, it expands by a very large factor and becomes puffed.

The process that we will use in this first chapter, developed by Miriyev *et al.* [22], bears strong similarities with the examples cited above: the material undergoes a very large expansion upon heating. It is composed of ethanol bubbles dispersed through an elastomeric matrix. When heated sufficiently, ethanol boils inside the cavities and forces the expansion of the elastomer matrix by a very large factor (figure 2.3).

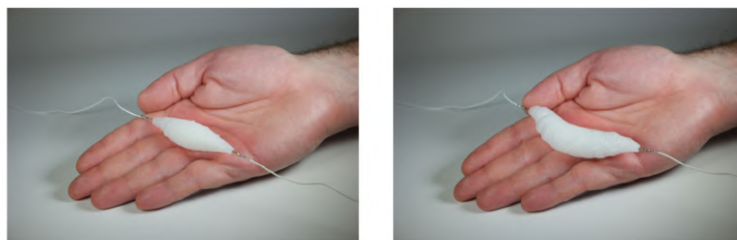


Figure 2.3 Material develop by Miriyev *et al.* [22] before and after heating by an internal resistive wire.

This material looks pretty similar to the 'Keropok'. In addition to the visual and physical aspect (whiter and puffed in the final state), the principle of actuation is identical. In both cases, the expansion of the raw material relies on the phase transition of a liquid trapped in the initial matrix. The main

Untethered shape morphing by phase transition

difference between the two products is that the expansion of the 'Keropok' is not reversible.

After having salivated over the starter, let us now focus on the main course: pasta. While uniform expansion of the material is interesting, it would lead to a homothetic transformation: the object grows but maintains its shape. It would be even more interesting if the final shape could be controlled. A team at MIT Media Lab developed pasta that can change shape upon heating [91]. Unlike the other systems cited above, when the pasta are cooked, they expand but also change shape. They do not only undergo a trivial homothety (figure 2.4).

During cooking, the pasta absorb water and thus expand (they also undergo a glassy to rubbery transition [92] due to the plasticizing effect of water). In [91], cellulose strips are deposited on top of the pasta, and these lines act as constraints reducing the water adsorption locally. Depending on the orientation of these cellulose fibers (black lines in fig 2.4) the cooked final shape is different.

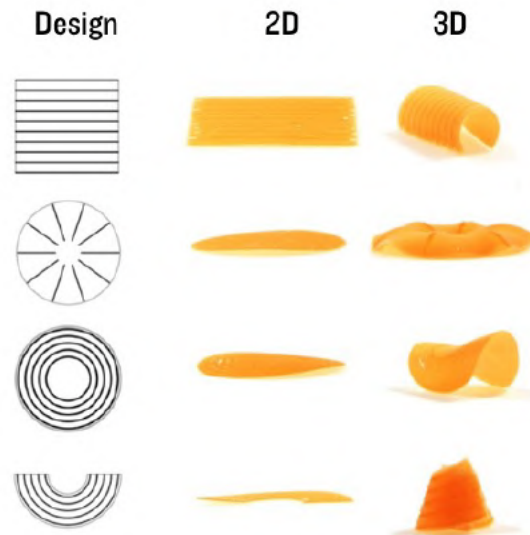


Figure 2.4 Composite pasta decorated with cellulose strips (black lines on the left panel) which locally reduce the water absorption during cooking. Flat before cooking (center) the pasta deploy into 3D shapes dictated by the geometry of the strips and the pattern of strips (right). Picture taken from [91].

Thus, in order to create 3D shapes with expanding material, the idea is to hinder expansion in a given direction of space through inclusions of non-active material (figure 2.5).

In the material developed by Miriyev *et al.*, some lines are left without alcohol to locally inhibit expansion. This idea appeared complex to implement experimentally, so that we decided to use stiffer material embedded in the matrix in order to block expansion in given directions of space. The samples then change shape due to anisotropic expansion imposed by the internal network (figure 2.5).

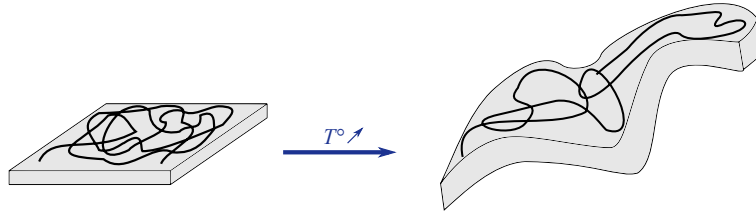


Figure 2.5 Principle of an expanding matrix with an embedded network in the initial and activated state.

The main challenge is then the choice and design of internal restrictive networks which force non-uniform expansion. We will explore two types of constraints to produce locally uniaxial or biaxial expansion. The first is achieved by internal networks consisting of series of parallel lines connected by chevrons. Conversely, biaxial strains are obtained by embedding arrays of diamond-shapes meshes (figure 2.6). A similar structure is for instance encountered in the well-known McKibben artificial muscle.

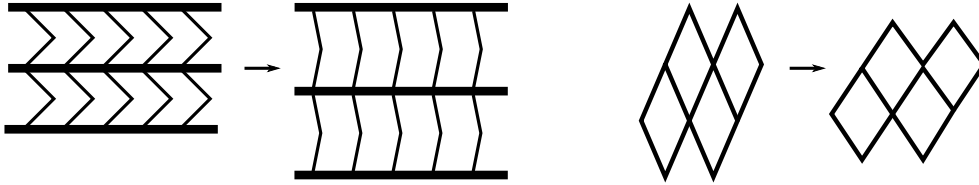


Figure 2.6 Unit pattern for chevrons networks (left) and diamonds network (right).

Thus in this chapter we will first explain how the samples are prepared and the different parameters that can be adjusted. Then we will detail the behavior of active matrices reinforced with two kinds of network: lines and diamonds (figure 2.6).

2.2 Experimental set up

2.2.1 Preparation of the material

The material provided to obtain large expansion is inspired by the work of Miriyev *et al.* [22]. It is experiencing a relatively reversible expansion by thermal actuation. It is composed of an elastomeric matrix in which small bubbles of a volatile liquid are dispersed. When the temperature of the sample is increased above the boiling point of the volatile liquid, the liquid trapped inside the cavities tends to boil, increasing the internal pressure. During a liquid-gas phase transition, the volume of the component increases dramatically. As the matrix is elastic, the increasing pressure in the small cavities inflates them until reaching a mechanical equilibrium. As a result, the cavities expand, deforming the elastic matrix and inducing an expansion of the overall material (figure 2.7). Thus thanks to the liquid-vapor phase transition of a volatile liquid, a large and homogeneous expansion is obtained. If the gas phase does not diffuse significantly in the inflated configuration, this actuation is reversible as the phase change is reversible and the matrix undergoes reversible elastic deformations (figure 2.8).

Untethered shape morphing by phase transition

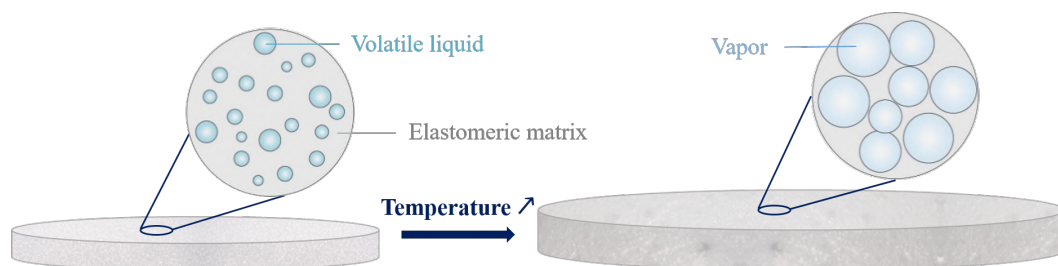


Figure 2.7 Material composed of an elastomeric matrix with trapped bubbles of a volatile liquid before and after heating. The increasing pressure inside the cavities leads to an overall expansion of the material.

The elastomer used for the matrix is a two-part platinum-catalyzed silicone elastomer: Ecoflex 00-35 fast and 00-50 from Smooth On®. These silicone elastomers are chosen for their high elasticity and because they are commercially available and easy to use. The standard procedure is to mix two parts (A and B) in equal amounts, cast and let it cure for a few hours at room temperature or in an oven at low temperature ($\sim 50^\circ\text{C}$). After curing, the material is removed from the mold and ready to use.

The volatile liquid in our case is ethanol, it is progressively added before curing to ensure a large expansion of the material. The ethanol is added to the part A of the silicone and then gently mixed. Mixing is a critical step because ethanol is not miscible with silicone. However, ethanol wets silicone which helps to create an emulsion. During the mixing air bubbles are trapped in the silicone. The part A with ethanol is then mixed with part B, cast and let to cure. Ecoflex 00-35 fast is mainly used for short curing time of typically 5 min. While short curing times limit the coalescence of alcohol droplets, they also hinder the gravity-driven rise of trapped air bubbles. The resulting elastomeric matrix containing air bubbles and ethanol is rather homogeneous upon heating (figure 2.8). The molds where the raw material is poured are closed from both sides to prevent the break of symmetry and to have two identical side surfaces.

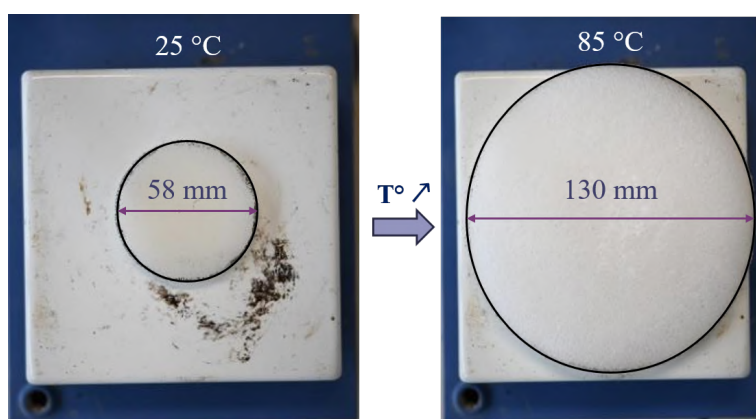


Figure 2.8 Sample of Ecoflex 00-35 fast with trapped ethanol bubbles inside before and after heating on a hot plate. The sample swell linearly by over 100 %.

2.2.2 Adjusting the fabrication procedure

2.2.2.a Selecting a volatile liquid

To be optimal, the volatile liquid has to meet some requirements. First it must be compatible with the silicone, in other words, the liquid has to wet both the cured and un-cured elastomer and not to be miscible. The ethanol has to wet the liquid silicone precursor to provide a nice emulsion. Secondly, its boiling point has to be low to be able to activate the sample at relatively low temperature (no more than 100°C) with non specific oven or heating process. Finally, it is better to find a non hazardous liquid that can be used without specific restrictions.

Ethanol is very convenient for its wettability and low boiling point. However as a very small molecule, it leaks easily from the sample. The matrix is not totally impermeable to liquid ethanol and even less to its vapor. Thus after each activation, a part of the ethanol trapped in the cavities vanishes and after few cycles the sample does not expand anymore upon activation. Among potential candidates as volatile liquids, water was disregarded due to its poor wettability and thus the impossibility to mix it correctly with part A.

We also tried 3MTMNovacTM7200, a hydrofluoroether. It seemed to meet all the criteria: high wettability and compatibility with the silicone and low boiling point (around 76°C). Experiments were conducted using the same protocol as ethanol. As the hydrofluoroether is denser than the silicone, it tends to sink at the bottom of the batch when mixed but seems to mix more easily. The mixture obtained with the hydrofluoroether and silicone is less turbid than the one with ethanol. Trapped bubbles seem also smaller. Once cured, specimens are nearly as clear as if nothing has been mixed to the Ecoflex matrix. Upon heating, a lot of very small bubbles appear in the material and cause small plastic deformations. Experiment showed that the deformation is smaller and requires higher temperatures and the process is less reversible than with ethanol. Thus we finally selected ethanol for our experiments.

Once the solvent is chosen, the proportion to be mixed to the silicone has to be determined. According to [22], the optimal percentage is 20% in weight (best expansion). In the lab, tests were done on small samples with various amounts of ethanol. Above 15% the expansion of all the samples are similar. Thus in the following experiments, a part 15% in weight is kept.

As ethanol tends to leak from the matrix, the samples are kept in sealed containers saturated with ethanol to limit the aging of the materials.

2.2.2.b Mixing techniques

As an emulsion has to be done with the part A and the ethanol, the technique of mixing is important. Ethanol is added 1g at a time and is then gently mixed with part A. As the ethanol is not miscible to part A, it takes time to incorporate it as small droplets. In all experiments, mixing is done by hand. A trial with a mortar and pestle was done in order to obtain smaller droplets in the emulsion. The expansion of the material was similar, but the temperature activation was higher and the process less reversible.

Untethered shape morphing by phase transition

Considering these results, and the one with the hydrofluoroether, it appears that having too small bubbles does not help. The pressure inside the bubble might be higher when the cavities are smaller, which could explain the higher temperature of activation, and the fact that the deformations seem more plastic.

As the mixing is done by hand, the expansion of the material is however not perfectly homogeneous. It is very hard to determine a global expansion with the temperature. One solution could be to mix with a stirring machine.

2.2.2.c Heating processes

In order to observe homogeneous and controlled heating over the sample, different ways of heating are tested but only one is kept to do the measurements.

In a first attempt to obtain uniform heating, the samples are immersed in boiling water. However, the samples are floating and water vapor prevents from taking pictures. Moreover with water the maximal temperature is fixed at 100°C and it is not easy to maintain a constant temperature that is not 100°C.

Another technique consists in putting the sample on a hot plate. In this configuration, pictures are easy to take but the heating is not homogeneous through the thickness (the sample had to be flipped frequently) and not easy to control. The positive point of this method was the actuation speed. The sample expands really quickly although the activation is less reversible as the ethanol diffuses more.

The last possibility we tested and selected is a homogeneous heating of the sample in an oven. We chose an oven with a large window in order to be able to take pictures: the environmental test chamber Weiss MKF115 (which offers possibility to monitor humidity, a feature we did not use during experiments). In this oven, the heating is relatively slow and the temperature rate cannot be tuned. However the measurements done are quite repeatable. In the experiments, a target temperature is set in the oven and the sample is put in it when the temperature of the oven is homogeneous.

We use several thermocouples to monitor temperature, a thermocouple is placed in the oven and three others are put inside the sample. Thus the temperature in the oven can be checked and the real temperature of the sample can be measured too. Two thermocouples are put inside the lateral edges of the samples and one inside the bottom edge (figure 2.9). The temperatures are recorded with an Arduino board connected to a computer in real time.

Not to be dependent on the potential impact of the temperature rate, the sample is put in an already hot oven at a given temperature. The inner temperature evolution of the samples is then recorded thanks to the three thermocouples, the temperature evolution is smooth and similar from one experiment to another. In a second part of the experiments, the heating is stopped and the door opened so that the sample cools down.

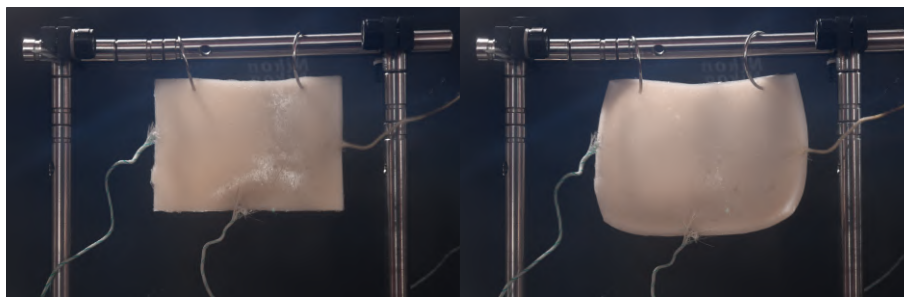


Figure 2.9 Expanding matrix in the oven at room temperature (left) and at 90°C (right).

If the sample is heated too much, we can observe that the experiment is not reversible. As ethanol is a very volatile liquid and a small molecule, it leaks through the sample and the experiment is not reversible anymore.

2.2.3 From homogeneous expansion to shape-change: preparation of the samples

In this chapter, we wish to use the liquid-gas phase transition for shape morphing. The expanding matrix naturally undergoes isotropic and homogeneous expansion because the bubbles are spherical and the distribution in the matrix is almost homogeneous, so that no shape change is observed. To trigger a 3D-shape from a flat object, we propose to constrain the expansion along chosen directions in space. To do so, stiffer fibers can be embedded in an expanding matrix to control the local deformation [93, 94]. In our case, to control the direction of dilatation, thin Mylar meshes are embedded inside the expanding material. They are embedded on top and bottom of the sample to keep symmetry in the system (figure 2.10). These networks are cut off a large 30 μ m thick sheet with a laser cutter and act as small links restricting the expansion of the matrix along their length. As the Young modulus of the Mylar is significantly higher than the elastomer, it is considered as inextensible. Imposing the local anisotropy of expansion, should allow one to modify the metric, and thus to produce 3D shapes.

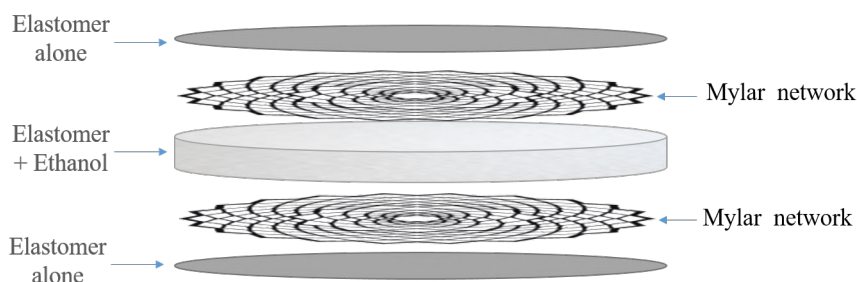


Figure 2.10 Expanding matrix with a Mylar network on top and on bottom.

In order to prepare the samples, two layers of pure elastomer (thickness: 0.6mm) are poured on two different plates. A network is then embedded in a second 0.6mm thick layer of pure elastomer on top of the previous ones for both sides. The excess elastomer around the mesh is then removed in order to have

Untethered shape morphing by phase transition

two faces of the size of the sample containing each one a network. They are then assembled in one mold where the expanding matrix is poured in between the two layers. The total height of the sample is 4mm.

We consider two different kinds of networks with different behaviors: “chevrons” and “diamonds”.

2.3 Lines and chevrons

The simplest pattern for restrictive networks is composed of straight inextensible lines. The swelling material should be restricted along the lines and can only expand along the direction perpendicular to these lines.

2.3.1 From lines to chevrons

Using solely lines is not convenient experimentally. As the networks have to be embedded in an elastomeric layer, it is difficult to handle lines without connections and to arrange them at the right place. Moreover bulging effects are observed and lines tend to slide inside the matrix. As a result, the final shape are out of plane and not reproducible (figure 2.12).



Figure 2.11 Sample with parallel lines at room temperature (left) and 90°C (center and right). The two samples (center and right) behave differently but do not remain in plane.

In order to solve the problem cited above, we decided to add chevrons to connect the thick lines between them. With these chevrons, the network can be manipulated as a whole piece and not as individual line. Moreover, they prevent the bulging deformation in the z-direction like a net and smoothen the deformation. The samples remain much more in-plane (figure 2.12). In the following experiments, only the lines are painted in black to ensure an easier detection.



Figure 2.12 Samples with parallel lines linked with chevrons at room temperature (left) and at 90°C (right).

Thus, chevrons improve significantly the experiments. They also have an influence on the mechanics of the sample as the samples do not expand the same way with or without chevrons. In addition, when the chevrons are in their open state (straight), they may block the expansion and stiffen the material. This hypothesis will be discussed in the following part 2.3.2.

2.3.2 Mechanical properties of chevrons under traction

Chevrons are added for experimental reasons. They could also impose a maximum deformation ϵ_{\perp} and could potentially help to stiffen the sample in the activated state. In a simple view, we would expect the material to be free to expand until the chevrons are stretched and block the deformation.

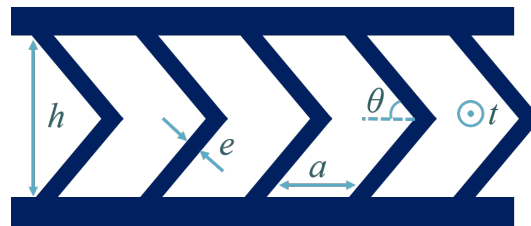


Figure 2.13 Sketch of chevrons in between two thick parallel lines.

In order to test this scenario, the mechanical responses of chevrons networks are measured alone without the expanding matrix. Test samples with a few chevrons are cut out of a Mylar sheets and then tested under traction with an Instron traction machine. The notations are the ones used in the figure 2.13. The distance h between the lines is kept at 15mm, the angle θ is varied from $\pi/3$ to $\pi/6$, the width e of the chevrons is set at 1.5mm or 2mm and the density d defined as $d = \frac{e}{e+a}$ changed from 0.3 to 0.6. The thickness t of the network is 30 μ m.

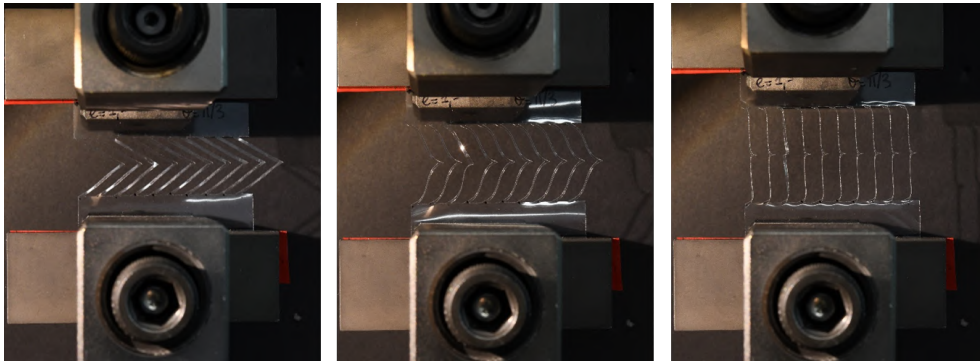


Figure 2.14 Chevrons under traction in an Instron test machine. Initial state (left), intermediary state during the opening of the chevrons (center) and final state when the blocking occurs (right).

When the chevrons are put under traction by the Instron machine, they first open very easily before blocking when in total extension (figure 2.14). This behavior can be observed on a force-strain curve figure 2.15 with $\epsilon = \frac{\delta l}{h}$. A small slope for small displacement is first observed before a steep change

Untethered shape morphing by phase transition

and a much larger slope (more than ten times higher). The chevrons are very weak when they open but become stiffer when fully deployed. With the plot in figure 2.15, the response of the reoriented chevrons is characterized by measuring the slope after the steep variation of slope. The response is considered linear when the chevrons start to be under tension. The linear approximation of the slope gives both the rigidity of the chevrons and the measure of ϵ_{open} , the final strain when the chevrons is open. It can be seen that when the angle θ increases, the chevrons are straighter and ϵ_{open} is smaller and the total extension of the chevrons occurs sooner.

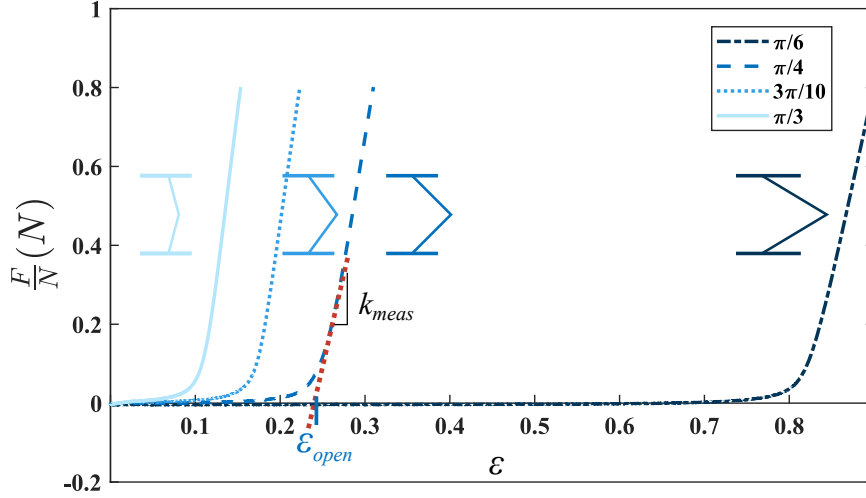


Figure 2.15 Experimentally measured force-strain curves of chevrons: $e = 1\text{mm}$, $h = 15\text{mm}$ and density $d = 0.3$ and $\theta = \frac{\pi}{6}$ to $\frac{\pi}{3}$.

The value ϵ_{open} of the final strain when the chevrons are open is calculated for all the samples. This value depends on the geometrical parameters of the chevrons. As a first approximation, the final length between the parallel lines can be defined as the total length of the chevrons (purple plain line figure 2.16) :

$$l_1 = \frac{h}{\sin \theta} \quad (2.1)$$

which gives a final strain ϵ_{op1} of:

$$\epsilon_{op1} = \frac{1}{\sin \theta} - 1 \quad (2.2)$$

This calculated strain appears slightly larger than the measured one (purple crosses on figure 2.17). We explain this fact by looking at the picture of the extended chevrons on figure 2.16: the chevrons are not thin wires, but are ribbons which twist, so that the final effective length is smaller than the total one.

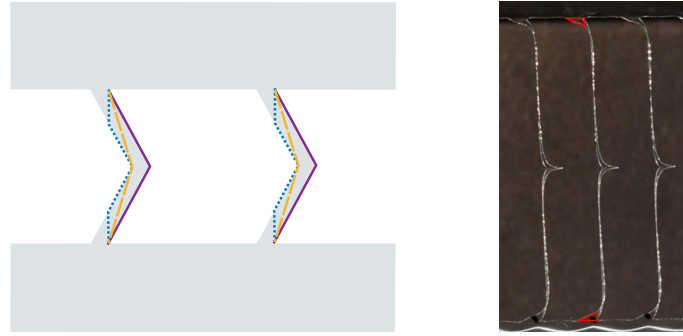


Figure 2.16 Sketch of the chevrons with the different final lengths considered. In purple and plain line, the total length, in yellow dashed line the smallest length between the two ends and in blue dotted line the measure inspired by the picture on the right.

As a second approximation, the final length is defined as the shortest straight line joining the plates through the chevrons (yellow dashed line in figure 2.16) and is equal to:

$$l_2 = 2\sqrt{\left(\frac{h}{2}\right)^2 + \left(\frac{h}{2\tan\theta} - \frac{e}{\sin\theta}\right)^2} \quad (2.3)$$

which gives a final strain ϵ_{op2} :

$$\epsilon_{op2} = 2\sqrt{\frac{1}{4} + \left(\frac{1}{2\tan\theta} - \frac{e}{h\sin\theta}\right)^2} - 1 \quad (2.4)$$

This theoretical strain is also overestimated as seen on the measures of figure 2.17. The real locking length is situated between l_1 and l_2 .

Looking at the picture more carefully in figure 2.16 right, it can be seen that a part of the inside length of the chevron is straight, and the rest (red triangle) is composed of one side of the triangles that appear on the edge. This third length l_3 inspired by the behavior during the experiment is represented with a blue dashed line on figure 2.16, with:

$$l_3 = \frac{h}{\sin\theta} + \frac{2e}{\cos\theta} \left(1 - \frac{1}{\sin\theta}\right) \quad (2.5)$$

which gives a final strain ϵ_{op3} :

$$\epsilon_{op3} = \left(\frac{1}{\sin\theta} - 1\right) \left(1 - \frac{2e}{h\cos\theta}\right) \quad (2.6)$$

This last calculated strain (blue circles in figure 2.17) seems to give the best approximation and will be kept in the following.

The maximal strain before stiffening and blocking is now known for different parameters and can be used to limit the expansion of the matrix. If the material of the chevrons is stiff enough, the expansion stops at a strain of ϵ_{open} .

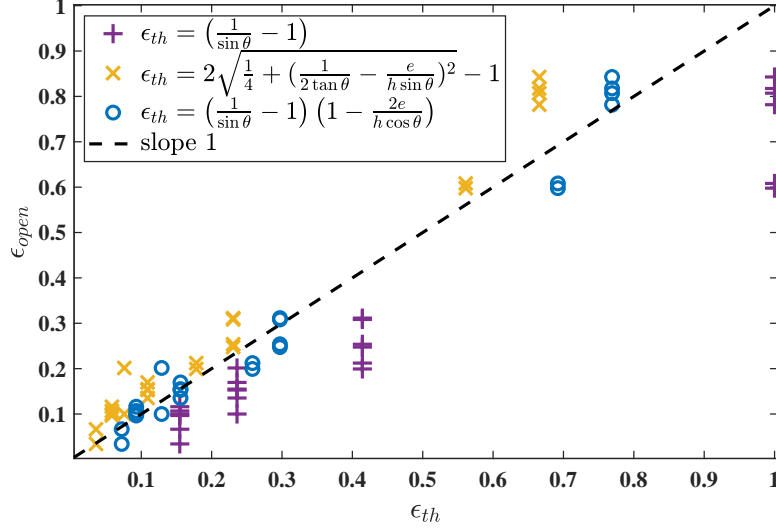


Figure 2.17 Measured blocking strain as a function of the prediction of several minimal models for chevrons without expanding matrix. The third computation in blue seems to be the closest.

We now give simple arguments to estimate if the chevrons may block the matrix expansion. Considering that the material follows Hooke's law, a naive estimate of the stiffness of a single extended chevron of width e and Young modulus E is obtained by assuming that it is stretched by $\frac{\Delta l}{l_3}$:

$$F = \frac{Nte}{\frac{h}{\sin \theta} + \frac{2e}{\cos \theta} \left(1 - \frac{1}{\sin \theta}\right)} E \Delta l \quad (2.7)$$

where F is the force measured over the entire sample, N the number of chevrons extended and Δl the elongation of the sample.

The slope measured on a force-strain curve should then be equal to:

$$k_{th} = NEt \frac{e \cos \theta \sin \theta}{h \cos \theta + 2e(\sin \theta - 1)} \quad (2.8)$$

with N the number of chevrons (depends on the density), t the thickness of the Mylar sheet, h , e and θ described in figure 2.6.

The stiffness is estimated from the force-strain curve as the coefficient of the first slope after the steep variation (figure 2.15). Plotting the measured stiffness k_{meas} as a function of the coefficient $\frac{tNe \cos \theta \sin \theta}{h \cos \theta + 2e(\sin \theta - 1)}$, the slope should be equal to the Young modulus E of the sample. For straight lines, i.e. when $\theta = \frac{\pi}{2}$ the measured effective Young modulus is around 1.2GPa, which corresponds to the typical Young modulus of Mylar. For chevrons that are not initially straight lines and have an angle lower than $\frac{\pi}{2}$, the effective Young modulus measured is about 0.46GPa which is significantly lower than the expected value for Mylar. The deployed chevrons seem to be weaker than the equivalent with straight lines. However, when the chevrons are totally open, the sample is much more rigid than at in the initial unstretched state.

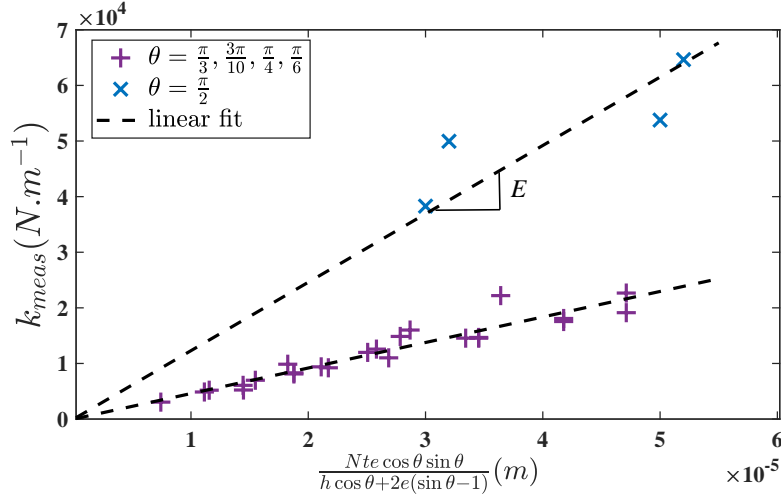


Figure 2.18 Measured rigidity for the different samples plotted as a function of a geometrical coefficient in order to get the Young modulus. If the material follows Hooke's law, the slope corresponds to the Young modulus. For $\frac{\pi}{2}$ (blue crosses) we measured $1.2 \cdot 10^9$ Pa. For chevrons, we find a smaller effective modulus $E^* = 4.6 \cdot 10^8$ Pa.

The purpose of the chevrons is to let the matrix expand before reaching ϵ_{open} , then block it in a final state where the chevrons are fully deployed. But are they correctly designed for these tasks ?

Let us compare the stiffness of the expanding matrix to that of the chevron layers that we have studied. Imagine that the network is embedded in the expanding matrix with the process detailed in section 2.2.3. The test samples used are approximately 15mm in height, 50mm in width and 4mm in thickness. The Young modulus of the silicon elastomer is approximately 1MPa. The stiffness is thus equal to:

$$k_{elast} \sim \frac{50 \cdot 10^{-3} \times 4 \cdot 10^{-3}}{15 \cdot 10^{-3}} 10^6 \sim 10^4 \text{ N.m}^{-1} \quad (2.9)$$

Chevrons experience two regimes, the deployment phase and the blocking phase. Taking the higher slope in the force-strain curve in the deployment phase gives a stiffness k_{net} about $4 \cdot 10^2$ N.m⁻¹ in our experiments. In this regime, the matrix is much stiffer than the network. As a consequence, the expansion of the matrix should not be influenced by the presence of the chevrons.

When chevrons are blocked, the stiffness k_{netb} is between $4 \cdot 10^3$ N.m⁻¹ and $2 \cdot 10^4$ N.m⁻¹ (figure 2.15). These values are comparable to the expanding matrix and should thus limit the expansion of the matrix.

Finally, chevron patterns let the matrix expand until ϵ_{open} and then strongly limit the strain which may add strength to the material. We now test the behavior of the hybrid system (matrix+chevrons) and characterize the deformation of the samples as a function of the distance h between the thick lines, the angle θ of the chevrons, the thickness e of the chevrons and the spacing a between the chevrons

Untethered shape morphing by phase transition

(figure 2.6 (left)). For that, networks of parallel lines connected with aligned chevrons are embedded in the expanding matrix.

2.3.3 Parallel lines and aligned chevrons

We now consider the influence of the different geometric parameters of the embedded chevrons pattern on the expansion of the matrix. As mentioned earlier, the expansion of the matrix depends significantly on the detail of the preparation of the emulsion and may differ from a sample to another. In order to get rid of the influence of the expansion of the matrix, the different parameters are tested on a single sample to be compared more easily. We thus design rectangular samples, with six lines separated by five rows of chevrons to measure the influence of the parameters of the networks only. The networks chosen consist in straight thick parallel lines separated by a distance h . All these thick lines are connected with chevrons with parameter θ , e or a that vary from one row to another (figure 2.19). The total thickness of the sample is 4 mm.

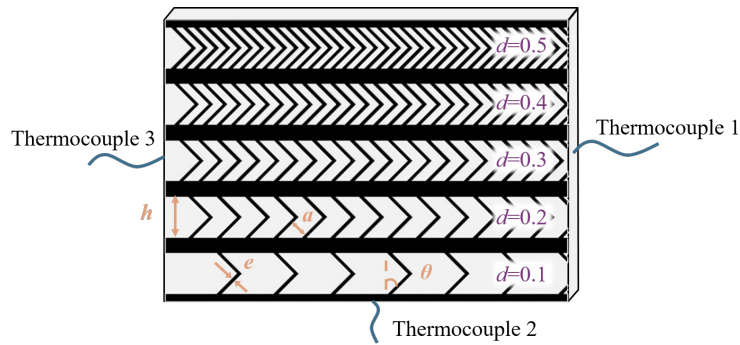


Figure 2.19 Drawing of a linear test sample to measure the influence of the chevron density d . The parameters $e = 1\text{mm}$, $\theta = \frac{\pi}{4}$ and $h = 10\text{mm}$ are kept the same from a row to another, only the spacing a is modified. From top to bottom, a increases, and thus the density d decreases. The temperature of the sample is recorded with the three thermocouples inserted inside the matrix.

These networks are embedded in the expanding matrix and the samples are suspended in the oven at 90°C (figure 2.12). When their inner temperature reaches 90°C , they are left for five minutes in the oven before the heating is stopped and the door opened to observe the cooling. The temperature of the sample and the oven are recorded over time and pictures are taken every 20 seconds. The strain is then recorded thanks to image analysis with a Matlab algorithm. The thick lines are painted in black whereas the chevrons are left transparent. The algorithm tracks the displacement of the thick parallel lines (i.e. the distance h) as a function of time or equivalently as a function of temperature (figure 2.20).

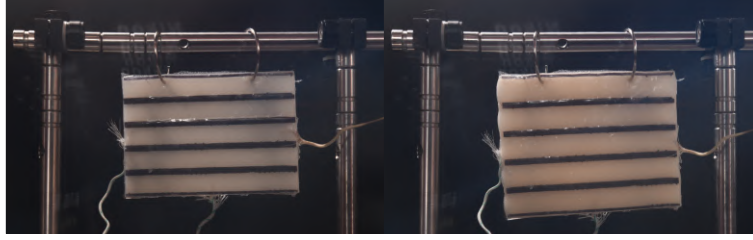


Figure 2.20 Experiment done with the sample from figure 2.19. The vertical strain of each row of chevrons is measured following the displacement of the thick parallel lines with a Matlab code.

2.3.3.a Influence of density d of the chevrons

We start by studying the influence of the density d of chevrons on the expansion of the material. According to section 2.3.2, they should not influence the expansion in their initial deployment phase. The thickness of the chevrons $e = 1\text{mm}$, the angle $\theta = \frac{\pi}{4}$ and the height between the lines $h = 15\text{mm}$ are kept constant from one row to another. Only the spacing a between the chevrons is modified.

The density is defined as : $d = \frac{e}{e+a}$. Two different networks with different density sets are used : $d = 0.1, 0.2, 0.3, 0.4, 0.5$ and $d = 0.05, 0.1, 0.2, 0.4, 0.6$.

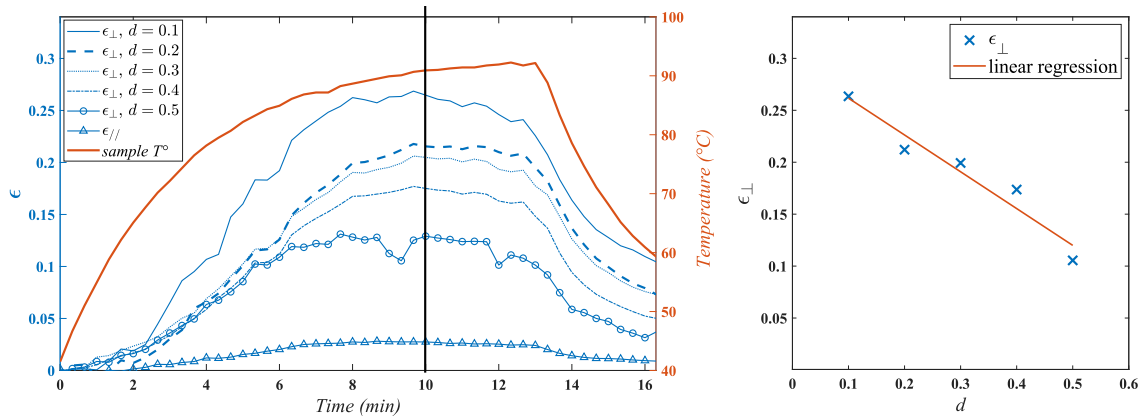


Figure 2.21 Left, measurement of the temperature (red) and strain of the sample (blue) from figures 2.19 and 2.20. The strain perpendicular ϵ_{\perp} to each row is measured for different densities as well as the strain $\epsilon_{//}$ parallel to the thick lines (left). Right, perpendicular strain at 10 min and 90°C (vertical black line in the left plot) as a function of the density d .

Using image analysis, the strain of each row is measured as a function of time and is plotted as a function of temperature (figure 2.21). We noticed that the quasi-plateau of temperature coincides with the strain plateau. The expansion rate seems to depend on the temperature as expected. All curves follow the same trend, except that the amplitude is different for the different densities.

The strain $\epsilon_{//}$, parallel to the lines (figure 2.21, triangles), is measured on the entire sample. It almost vanishes except when the limited adhesion between the matrix and the mesh allows for some sliding.

Untethered shape morphing by phase transition

The other blue lines in figure 2.21 correspond to the perpendicular strains ε_{\perp} of the different rows of chevrons. The maximal mean strain is measured on the plateau of each curve. As expected, the denser the network, the less it expands. The perpendicular strain can also be measured at all times and thus for different temperatures (an example of measurement at time=10min can be seen in figure 2.21, right). In the curves strain versus density, the strain corresponds at zero density to a network with only parallel lines. At a density $d = 1$, the strain should be zero and corresponds to the strain parallel to the thick lines.

In order to compare the influence of d for different temperatures, the global expansion of the sample must be known as a function of temperature. One possibility is to record the expansion rate as a function of temperature for samples without any networks or with only lines. As seen on figure 2.9 and 2.11, it is not very convenient and precise to measure strains on blank samples. Another solution consists in extrapolating the strain at zero density for each strain versus density curve at a given temperature, to extract $\varepsilon_{\perp 0}(T)$. This perpendicular strain in a case of zero density can be linked to the global expansion $\varepsilon_0(T)$ (expansion of the free matrix without any mesh embedded).

To find the relation between these two quantities, we consider a uniform pattern of parallel lines along the x direction, embedded in a matrix with isotropic stretch of $\lambda_0(T)$ (corresponding to the case of networks with zero density). Assuming that there is no stretching in the x direction ($\lambda_x = 1$), that the stretching is the same in the perpendicular directions ($\lambda_z = \lambda_y$), and that the volume is conserved ($\lambda_x \lambda_y \lambda_z = \lambda_0^3(T)$), the stretches parallel and perpendicular to the lines should be:

$$\lambda_{\parallel} = 1 \qquad \lambda_{\perp} = \lambda_0^{3/2}(T) \qquad (2.10)$$

In the limit of small deformation ($\varepsilon = (\lambda - 1) \ll 1$), the corresponding strains are:

$$\varepsilon_{\parallel} = 0 \qquad \varepsilon_{\perp} \sim \frac{3}{2} \varepsilon_0(T) \qquad (2.11)$$

where ε_0 is the global strain in absence of any constraint. As a result, the presence of lines blocks one direction of expansion and enhances the two others.

Thus in a case of small strain ($\varepsilon \ll 1$):

$$\varepsilon_0(T) \sim \frac{2}{3} \varepsilon_{\perp 0}(T) \qquad (2.12)$$

To determine the strain at zero density $\varepsilon_{\perp 0}(T)$, we performed a linear regression over the data points and extrapolate it at zero density (figure 2.22).

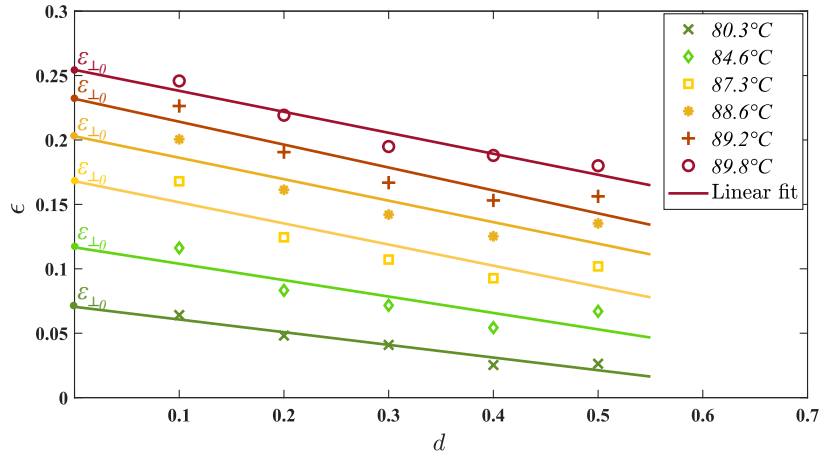


Figure 2.22 Strain of the chevrons rows with different densities and at different temperatures. For each temperature a linear fit is extrapolated at $d = 0$ to extract the global perpendicular strain $\varepsilon_{\perp 0}$.

Linear regression is chosen among other fitting possibilities because it offers a more robust way of normalizing the samples. Thus for each pictures, the measured strain can be now normalized by the global estimated value ε_0 . This strain normalization is convenient to compare the results at different temperatures and it also helps to compare the samples with each other. As mentioned before, due to variability in the fabrication process the expansion is different from one sample to another. However as the normalization is done for each sample, it is now possible to compare the samples with each other.

In order to measure the expansion due to the phase change as a function of the density, the data for the normalized strain are recorded for all temperatures when the sample is heating up. An average is done over five samples of the first set of density and two for the second. Keeping only the temperatures above 79°C (boiling point of ethanol) gives almost the same results as taking the normalized strain for all temperatures.

The material starts to expand for temperatures below the boiling point. This early expansion is probably due to the equilibrium vapor pressure or because some parts of the material are hotter than others. As the expansion is normalized, the influence of the chevrons should be the same and it seems to be the case.

The point at density $d = 1$ corresponds to the mean normalized parallel strain over all the samples. As explained earlier, the strain is not perfectly zero because the samples expand on the edges. Due to experimental issues, the networks often delaminate or slide on the edges which leads to a finite strain in the direction parallel to the lines.

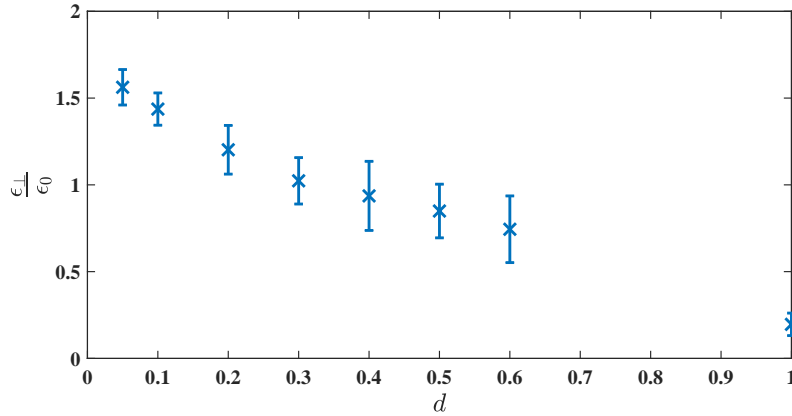


Figure 2.23 Measurement of the strain as a function of the density for a compilation of all the samples and all temperatures.

In the final state, the chevrons are never fully open, the maximal extension is thus never reached. The expectation from section 2.3.2 are not met. No additional strength is added by fully deployed chevrons (rigidity of Mylar). However, in the deployment phase, the force needed to open the chevrons is surprisingly linked to the density whereas it is much easier to open the chevrons than expanding the matrix. This might be due to the fact that the networks are embedded and that the material has to shear to open the chevrons: the deformation of the matrix and reinforcing network are strongly coupled.

On the final plot (figure 2.23), the trend is not perfectly linear but shows a dependency between the strain and the density: qualitatively, when the density increases, the strain decreases. Since the density of the chevrons fails to precisely predict the final strain, this technique cannot be used to program precise 3D-shapes. The dependency with densities seems not to be the same at low and higher density. Below $d = 0.3$ the slope is steeper, a small change in density has a bigger impact than above $d = 0.3$. At very high density a plateau seems to be reached. Experiments were not done above $d = 0.6$ because these configurations offers too small strains to be used for shape-changing objects.

2.3.3.b Influence of angle θ on the strain

We now focus on the influence of the angle θ of the chevrons. The density is set to $d = 0.4$ which gives better results. When the density is too low, the expansion of the matrix is too strong and may break the chevrons. Conversely if the density is too high, the final deformation is smaller and thus more difficult to measure.

Samples with different angles for each row are placed in the oven under the same conditions as in the previous section. The angles selected are : $\frac{\pi}{3}$, $\frac{3\pi}{10}$, $\frac{\pi}{4}$, $\frac{3\pi}{14}$, and $\frac{\pi}{6}$. The mean strain is measured on the plateau at 90°C . In this case, the samples can not be normalized intrinsically. Looking at the results (figure 2.24), the strain increases when the chevrons are more closed (smaller θ angle) and seems to reach a plateau.

For almost straight chevrons (large angle θ), the final strain seems to correspond to the maximal value ϵ_{open} , when chevrons are open at their maximum. As θ decreases, the expansion is however not strong enough fully open the chevrons. The angle of the chevrons seems thus to only play a role when the angle is large and that the chevrons are almost straight. When the chevrons are almost straight, they block the expansion and become the limiting factor. However when the chevrons are more closed, the expansion of the matrix is the limitation and the density seems to be the only factor influencing the strain as seen in the previous part.

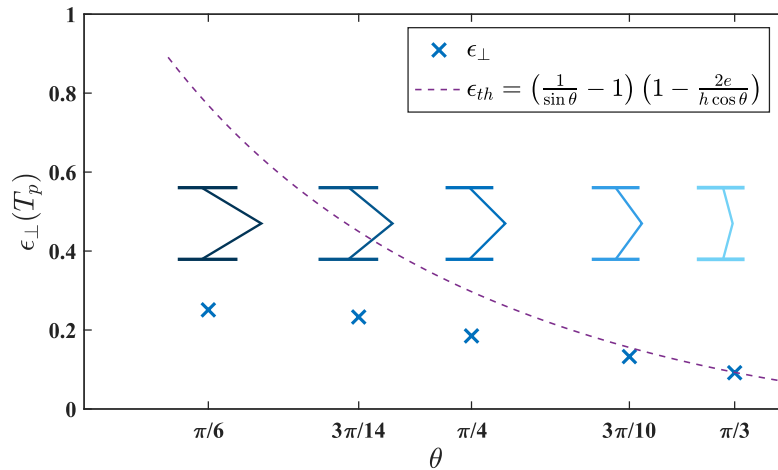


Figure 2.24 Measurement of the final strain of chevrons for different angles. The dotted line represents the maximal strain ϵ_{open} that the free chevrons can reach.

2.3.3.c Influence of thickness t of the Mylar sheet

In all previous experiments, the thickness t of the Mylar sheet used was maintained constant ($t = 30\mu\text{m}$). In this section, experiments are done with the same material but with thickness of $50\mu\text{m}$ and $100\mu\text{m}$ with the same parameters. Samples with chevrons of angle $\theta = \frac{\pi}{4}$ and density set $d = 0.1, 0.2, 0.3, 0.4$ and 0.5 are put in an oven at 90°C .

When the thickness of the network increases, the perpendicular strain is reduced as the network is stiffer. The samples remain more in plane when the networks are thicker and the measurements are cleaner. Normalizing the strain by the extrapolated zero density strain as in the part 2.3.3.a, the different samples can be compared even if the final perpendicular strain is different.

When the sample is thicker, the relation between the normalized perpendicular strain and the density is closer to linear (figure 2.25). The relation between the final perpendicular strain and the density d seems easier to determine in the case of thicker networks although the strain is smaller. To design 3D shapes, having a strong dependency is important but small strains limit the family of achievable shapes.

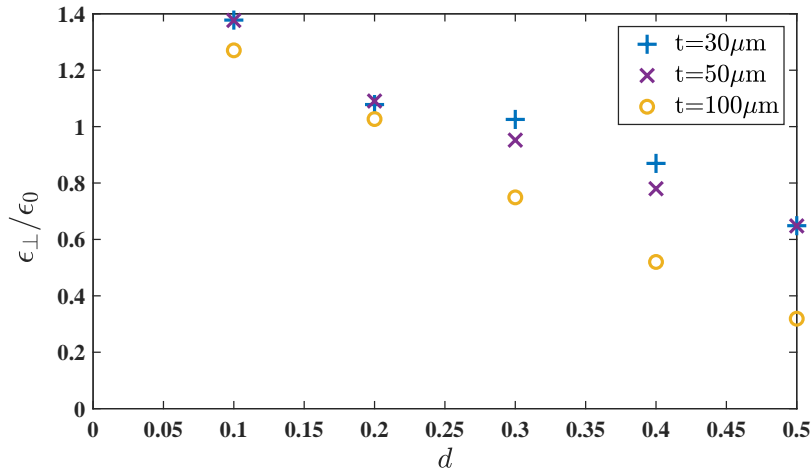


Figure 2.25 Network of chevrons with angle $\theta = \frac{\pi}{4}$ and density $d = 0.1, 0.2, 0.3, 0.4$ and 0.5 but with a different thickness t from a sample to another. The Mylar thickness selected are $30\mu\text{m}$, $50\mu\text{m}$ and $100\mu\text{m}$.

2.3.3.d Effect of temperature

We are now interested in the influence of the temperature of the oven on the induced global strain. We use chevrons networks with different densities to extrapolate a global strain for different temperatures of the oven (part 2.3.3.a).

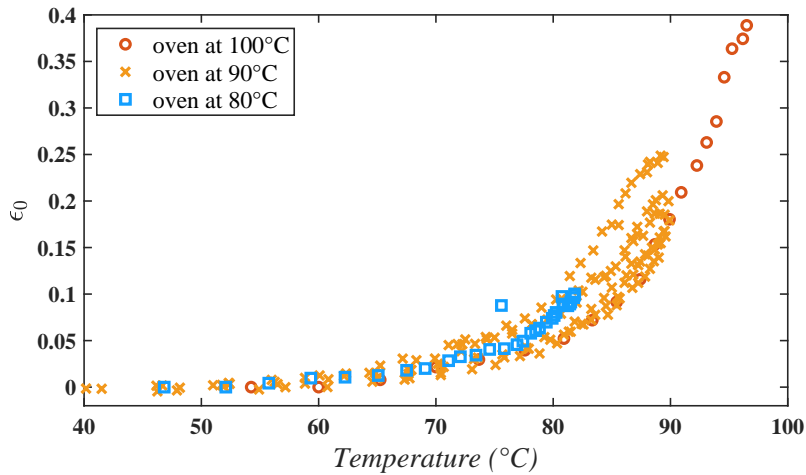


Figure 2.26 Global strain ϵ_0 as a function of the internal temperature for all the samples. The color represents the temperature of the oven when the sample is inserted.

Selecting the temperature of the oven at 80°C , 90°C or 100°C , gives similar responses of the material. In most cases the sample are heated in an oven at 90°C (figure 2.26, orange crosses), but the samples heated in oven at 80°C and 100°C tend to follow the same trend. The temperature of the oven does

not have a strong effect on the expansion of the sample, it only changes the final global strain. The temperature of the oven is set at 90°C in the experiments as a compromise between a good expansion of the material and a limited diffusion of ethanol.

This extrapolation of a global strain can also be used to determine a general trend $\epsilon_0(T)$ that does not depend on a specific sample. For each sample, the extrapolated global strain is recorded for each temperature on the same figure (figure 2.27). In order to determine the relation between the global strain ϵ_0 and the temperature, an exponential fit is superimposed to the data points recorded (figure 2.27 purple line). This approximated global strain as a function of the temperature $\epsilon_0(T)$ will be used in the next part when the normalization of the data cannot be done intrinsically.

On the same figure 2.27, the strain is also recorded while the temperature of the sample is decreasing (the oven is opened). The hysteresis may be due to the fact that the deformation is partially plastic or irreversible or that the temperature cooling and heating rates are different. Indeed, time is not present on the graph and temperature rates are not accounted for. In practice, samples are cooled down faster than they are heated up.

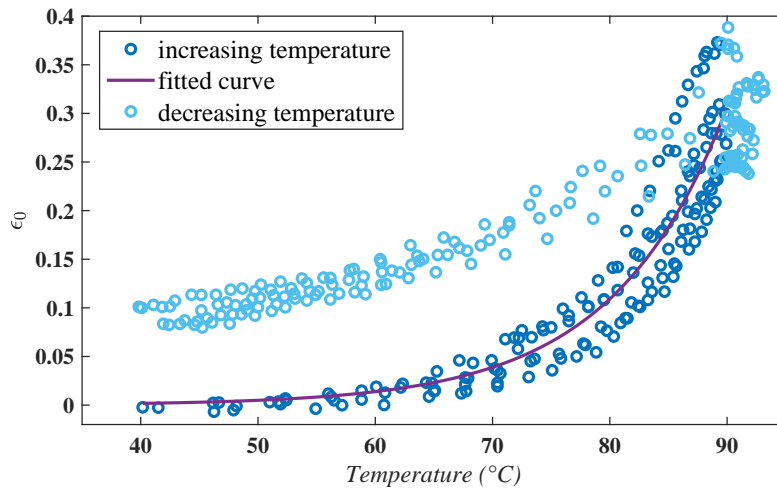


Figure 2.27 Global strain as a function of the temperature when the sample is put in an already hot oven and then when the temperature of the oven is dropped down.

To conclude this part with uniaxial deformations, we were able to provide correlations between final perpendicular strain and the density or angle of the chevrons. Thick lines seem to drive the deformation while chevrons seem to act at second order. The difference in strain for the different angles and densities is probably not strong enough to use it to create more complex shapes than in-plane deformation.

In order to create 3D-shapes, we will not rely on the change in density or on the angle of the chevrons but rather on the orientation of the thick lines which drives most of the deformation. The chevrons are conserved because they help maintaining the deformation in the plane of the network, preventing too large deformations in the thickness.

2.3.4 Programming 3D-shapes

One of the first goals of this PhD thesis is to design objects that can change shape upon activation. In the first section we tried to characterize a new material that undergoes a large expansion when heated, combined with an internal structure that selects the local direction of deformation. A qualitative understanding of the achievable deformations was possible.

The position of thick straight lines appears to be leading the deformation, the presence of the chevrons playing at a second order but helping smoothening the deformation. To create simple shapes with negative or positive Gaussian curvature, we were inspired by material with anisotropic deformations along “director fields”. We decided to use axisymmetric networks.

As a first attempt, the thick lines are arranged in concentric circles. These circles are connected with chevrons of equal angle and with the same thickness and spacing everywhere. As explained earlier, the matrix can only expand perpendicularly to the thick lines. In the case of the concentric circles, the strain vanishes along the perimeters (thick lines) and is maximal along the radii (perpendicular to the thick lines). The chevrons are identical on every ring, leading to an uniform strain in the radial direction. The concentric circles keep their perimeters but their distance to the center increases. As a consequence, they go out of plane and the surface deploys into a cone (figure 2.28).

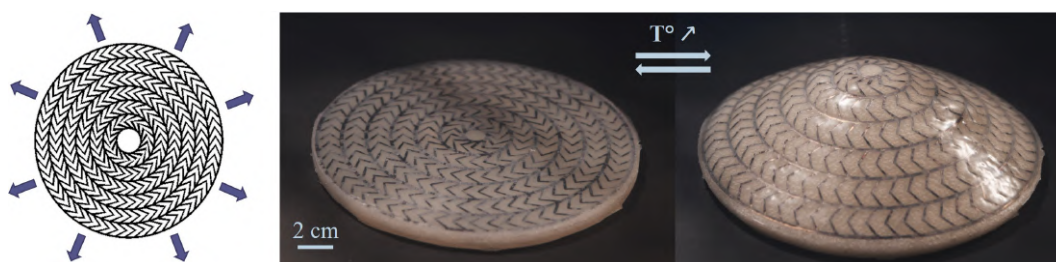


Figure 2.28 Network of chevrons with thick lines as concentric circles. When the temperature is increased, a conical shape emerges and goes back to the flat state when the temperature is lowered. On the left the Mylar network before being embedded in the matrix.

The lines can also be drawn along the radii and be connected by chevrons. The angle of the chevrons and their density are kept constant along the radius even if their length changes. In this case, the radial strain (parallel to the thick lines) is zero while the strain is maximal in the orthoradial direction (perpendicular to the thick lines). As in the previous case, the metric changes upon heating and a 3D shape emerges. The perimeters of the samples expand whereas the radii are preserved. This change in metric codes for an e-cone, the excess of length of the perimeters causing them to buckle (figure 2.29). In principle, the azimuthal positions of the lobes are random and could be changed as the network is axisymmetric. Once one shape is chosen it is usually difficult to change it if the sample is heated again: small defects and history determine the shape.

In these two designs (e-cone and cone), the position of the thick lines drives the deformations and the main role of the chevrons is to reduce the deformation across thickness. However it is possible to design relatively simple structures that use the properties of the chevrons to program shape morphing.



Figure 2.29 Network of chevrons with radial thick lines. When the temperature is increased, a shape of an e-cone emerges and goes back to the flat state when the temperature is lowered. On the left the Mylar network before being embedded in the matrix.

To prove that chevrons also have an impact on the deformations and that they can be used to design shapes, we design pattern relying either on the angle or density change and using only thick lines. The goal is to design samples with positive and negative Gaussian curvature: a helix and a shell.

A first attempt at programming these two shapes is made using only thick lines. In both cases, horizontal parallel thick lines are connected through a few vertical lines.

In order to get a helicoidal shape, a thick vertical line is drawn in the center of the sample (figure 2.30 (left)). The horizontal parallel lines limit the deformation in the horizontal direction. However the central backbone also blocks the deformation in the vertical direction. Thus on both sides, the matrix can expand freely perpendicular to the lines, extending the edges but without expanding in the center. The resulting shape observed in figure 2.30 might be reminiscent of a helix but the deformation appears irregular.

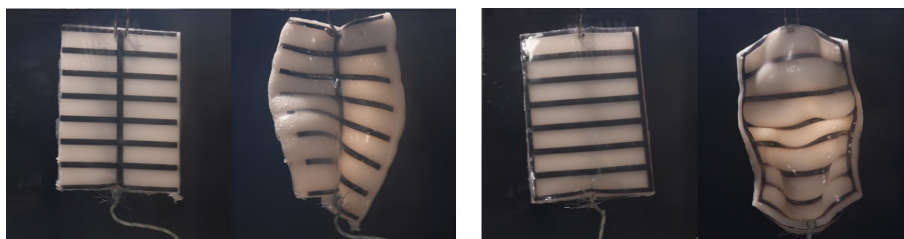


Figure 2.30 Horizontal thick lines with a vertical line in the center (left) or on the edges (right). When the temperature is increased, two different shapes emerges. The expected shapes (helicoidal and shell like, respectively) are not observed and the expansion does not seem homogeneous.

In order to obtain a shell, two vertical lines are drawn along the sides of the sample (figure 2.30, right). The horizontal parallel lines limit the deformation in the horizontal direction. The expansion is also blocked along both edges, the matrix can only freely expand in the center of the sample. The activated shape might be reminiscent of a shell divided in two parts. As in the case of the former

Untethered shape morphing by phase transition

backbone, the deformation is irregular and the shell exhibits two parts with opposite concavities. Upon further activations, the same shape will deploy: the material is likely damaged by its first cycle and will follow the same path in the following deployments.

The issue with the two last designs is that the change in strain is too abrupt. A smoother change in the strain should help obtaining more controlled shapes. Using chevrons helps in this way and changing their geometrical parameters allows to better control 3D shapes.

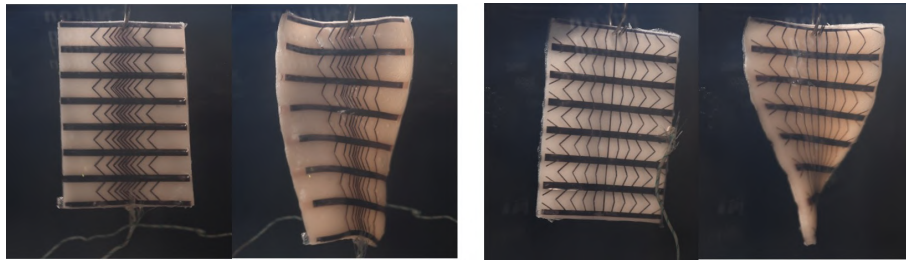


Figure 2.31 Networks with horizontal thick lines connected by chevrons with different angles or density. On the left, the density is higher in the center than on the edge. On the right, angles θ are lower on the edge than in the center. A helix emerges when the temperature is increased (right picture of each pair).

We use now chevrons as tool to control 3D shapes. The horizontal parallel thick lines are kept but the chevrons in each row change in density or angle depending to their position from the center of the sample.

First we focus on helices. To obtain more regular shapes than in figure 2.30, the target strain should evolve linearly along the width of the sample: smaller in the center of the sample, larger on the edges. If we consider that the final strain is almost linear with the density, placing chevrons with a density decreasing linearly from the center should lead to a helix (figure 2.31).

Alternatively, the angle of the chevrons can be changed instead of their density. The angle is linearly decreased from the center to the edges across the width. When the sample is heated, an helix deploys (figure 2.31 right).

These two ways of creating helices demonstrate that the density and the angle can be tuned to change shape and that the chevrons help regularizing the final shape. As the thick lines only drive general expansions, the chevrons help to refine the direction and the final shape.

For both helices, the density and angle are decreased from the center to the edges of the samples. The opposite can also be done: the density or the angle of the chevrons can be increased from the center. If the density of chevrons is increased from the center (figure 2.32 left) or if the angle of the chevron is increased from the center to the edge (figure 2.32 right), a shell shape emerges when the temperature is increased.

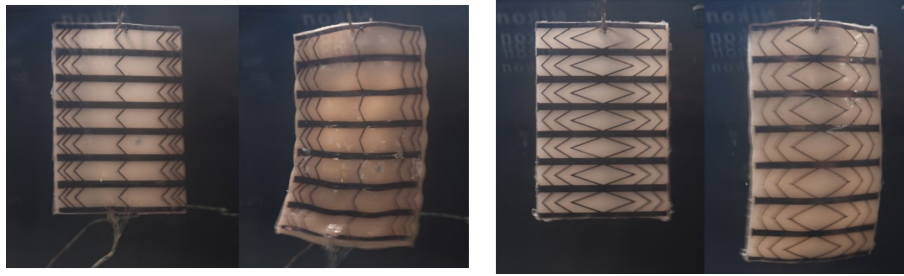


Figure 2.32 Network of chevrons with horizontal thick lines and chevrons with different angles or density. On the left, the density is low in the center and higher on the edge. On the right, angles θ are larger on the edge than in the center. A shell shape seems to emerge when the temperature is increased (right picture of each pair).

Thus, networks with lines and chevrons that are embedded in an expanding elastomeric matrix can drive a shape changes. Although drawing lines is a simple way to program shape change, other designs can be used too.

2.4 Diamonds network

In this section, another type of network composed of diamonds is tested. Why diamonds ? Looking around more carefully, they appear everywhere. From a facade, a fence or a card they are very present in the daily life. They are used either for their aesthetics (logo, decorations,...) or because they are deployable and can easily be open and close (fence, grids,...).

In the following, we will try to use such diamonds networks to create objects that change shape upon activation. The diamond cell is interesting because it undergoes a bi-axial deformation when activated. If the sides are inextensible (constant perimeter), the state of the diamond relies on a single degree of freedom as the sum of all angles is 2π .

As in the previous section, the network of diamonds is embedded in an expanding matrix. When activated, the matrix expands, which tends to maximize the area enclosed within each cell: diamonds evolve toward squares (figure 2.33). The length of one diagonal is thus increased whereas the other is decreased, providing extension and compression strains respectively. Interestingly, the anisotropy induced is larger than in the case of the lines.

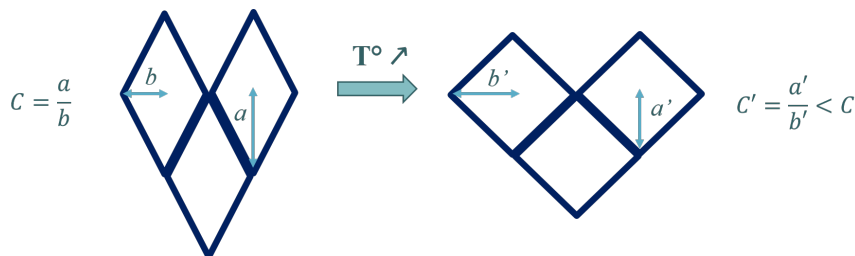


Figure 2.33 Activation of the diamonds upon inflation. As the area increases with the temperature, the half diagonal b extends while the half diagonal a contracts.

Untethered shape morphing by phase transition

As for the lines and the chevrons, before using the diamonds to create 3D shapes, the expansion of one unit cell has to be quantified. In order to understand how embedded diamonds behave inside a matrix, a pattern with identical aligned diamonds is used first. With this type of networks, when the temperature increases, the deformation is homogeneous and the samples deform in plane.

Contrary to the last section, the network are not tested alone with the Instron machine, they are directly embedded inside the matrix and tested in the oven.

2.4.1 Network of aligned diamonds

In order to understand the influence of the diamonds on the deformation of the sample, networks of identical aligned diamonds are embedded in an expanding matrix. They are placed in the oven at 90°C. The resulting deformation is measured and quantified by image analysis using Matlab.

From one network to another, different parameters are changed. The thickness of the network and the temperature are kept the same during all experiments, as the measures of the influence of these parameters has been done in the previous sections 2.3.3.d and 2.3.3.c .

The networks are simply parametrized by three parameters: the thickness of the diamonds e , the length of the side l and the aspect ratio $C = \tan \theta = \frac{a}{b}$ that is linked to the angle θ . The lengths $2a$ and $2b$ correspond to the diagonals of the diamonds with $2a$ corresponding to the diagonal opposite to the measured angle θ . In most cases, $2a$ is considered as the major axis and $2b$ as the minor axis (figure 2.34). The side length l is measured inside the diamonds and corresponds thus to the side length of the expanding material inside the diamonds.

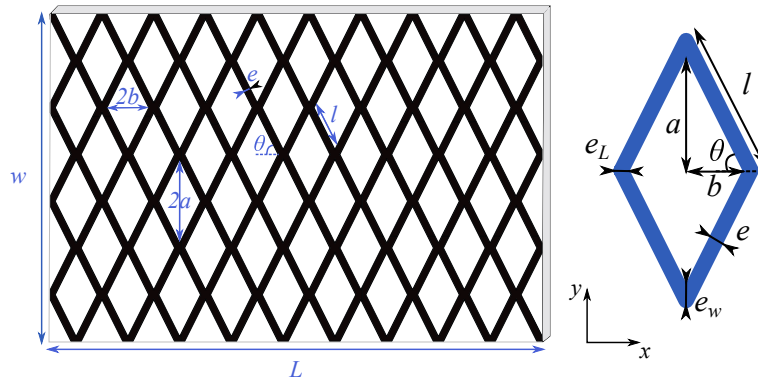


Figure 2.34 Test sample of length L and width w with diamonds of angle θ , side length l , thickness e and diagonals $2a$ and $2b$.

On the network, diamonds of equal angle θ are aligned in rows. The thickness measured perpendicularly to the side is e but they are laterally and vertically separated by the same distance $e_L = e_w$:

$$e_L = e_w = \frac{e}{\sqrt{2} \sin\left(\frac{\pi}{4} + \arctan\frac{1}{C}\right)} \quad (2.13)$$

The samples used have the same area wL with L the total length and w the total width. Knowing these distances and the other parameters it is possible to measure a density of lines for each sample. This density corresponds to the ratio of areas of the network with the total area of the sample.

$$\mathcal{D} = \frac{\mathcal{A}_{mylar}}{\mathcal{A}_{tot}} = \frac{1}{1 + \frac{b^2 C}{eh + b\sqrt{(e^2 + h^2)(1 + C^2 \sin(\pi - \arctan C - \arctan \frac{e}{h})}}}} \quad (2.14)$$

In all the experiments, the density \mathcal{D} is kept constant not to influence the measurement of expansion and to be able to compare the different samples between each other. As the density of lines is the same in all samples, the global expansion is expected to be the same as seen previously with the chevrons. Locally, the “same energy” is involved to push the different lines embedded in the different samples.

As in the experiment with the chevrons, the samples are put in the oven. The temperature is recorded with four thermocouples (one in the oven and three others in the sample) and pictures of the sample are recorded every 20 seconds. The heat treatment is the same as for the samples with lines and chevrons. The sample is put in a pre-heated oven at 90°C. When the sample reach 90°C, it is left 5min and the oven is finally switched off and the door opened to observe the cooling.

When the sample is heated, the diamonds tend to approach a square shape (figure 2.35). This behavior can be quantified by image analysis.

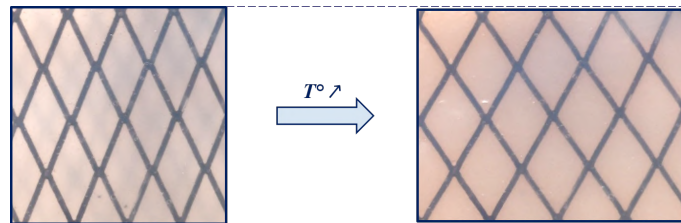


Figure 2.35 Diamond network embedded in the expanding matrix at room temperature (left) and 90°C (right). The diamonds seems to evolve into squares. On both pictures, the number of diamonds is the same but the heated sample is wider and slightly less high.

A Matlab algorithm follows the evolution of the diamonds in time. More especially, we measure their dimensions and aspect ratios. The diamonds networks are painted in black and the position of the corners of the diamonds is measured on each image. When a diamond shape (four corners) is recognized on the image (colored diamond in figure 2.36), the position of the point is taken into account. For each image, an average is done over all the detected diamonds to measure the length of the minor and major axes. The evolution of the total size of the sample is also measured.

On figure 2.36, we observe that the shape of the diamonds evolves with temperature. Diamonds tend to become square as mentioned previously.

Untethered shape morphing by phase transition

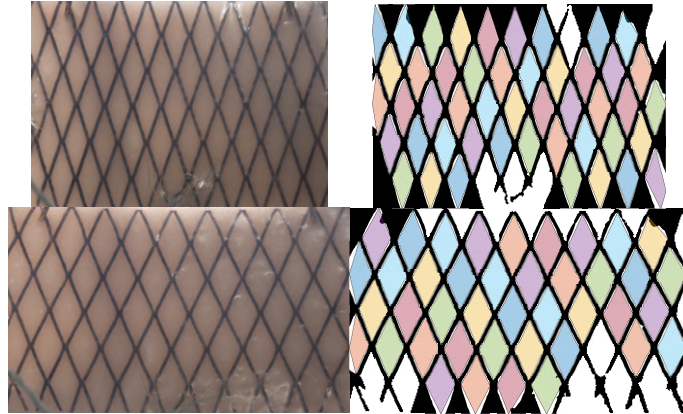


Figure 2.36 Diamond sample with $C = 3$, $e_w = e_L = 1\text{mm}$, $d = 0.28$ at room temperature (up) and 90°C (down). On the right of each picture the detection of the diamonds by the algorithm.

As in the case of chevrons, the evolution of the different dimensions of the system and the temperature are plotted as a function of time (figure 2.37). As assumed, the perimeter of the diamonds is rather constant over time (yellow circles in figure 2.37): the branches of the network remain unstretched. The evolution of the total length L and minor axis $2b$ are very similar. The two lengths increase with temperature and reach a plateau when the temperature reaches a quasi-plateau. They get shorter when the temperature decreases.

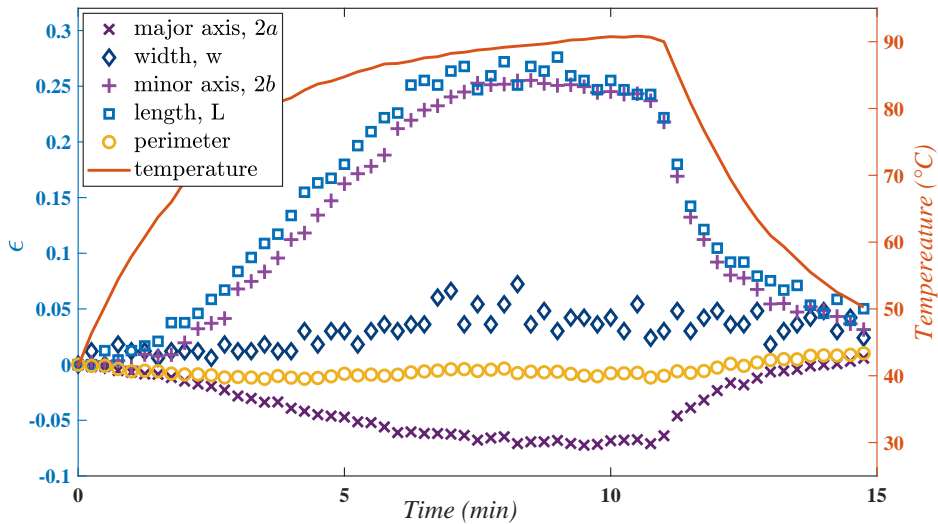


Figure 2.37 Diamonds network with $C = 2.5$. The strain is measured along the different directions of the sample when the temperature is increased. Evolution of the mean of the major and minor axes of the diamonds, of the length and the width as well as the evolution of the perimeter with temperature.

However, the major axis $2a$ and the width w do not follow a similar trend. The major axis evolves as expected: when the temperature increases, it shrinks because the minor axis stretches (if the square

shape is reached, the diagonals are equal). However the total width seems to remain constant when the temperature increases. As explained earlier with the chevrons, the networks tend to delaminate on the edges which lets the matrix expand freely on the edge. As a result, the material does not globally reduce its size in one direction.

For all networks, the strain of the diamonds in the direction of both diagonals can be measured as a function of the temperature. Most tests are done with the same density $d = 0.28$. Unlike the chevrons network with changing density, the diamonds network cannot be internally normalized as a single density is used. In order to compare the different temperatures, the approximated law $\epsilon_0(T)$ calculated in section 2.3.3.d is used.

We now try to predict theoretically the behavior of the different networks to compare it with the experiments. We consider the expanding matrix as a homogeneous material following a neo-hookean elastic behavior. Some restrictions are applied to this material when it expands due to the presence of the embedded network.

The reference state is taken before the expansion of the material and the actual stretches in the three directions of space are noted λ_x , λ_y and λ_z . When the sample is heated, we first consider that it reaches a new stress-free state with an isotropic expansion λ_0 . The effect of the network is taken into account in a second step. The material is considered incompressible which leads to:

$$\frac{\lambda_x \lambda_y \lambda_z}{\lambda_0^3} = 1 \quad (2.15)$$

Thus the elastic energy of the system can be written as:

$$\mathcal{E} = \frac{\mu}{2}(I_1 - 3) \quad (2.16)$$

with:

$$I_1 = \left(\frac{\lambda_x}{\lambda_0}\right)^2 + \left(\frac{\lambda_y}{\lambda_0}\right)^2 + \left(\frac{\lambda_z}{\lambda_0}\right)^2 \quad (2.17)$$

from incompressibility $\lambda_z = \frac{\lambda_0^3}{\lambda_x \lambda_y}$, so that:

$$\mathcal{E} = \frac{\mu}{2\lambda_0^2} \left(\lambda_x^2 + \lambda_y^2 + \frac{\lambda_0^6}{\lambda_x^2 \lambda_y^2} - 3\lambda_0^2 \right) \quad (2.18)$$

The stored elastic energy is zero if the material is allowed to expand freely : $\lambda_x = \lambda_y = \lambda_z = \lambda_0$. However, the presence of the internal network, frustrates expansion in some directions. If the sides l of the diamonds are considered inextensible:

$$\lambda_x = \frac{l_{x_{fin}}}{l_{x_{ini}}} = \frac{l \cos \theta_f}{l \cos \theta_i} = \frac{\cos \theta_f}{\cos \theta_i} \quad (2.19)$$

Untethered shape morphing by phase transition

where θ_i and θ_f are the initial and final value of the diamond angle. Similarly:

$$\lambda_y = \frac{\sin \theta_f}{\sin \theta_i} \quad (2.20)$$

The elastic energy can then be written as:

$$\mathcal{E} = \frac{\mu}{2\lambda_0^2} \left(\frac{\cos^2 \theta_f}{\cos^2 \theta_i} + \frac{\sin^2 \theta_f}{\sin^2 \theta_i} + \frac{\lambda_0^6 \cos^2 \theta_i \sin^2 \theta_i}{\cos^2 \theta_f \sin^2 \theta_f} - 3\lambda_0^2 \right) \quad (2.21)$$

The equilibrium angle θ_f minimizes \mathcal{E} and satisfies $\frac{\partial \mathcal{E}}{\partial \theta_f} = 0$:

$$\frac{\partial \mathcal{E}}{\partial \theta_f} = \frac{\mu}{2\lambda_0^2} \left(\frac{-\sin(2\theta_f)}{\cos^2 \theta_i} + \frac{\sin(2\theta_f)}{\sin^2 \theta_i} + \lambda_0^6 \sin^2 2\theta_i \frac{-4 \cos(2\theta_f) \sin(2\theta_f)}{\sin^4(2\theta_f)} \right) = 0 \quad (2.22)$$

$$4 \sin(2\theta_f) \frac{\cos(2\theta_i)}{\sin^2(2\theta_i)} = 4\lambda_0^6 \sin(2\theta_i) \frac{\cos(2\theta_f)}{\sin^3(2\theta_f)} \quad (2.23)$$

Which yields :

$$\frac{\cos(2\theta_f)}{\sin^4(2\theta_f)} = \frac{\cos(2\theta_i)}{\lambda_0^6 \sin^4(2\theta_i)} \quad (2.24)$$

When the expansion of the matrix is very large (i.e $\lambda_0 \rightarrow \infty$), the factor $\frac{1}{\lambda_0^6}$ tends toward zero which gives $\cos(2\theta_f) \rightarrow 0$ and thus $\theta_f \rightarrow \frac{\pi}{4}$. The shape that minimizes the energy of the expanding sample is the square as expected.

For each sample with a different θ_i , the measured angle $\theta_f(\varepsilon_0)$ is plotted in (figure 2.38) as a function of the global expansion of the material $\varepsilon_0(T) \sim \lambda_0 - 1$. Theoretical prediction (equation 2.24) are plotted as a dashed line: they all converge toward a final angle of $\pi/4$ when the expansion is large enough.

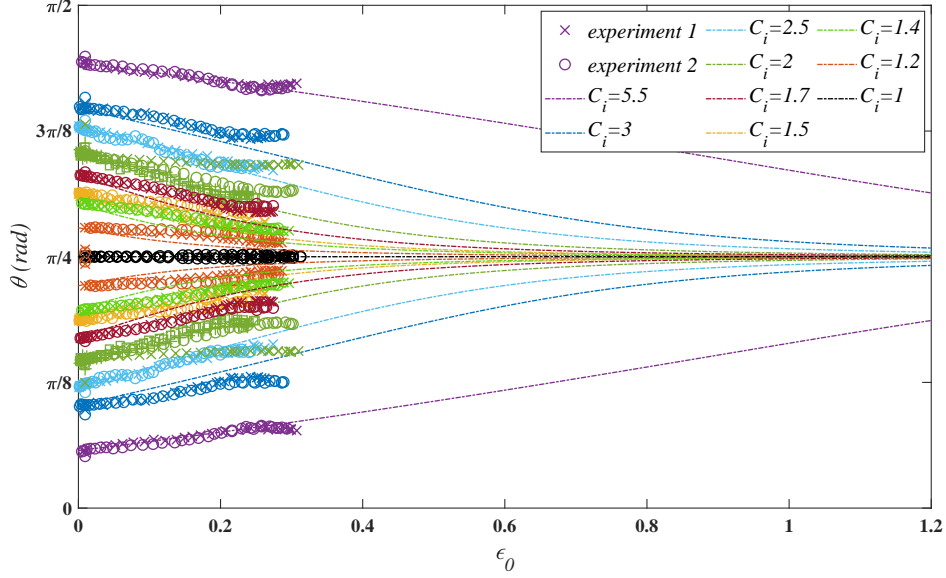


Figure 2.38 Evolution of the angle θ of the diamonds as a function of the global expansion of the matrix, for various values of the initial aspect ratio C_i . The theory in dashed line converges toward an angle of $\pi/4$.

On figure 2.38, we can see that the experimental points are in better agreement with the theory for large initial angles. Measurements are not easy to achieve as the strain ϵ_0 is not known for the samples and has to be extrapolated with the data from section 2.3.3.d.

At small deformation ($\epsilon_0 \ll 1$), the angle θ_f seems to vary linearly with the global strain ϵ_0 . Most of the recorded data points seem to be in this regime. Thus, at small strain, θ can be written as $\theta_i + A\epsilon_0$ with A a coefficient to be determined and $\epsilon_0 \ll 1$.

In these condition, the equation 2.24 leads to:

$$\frac{\cos(2(\theta_i + A\epsilon_0))}{\sin^4(2(\theta_i + A\epsilon_0))} = \frac{\cos(2\theta_i)}{(1 + \epsilon_0)^6 \sin^4(2\theta_i)} \quad (2.25)$$

$$\frac{(\sin(2\theta_i) \cos(2A\epsilon_0) + \sin(2A\epsilon_0) \cos(2\theta_i))^4}{\cos(2\theta_i) \cos(2A\epsilon_0) - \sin(2A\epsilon_0) \sin(2\theta_i)} = (1 + \epsilon_0)^6 \frac{\sin^4(2\theta_i)}{\cos(2\theta_i)} \quad (2.26)$$

Considering $\epsilon_0 \ll 1$, the development at first order gives:

$$\frac{(\sin(2\theta_i) + 2A\epsilon_0 \cos(2\theta_i))^4}{\cos(2\theta_i) - 2A\epsilon_0 \sin(2\theta_i)} = (1 + 6\epsilon_0) \frac{\sin^4(2\theta_i)}{\cos(2\theta_i)} \quad (2.27)$$

$$\frac{\sin^4(2\theta_i)}{\cos(2\theta_i)} (1 + 8A\epsilon_0 \cot(2\theta_i))(1 + 2A\epsilon_0 \tan(2\theta_i)) = (1 + 6\epsilon_0) \frac{\sin^4(2\theta_i)}{\cos(2\theta_i)} \quad (2.28)$$

We can finally deduce the expression for the prefactor:

Untethered shape morphing by phase transition

$$A = \frac{3 \tan(2\theta_i)}{4 + \tan^2(2\theta_i)} \quad (2.29)$$

We have now determined the relation between the global deformation ε_0 and the measured angle θ . In order to design shapes, it is more interesting to work with the strain of each diamonds instead of the stretch λ . Using the coefficient A we can now derive:

$$\varepsilon_y = \frac{\sin \theta_f}{\sin \theta_i} - 1 = \frac{\sin(\theta_i + A\varepsilon_0)}{\sin \theta_i} - 1 \sim \frac{\sin \theta_i + A\varepsilon_0 \cos \theta_i}{\sin \theta_i} - 1 = A\varepsilon_0 \cot \theta_i \quad (2.30)$$

$$\frac{\varepsilon_y}{\varepsilon_0} = \frac{3 \tan(2\theta_i)}{4 + \tan^2(2\theta_i)} \cot \theta_i \quad (2.31)$$

The strain ε_y is obtained from the measurements of the length of the diagonal $2b$ for each picture. It is recorded on samples with diamonds of different initial angles. These values are normalized by the law $\varepsilon_0(T)$ deduced from measurements taken in the previous section 2.3.3.d. These experimental normalized strains are then compared to the prediction of equation 2.31 in figure 2.39.

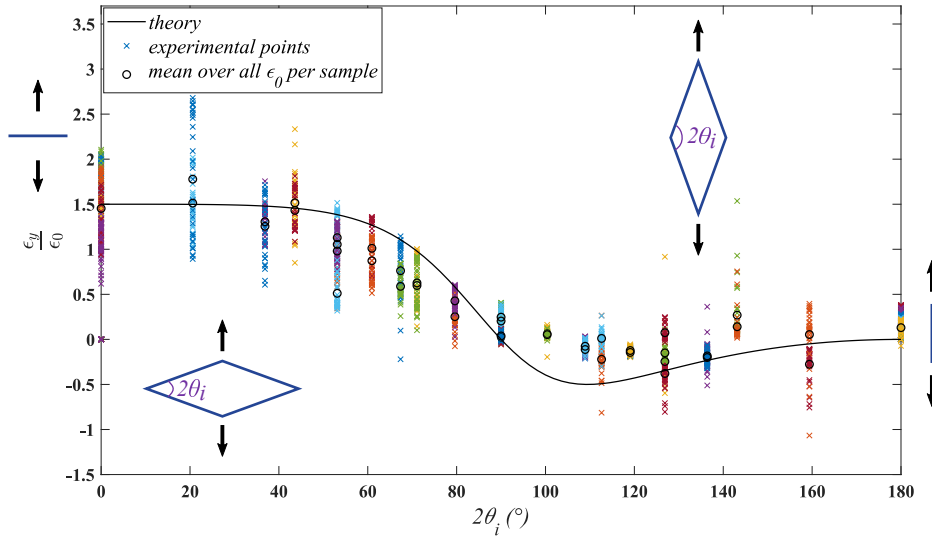


Figure 2.39 Measurements of the normalized strain of the diamonds as a function of the initial angle θ_i for small global strain ε_0 . Each color corresponds to a new sample.

In figure 2.39, the normalized strain is plotted as a function of $2\theta_i$ which corresponds to the total angle of the diamonds. Each color corresponds to a different sample and a different experiment. Each data point of the same color corresponds to the measurements of $\frac{\varepsilon_y}{\varepsilon_0}$ at different temperatures and thus at different ε_0 . The black circles correspond to the mean value of $\frac{\varepsilon_y}{\varepsilon_0}$ for each sample tested. The points at 0° and 180° correspond to the measurements along the line and perpendicular to the lines at zero density for the samples with chevrons tested in part 2.3.

As in figure 2.38, the experimental points better fit the theory for relative large angles. When the initial shape is close to a square, the strain measured is lower than the one predicted.

The difference between the theory and the experiment can be explained by the fact that the expansion of the sample cannot be determined intrinsically for each samples. The value of ϵ_0 is deduced from precedent experiments and may not correspond to the actual global strain of the samples as the variability in the expansion of the matrix is significant from a sample to another.

In order to better predict the shape of the diamonds, the matrix should be prepared with a higher degree of repeatability and tested in a more controlled environment.

Even though the theory does not fit totally the experiments, it still gives a good idea of the deformation of the diamonds when the matrix is expanding. It provides at least the direction of the strain. The larger the initial angle, the larger the strain for an equivalent matrix expansion.

2.4.2 3D-shapes

While predicting the exact strain of the cells as a function of the initial angle is difficult, the direction of strain is known. Taking advantage of this information, diamonds can be arranged along certain director fields. To start with simple patterns, we use diamonds with similar angles.

As in the section 2.3 with the lines, by tuning the direction of expansion of the material, we can program shapes. As in the case of radial lines and circles, it is easier to deal with uniform strain along the desired direction. In order to have the same direction of expansion for the diamonds, the diamonds are arranged radially and point toward the center of the network and they should all share the same angle.

Following a classical result from geometry, the only manner to arrange such diamonds on a disk with constant angle is to use logarithmic spirals.

2.4.2.a Logarithmic spirals

When trying to find a way of paving the space with regular patterns, Nature has found different solutions. For example, the seeds of the sunflower move from the center following logarithmic spirals. Counterclockwise and clockwise spirals can be observed on figure 2.40 which delimits cells reminiscent of diamonds.



Figure 2.40 Corols of a sunflower. The seeds are organized as logarithmic spirals when they grow.

Examples of logarithmic spirals also appear in animals as in the iconic nautilus shell (figure 2.41) [95].

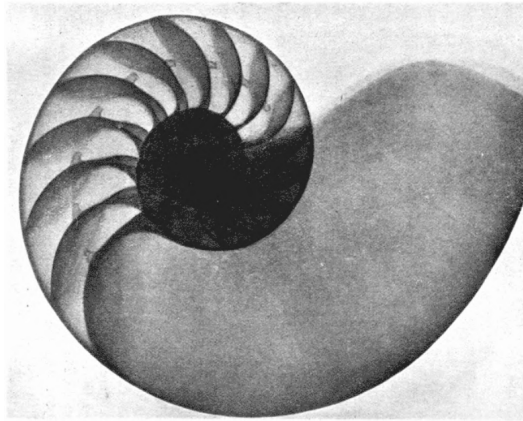


Figure 2.41 Nautilus shape follows a logarithmic spiral [95].

These particular spirals can be described in polar coordinates as:

$$r = ae^{\cot\beta\theta} \quad (2.32)$$

where β is the angle between the radius and the tangent to the spiral at any point (figure 2.42). It can be written in cartesian coordinates as:

$$\begin{cases} x = ae^{\cot\beta\theta} \cos \theta \\ y = ae^{\cot\beta\theta} \sin \theta \end{cases} \quad (2.33)$$

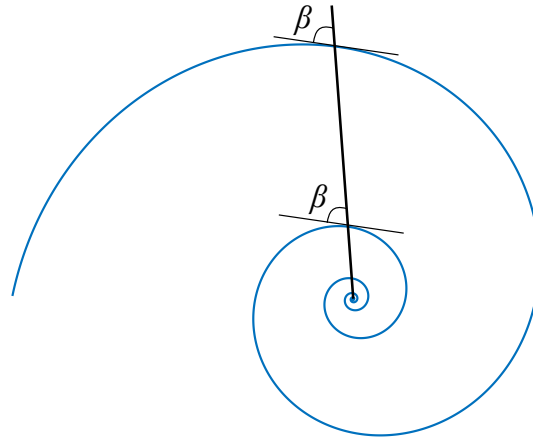


Figure 2.42 Logarithmic spiral with $\beta = \frac{7\pi}{16}$

This spiral is self-similar and thus keeps a constant angle β with any tangent to the curve. Logarithmic spirals are chosen over other curves for this property. If the angle is kept constant over the curve, it is then possible to draw diamonds with equal angle when moving from the center of the figure to the edge.

To create diamonds, a series of counterclockwise spirals is intersected with a series of clockwise spirals with the same angle β . Depending on the chosen angle β , the angles of the diamonds are different. Thus by tuning this parameters the shape of the diamonds can be determined.

Using these spirals to design samples is not easy because the width of the black spirals has to be tuned to keep the density d constant. For more simplicity, the diamonds are drawn one by one with the same angle but not using the fact that they belong to logarithmic spirals.

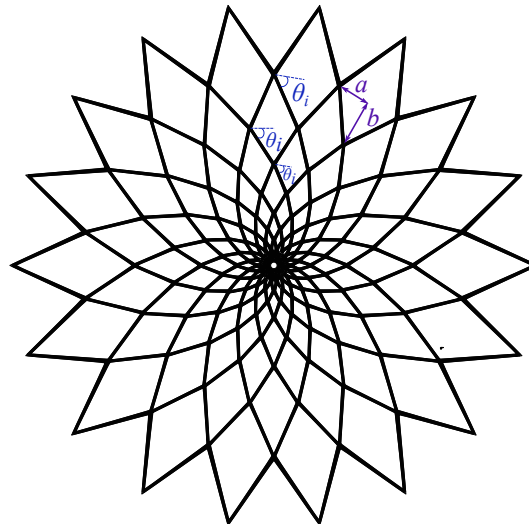


Figure 2.43 Example of diamonds delimited by logarithmic spirals with $\theta_i > \frac{\pi}{4}$.

The angle θ_i is measured at the center of the diamonds as shown in figure 2.43. By increasing the value of this angle θ_i , one switches from radial to orthoradial growth of the structure upon activation. As

Untethered shape morphing by phase transition

a result, a family of shapes from cones $\theta_i < \frac{\pi}{4}$ (i.e the ratio $C < 1$) to saddles $\theta_i > \frac{\pi}{4}$ (i.e the ratio $C > 1$) can be programmed. In the special configuration $\theta_i = \frac{\pi}{4}$ or $C = 1$, the sample should remain planar.



Figure 2.44 Diamonds network made with logarithmic spirals. For all the diamonds, the ratio $C_i < 1$. The diamonds are thus elongated along the perimeters and grow radially. When the matrix expands, a conical shape emerges.

When the initial angle of the diamonds is lower than $\frac{\pi}{4}$ ($C_i < 1$), the diamonds are oriented along perimeters. According to figure 2.39, for angles smaller than $\frac{\pi}{4}$, the strain is positive in the radial direction and negative in the orthoradial one. Thus when the matrix expands, the “perimeters” are reduced and the radii increase. These strains are not compatible with in-plane deformation and a conical shape pops off when the temperature is increased (figure 2.44).



Figure 2.45 Diamond networks made of logarithmic spirals. For all the diamonds, the ratio $C_i > 1$. The diamonds are elongated along the radii and grow azimuthally. When the matrix expands, a saddle shape emerges.

When the angle θ_i is higher than $\frac{\pi}{4}$, ($C > 1$), diamonds are elongated in the radial direction. According to figure 2.39, for such initial angle the strain is negative in the radial direction and positive in the orthoradial one. When temperature is increased and the matrix expands, the “perimeters” get longer and the radii shorter. This excess of length on the edge is only compatible with a saddle shape (figure 2.45).

Thus by changing the angle of the spirals, we showed that is possible to obtain both positive and negative Gaussian curvature surfaces. We did not used the differences between diamonds but the principal directions of positive strain of the diamonds according to their angles.

Another solution consists in keeping the same orientation for the diamonds but changing the angle of each one.

2.4.2.b Continuous variation of the diamonds angle

In the previous section, we used logarithmic spirals to define diamond cells. By intersecting a series of shifted curves of the same function and their mirror image, diamonds are also drawn. The simplest example is a linear function, which leads to the regular array of identical diamonds used as test samples in section 2.4.1. This particular pattern causes in-plane deformation when the sample is heated.

If the orientation of the diamonds does not spatially change, the angle have to change and the chosen function has to be non-linear. In order to obtain helices and shells as in section 2.3.4, the angle of the diamonds must evolve gradually from the center to the edges of the sample.

We first use exponential functions:

$$y = Cxe^{\frac{x}{b} \ln s} \tag{2.34}$$

with C the ratio of the central diamond, b the half diagonal in the x direction for all the diamonds and s the step used to decrease or increase the angle of the diamonds.

Each curve is then shifted by a distance $2b$ in the x direction in order to get a succession of curves. Diamonds are defined by the intersection between this family of translated curves and their mirror image. Doing so, half of the network is drawn (from the center to the edge), the other half is drawn by symmetry (figure 2.46).

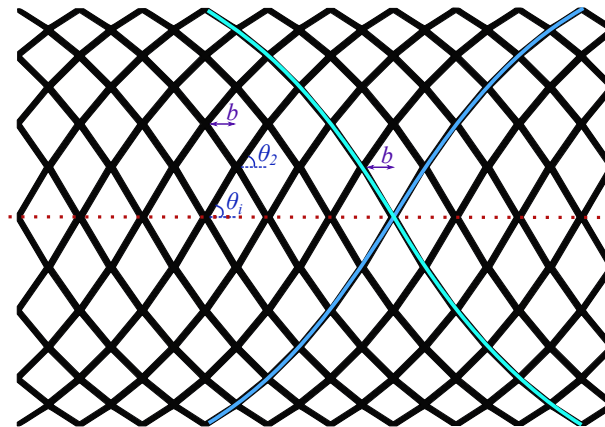


Figure 2.46 Diamonds network with changing angles according to the function 2.34. The initial ratio is $C = 2$, $s = 0.93$ and $b = 4.5$. As $s < 1$, the angles decrease as they go far from the center ($\theta_n > \theta_{n+1}$ with $n = 1$ at the center line).

The angles of the central diamonds are chosen first, while the dimensions of the sample and the number of the diamonds gives the half diagonal b . Finally the value s indicates if the angles increase or decrease when going away from the median of the figure. If $s > 1$ (figure 2.46) the angles of the diamonds increase, if $s < 1$, the angles decrease. The value of this parameter also controls the amplitude

Untethered shape morphing by phase transition

of the shape change of the diamonds.

When the aspect ratio C is higher than 1 along the median ($\theta > \frac{\pi}{4}$) and smaller than 1 along the edges, the perpendicular strain is positive along the center line and negative along the edges. The length mismatch lead to a shell shape (figure 2.47).

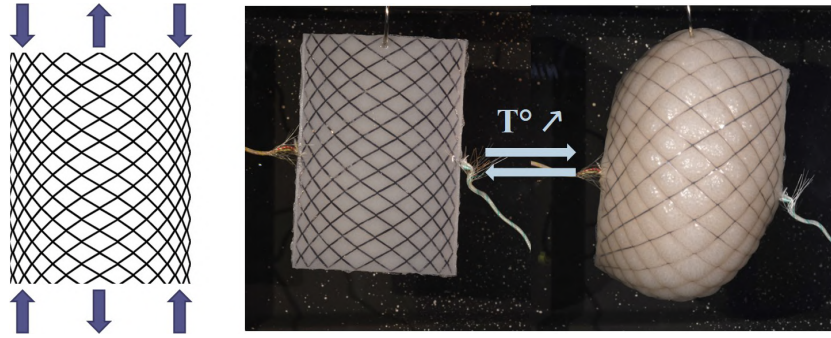


Figure 2.47 Diamonds network following the function 2.34, an exponential variation. The ratio in the center is $C = 2$, the step value is $s = 0.93$, the half diagonal is $b = 3.7\text{mm}$ and the width of the walls is $e = 0.7\text{mm}$. When the sample is heated a shell emerges.

Conversely, if the ratio C is lower than 1 at the center and higher than 1 on the edges, the perpendicular strain is positive on the edges and negative along the center line. The excess length on the edges when the matrix expands leads to the emergence of a helicoidal shape (figure 2.48).

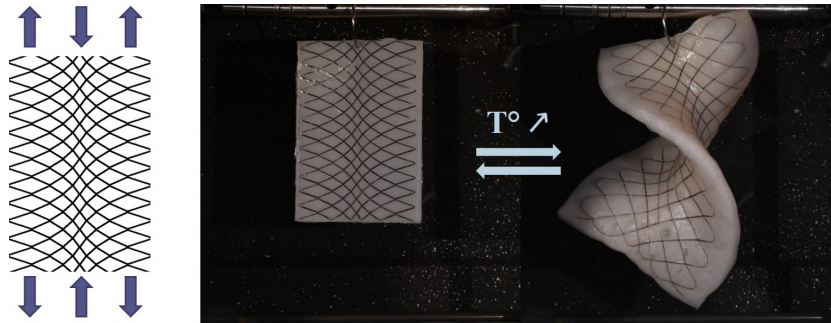


Figure 2.48 Diamonds network following the function 2.34, an exponential variation. The ratio in the center is $C = 0.8$, the step value is $s = 1.2$, the half diagonal is $b = 3\text{mm}$ and the width of the walls is $e = 0.7\text{mm}$. When the sample is heated an helix emerges.

In the examples used before, the exponential function can be replaced by a power law:

$$y = \frac{C}{b^{(s-1)}} x^{(s)} \quad (2.35)$$

The pattern looks similar but the evolution of the angle is different. As in the previous example, an initial ratio C has to be chosen for the central diamonds. Then the choice of the parameter s will decide if the angles of the diamonds increase or decrease when they go away from the center. By following the

same principle as the examples showed above it is possible to obtain shell (figure 2.49) and helicoidal shapes (figure 2.50).

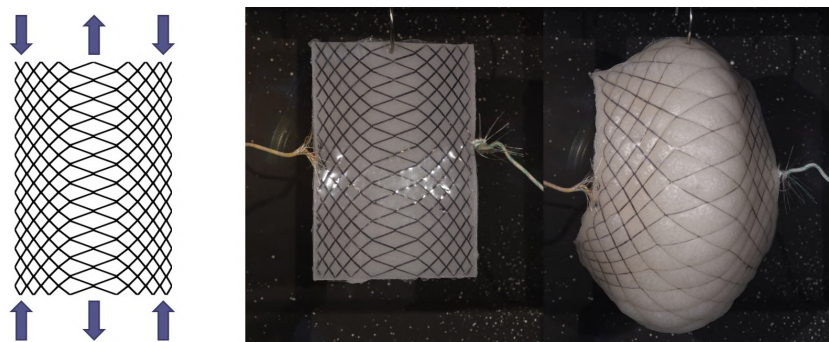


Figure 2.49 Diamonds network following the function 2.35, a power law variation. The ratio in the center is $C = 3$, the step value is $s = 0.59$, the half diagonal is $b = 3.5\text{mm}$ and the width of the walls is $e = 0.7\text{mm}$. When the sample is heated a shell emerges.

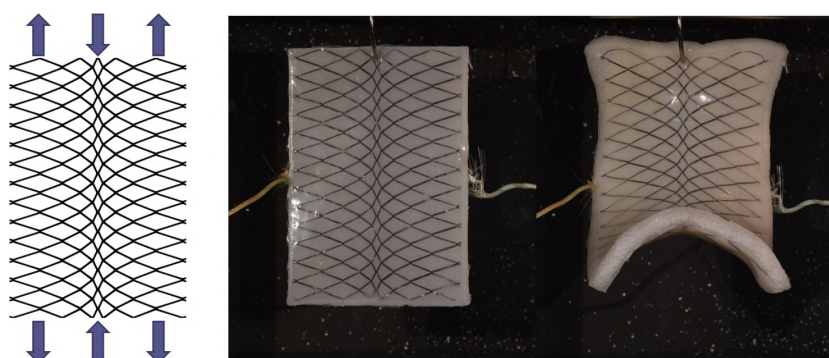


Figure 2.50 Diamonds network following the function 2.35, a power law variation. The ratio in the center is $C = 0.7$, the step value is $s = 1.7$, the half diagonal is $b = 3.2\text{mm}$ and the width of the walls is $e = 0.7\text{mm}$. When the sample is heated the beginning of a catenoid emerges.

In both cases, the diamonds tend to become squares but they stop before reaching the square shape. For high strains it seems that it takes less energy to plastically stretch the network instead of deforming it. It can be explained by the fact that the matrix is embedded and thus the deformation of the sample leads to a lot of shearing in the material.

2.5 Conclusion

In this chapter, we have shown how to use the giant expansion provided by liquid-gas phase transitions and created untethered objects that can evolve and change shape when temperature is varied. The active material used undergoes a very large but uniform and isotropic expansion upon heating. We have therefore embedded thin but inextensible cellular networks to impose the local direction of expansion. Changing the geometry of such networks allows us to direct shape changes, with positive

Untethered shape morphing by phase transition

or negative Gaussian curvature. These objects are quite unique: they have a relatively high stiffness (compared to morphing gels), and are still capable of extracting from the environment sufficient energy to power their large change of shape.

We however found that it is difficult to accurately program the final shape. We could not calibrate the material response with sufficient precision, as the experiments were not fully reproducible: when the sample are heated, they expand, but not all by the same amount, whereas a precise control of expansion is key to program 3D shapes. The behavior of such samples depends on too many parameters to offer fully reproducible experiments: temperature, temperature rate, the storing method before experiment, resting time between the fabrication process and experiment... The use of ethanol (that is not perfectly retained in the matrix) seems to be the main source of inconsistency in the process but it is difficult to find a liquid that meets all technical and safety requirements.

However we could imagine using the same concept with a different swelling mechanism (e.g. hydrogel responsive to pH or temperature [50, 51, 96] with very large expansion) adapted to small scale structures. We can envision embedding 3D-printed (with a printer such as Nanoscribe) networks in gel sheets, and build shape-changing devices at small scale, capable of interacting mechanically (capturing, applying forces) with micro-systems such as living cells or bacteria.

In the following chapter, we will further explore the geometries of pattern that we found to be efficient in this study, and create shape-shifting structures with other types of actuation.

Chapter 3

Changing shape by closing cellular structures

In the previous chapter we described how a mesh of diamonds embedded in a expanding matrix can dictate the final 3D shape of a composite structure. In this chapter, we propose to “close” diamond frames, which similarly results into a large biaxial deformation. As a consequence, an initially flat frame may adopt a complex 3D shape that can be programmed.

Contents

3.1	Introduction	68
3.2	Fabrication process	69
3.2.1	3D printing of structures	69
3.2.2	Selecting the final angle: blocker mechanism	72
3.3	Programming with blockers	74
3.3.1	Aligned diamonds with different blockers	75
3.3.2	Axisymmetric actuation	76
3.3.3	General inverse problem	82
3.3.4	Programming the curvature	84
3.4	Mechanical properties of cellular plates	85
3.4.1	Mechanical properties under traction/compression	85
3.4.2	Mechanical properties: bending of cellular networks	91
3.5	Activation with vacuum	96
3.5.1	Network of aligned diamonds under vacuum	97
3.5.2	3D shapes with vacuum	102
3.6	Rectangular unit cells	104
3.6.1	3D shapes with angular sectors	106
3.6.2	3D shapes from logarithmic spirals	107

3.1 Introduction

In the previous chapter, we have shown how a material that undergoes a large but featureless expansion sees its deformation constrained and guided by an internal cellular structure.

In this chapter, we wish to study the shape-changing properties of such structures by themselves, when they are stiff enough to carry loads. Instead of cutting the network out of a very thin sheet, the samples are now 3D-printed to a thickness on the order of a centimeter (figure 3.1, bottom right).

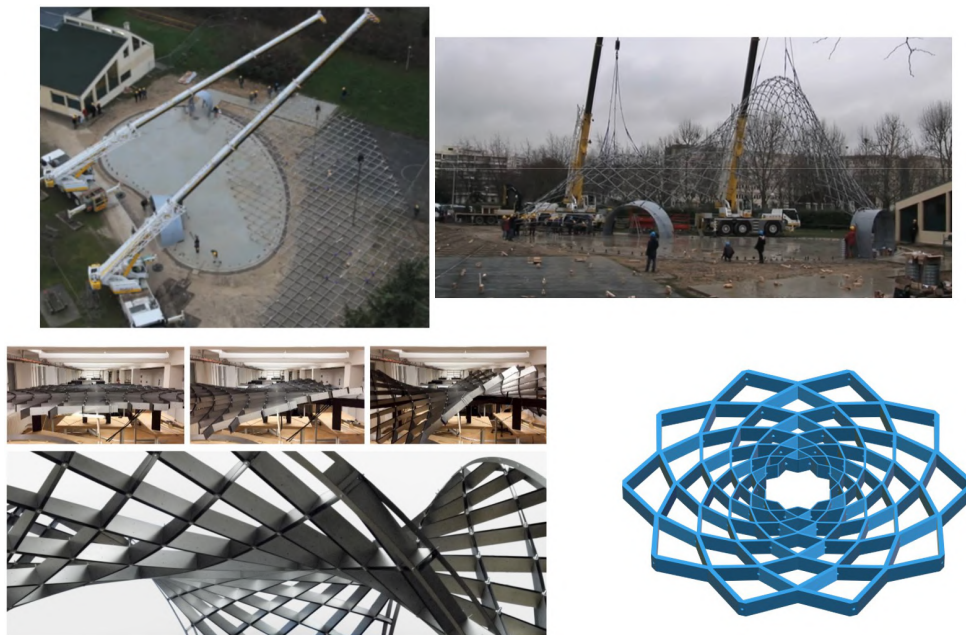


Figure 3.1 Top: Example of gridshell when it is flat (left) and deformed elastically with boundary conditions (right) (Cathédrale Ephemere de Créteil from [97]). Bottom left: an asymptotic gridshell pavillon [98], before and after being activated. Right: example of a 3D printed sample used in the chapter.

The structures that we now consider are visually similar to gridshells (or pantographs) as illustrated in figure 3.1. Gridshells [99] are composed of a grid network of flexible beams assembled with rotational joints in a flat, typically square pattern. They were introduced by architects (first by V. Shukhov, and famously by F. Otto) as an efficient way to construct shells: a crane pulls up the network initially laid flat on the ground. The structure may adopt a variety of shapes because the rotation at the connections is left free. When the desired shape is obtained, it is fixed by locking the joints. Sometimes, a third family of beam is introduced to increase the stiffness of the system.

A very important difference is that in gridshells, the joints allow free rotation at each connection point,

whereas the system of interest here is a single piece of material, with no rotational parts, so that all deformations involve elastic bending energy of the beams of the network.

In this sense, our system is closer to the “mechanical metamaterials” that were recently developed. Metamaterials are architected materials that are most of the time composed of periodically arranged unit cells, designed to have effective properties [19] different from the material they are made of. A very successful technique consists in designing an assembly of rigid blocks that can rotate around a flexible connecting ligament. The coordinated internal rotation of several neighboring blocks can produce a large in-plane expansion (or contraction).

Meta-materials structures were designed for a variety of properties: controlling the global mechanical response [19] or the Poisson ratio [100], providing large in-plane contraction [101]. Relatively few studies consider 3D shape-morphing [4]. A beautiful example of shape-changing meta-material is obtained by the snapping of all the internal patterns [83] into expanded (open) stable states.

Our cellular networks require less manufacturing precision than the fine rotational ligaments in metamaterials, and we expect them to be more robust. Because they are composed of slender members, they occupy a very low surfacic density in the deployed state, and we may expect them to be capable of huge change in area, and very large strains. However their deformation involves the bending of their beam components, and is more complex.

In this chapter we will first study the geometry and mechanics of large in-plane deformations of uniform 3D-printed diamond-shaped networks.

We then ask if contraction of controlled amplitude can be programmed and distributed spatially, and show how axisymmetric 3D shapes can be obtained when the material is activated by the tension of internal wires. We then turn to the question of how to program arbitrary shapes.

Finally, we show how pressure differences may also activate shape changes, a concept that we extend to other type of networks.

3.2 Fabrication process

3.2.1 3D printing of structures

In the previous chapter, networks were cut out of Mylar sheets. Such 2D meshes exhibit strong resistance when stretched, but the thin beams separating the nodes tend to buckle out of plane under compression. In this chapter, we consider cellular plates with walls of height h (the thickness of the plate) much larger than their thickness e . Although such cellular samples may undergo global buckling, the deformations of the cell walls remain in plane. In this section, the networks are printed with a regular fused filament 3D-printer (Artillery Sidewinder). In this 3D printer, filaments with different properties can be introduced. The most commonly used filament in open 3D printer is the PLA (polyactic acid) for its strength. This recycled material is commonly used in the plastic industry in general because it is biodegradable by industrial processes, even if the pigment added in the 3D printed filaments may alter

Changing shape by closing cellular structures

this property. In addition, printing with PLA is relatively easy because the filament is rigid and can be extruded at a relative low temperature (200 °C). The alternative to PLA for rigid filament is ABS, but as it is suspected to release nanoparticles when printed, we do not use it with open 3D-printer.

In addition to rigid filaments, flexible ones can be printed with this printer. Most of the flexible filaments are thermoplastic elastomers that possess both the elastic property of elastomers and the mechanical properties of thermoplastics. The two categories that are widely commercialized are TPU (Thermoplastic polyurethane) and TPE (Thermoplastic elastomer). Although they are both thermoplastic elastomers, they don't have exactly the same mechanical properties. As the composition of commercial filaments is not known and may vary, the properties of each filament change from one brand to another even if the declared shore and name are the same. We chose TPU over TPE because samples were less viscoelastic. Among the different brands, we selected the less viscoelastic material: Flexifill 92A from Fillamentum[®]. Using test samples, we have measured the Young modulus to be around 26MPa, and the Poisson ration around 0.3. These values look surprising (lower E and a Poisson ratio not equal to 0.5) but it might be explained by the fact that the test sample are printed and that the printing path has an influence on the mechanical properties of the samples.

In this first section, we focus on networks of identical diamonds aligned along lines and rows (figure 3.2). This type of networks enables in-plane deformations: shrinking along the closing direction and extension in the perpendicular one. Such networks are printed in TPU, with different geometrical parameters as shown in figure 3.2: the initial half-angle θ of the diamonds, the thickness e of the walls, the length l of the diamonds' side, and the height h of the network. The total length L and width w of the samples are related to the number of columns N_L and the number of rows N_w by $L = N_L 2l \cos \theta$, $W = N_w 2l \sin \theta$.

Samples are printed with different θ , l , e , h but the thickness e is difficult to control precisely due to the limited precision of the printer. As the thickness e is not precisely controlled in the printing process, the wall thickness is measured a posteriori. The height h of the walls is more precise: the height of the layers is driven by the motor step rather than extrusion parameters for the width of the walls. The angle θ is geometrically represented through the aspect ratio C of the diamonds. C is the ratio between the diagonals of the diamonds $2a$ and $2b$ respectively along the length and along the width, : $C = \frac{a}{b} = \tan \theta$ so $\theta = \arctan C$. When $C = 1$, diamonds are squares, when $C > 1$ the diamonds are elongated along w and if $C < 1$ they are elongated along L .

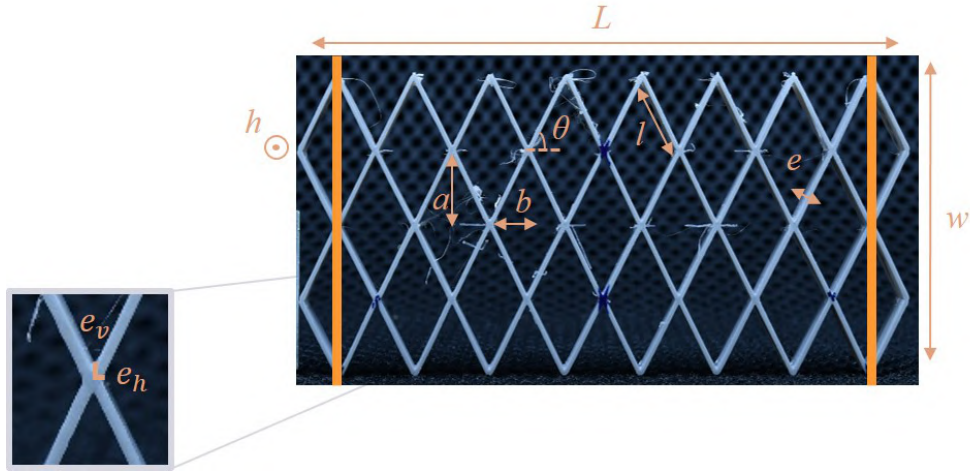


Figure 3.2 Example of a diamonds network and the different geometrical parameters: the half angle θ , the length of the diamonds l , the thickness of the walls e , the height of the walls h , the half diagonals a and b , the total length L and width w and the thickness of the separation between the diamonds e_v and e_h .

Paving space with diamonds might not seem to be complicated but there are actually many ways of doing it for diamonds with a finite thickness. Here the constraint is to keep the wall thickness and diamonds size constant. We have been using two different methods of drawing. In the first one, l is measured along the inside edge of the diamonds. Diamonds with a certain thickness e are laid out with the same distance vertically, $2e_v$, and horizontally, $2e_h$ (figure 3.2 left):

$$e_h = e_v = \frac{e}{\sqrt{2} \sin\left(\frac{\pi}{4} + \arctan\frac{1}{c}\right)} \quad (3.1)$$

In the second method, a backbone of diamonds of side l and angle θ are drawn and are then thickened. Thus l is measured from the center of the walls and e_h and e_v are different from each other and depend on θ .

In the following, l will be mentioned for either methods. In reality the computation will be slightly different in the different cases but will not be mentioned in the following.

These printed shapes are then activated by wires (section 3.3) or by the vacuum (section 3.5) to close the cells. In order to let the wires go through the sample as well as the air when the vacuum pump is switched on, a small hole is left at the center of the walls during the printing of the samples. The holes are designed to be small (radius $r = 0.7\text{mm}$) and at the intersection of the beams in the center of the walls, to minimize the influence on the deformations of the samples toward their final shapes (figure 3.3 right).

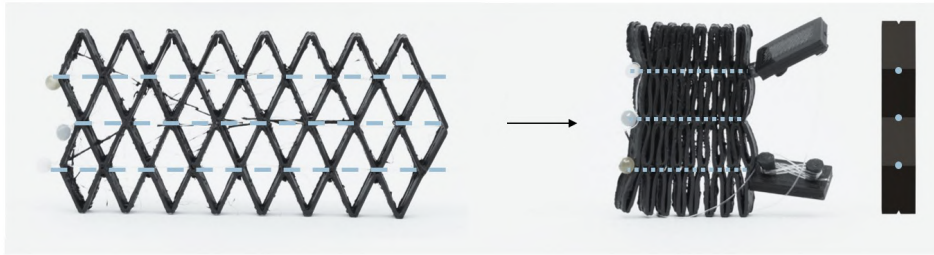


Figure 3.3 Closing of the diamond cells with through a series of wires under tension. Left: rest state. Right: side and front view of the compressed state. The compression is very large.

When cells are activated by wires, the wires are usually pulled taut by hand. They are then blocked thanks to small cleats (wires are coiled around cleats many times and remain in place due to friction). We usually use a wire of high performance nylon with a diameter of 0.35mm that can resist to 13kg (manufacturer data). Usually a different wire is used for each contraction line in order to avoid multiple u-turns in the path of the wire. These turns in the wire path would result in increased friction and make the actuation hardly possible. Nylon and TPU are two materials that are known to cause friction when put into contact due to polar interactions. Nylon is used for its good mechanical properties and for practical purposes because its rigidity helps inserting the wires through the holes. However, using a different material could help reducing friction and enable an easier activation but we have not investigated other materials.

3.2.2 Selecting the final angle: blocker mechanism

Programming 3D shapes requires non uniform in-plane deformations. We can impose different directions of deformation or impose inhomogeneous deformations. In the first case, the orientation of the diamond has to be precisely determined in the other case the amount of closing must be tuned locally. However, simple diamonds usually display only two states: opened (starting state) and closed (final state). In order to get different final strains for the cells, two solutions exist: changing the initial angle of the cells or controlling the closing of cells in their final state. In the second option, if the cells are not completely closed the mechanical performances are less interesting. The challenge is thus to obtain cells with a chosen maximal strain when closed in the final state. To achieve this goal, triangular blockers are implemented to the inner walls of the cells (figure 3.4). As the cells are squeezed, these blockers interlock and set the maximal amount of closing for each cell and thus their maximal and final strain.

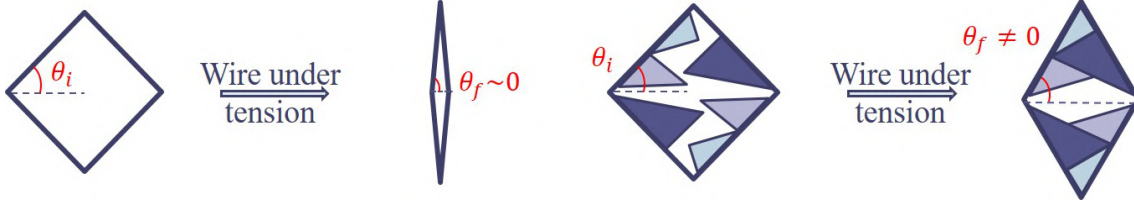


Figure 3.4 Implementation of blockers to control the maximal strain of each cell.

The actuation of such designs can also be reminiscent of the jamming effect. Blocks that are initially loose provide stiffer structures when jammed [102]. In our case, as the triangles get into contact, the diamonds behave as if they were almost a block of bulk material. Moreover, using three triangles instead of two may improve the rigidity of the sample by preventing shear of the diamond thanks to the locking effect. Samples are printed with basic printers so the surfaces are not totally smooth. Having three triangles guides the deformation of the cells and increases the surface of contact, reducing the impact of a bad printing compared to the case where only two triangles meet.

There are different ways of drawing three triangles inside a larger one which can interlock (figure 3.5). For simplicity, we assume that when a diamond closes, there is a simple rotation of the walls around the upper joint. A length e_{joint} is left around the joint to maintain some freedom in the rotation. Two angles are given as an input, the initial angle θ_i and the final one θ_f . Both angles determine the initial shape and the final local strain. The algorithm that determines the shape of these triangles and their truncation is detailed in Appendix A. Moreover, the angle α_1 is set at its maximum value θ_i , which leaves an empty space inside the diamond after closing. Then, only two parameters have to be chosen to determine precisely the size and location of the triangles. The parameters taken for construction are the angle γ_3 and the length l_3 (figure 3.5). In most of the cases, γ_3 is set to $\alpha_1 - 0.19$ and $l_3 = \frac{3}{4}l$. These parameters are chosen arbitrarily to have triangles of similar sizes. For convenience, the initial and final angles are defined by the aspect ratios: $C_i = \tan \theta_i$ and $C_f = \tan \theta_f$.

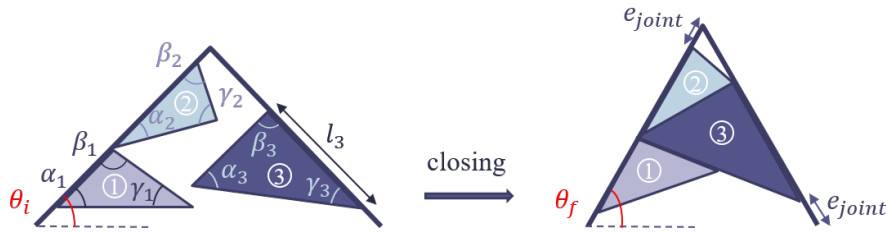


Figure 3.5 Sketch of the closing of half a diamond with initial and final angles θ_i and θ_f . α_1 is set to θ_i , its maximal value. In addition to the three parameters just cited, it only takes two more parameters to completely define the system. The parameters chosen are l_3 and γ_3 .

The samples used for the experiments are homogeneous systems with aligned diamonds that undergo purely in-plane deformation. The size of the blockers is changed from a sample to another keeping some parameters constant: the initial aspect ratio C_i , the side length l , the thickness e and height h of the walls.

Changing shape by closing cellular structures

The size of the blockers determines the final aspect ratio $C_f = \frac{a}{b} = \tan \theta_f$ of the diamond and thus the local strain. In figure 3.6, when the final C_f is increased, the final compression is smaller.

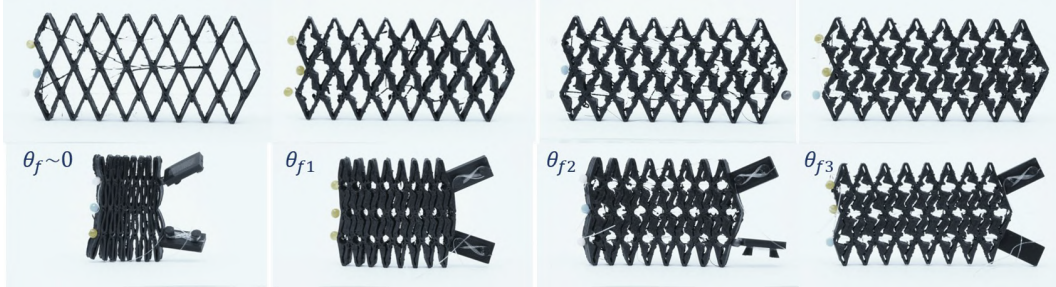


Figure 3.6 Samples with constant parameters $C_i = 2$, $l = 15\text{mm}$, $e = 0.8\text{mm}$ and $h = 8\text{mm}$ but with different size of blockers before (up) and after (bottom) being activated. From left to right: no blockers, $C_f = 4, 6$ and 8 .

In addition to determining the final strain of the cells, blockers bring stiffness to the structures when the samples are activated with wires. It can be observed through tension and compression tests using an Instron machine on samples that are in the closed and free state (figure 3.7). In the free state, we can observe that the sample is blocked in compression (slope break) when the blockers are in contact.

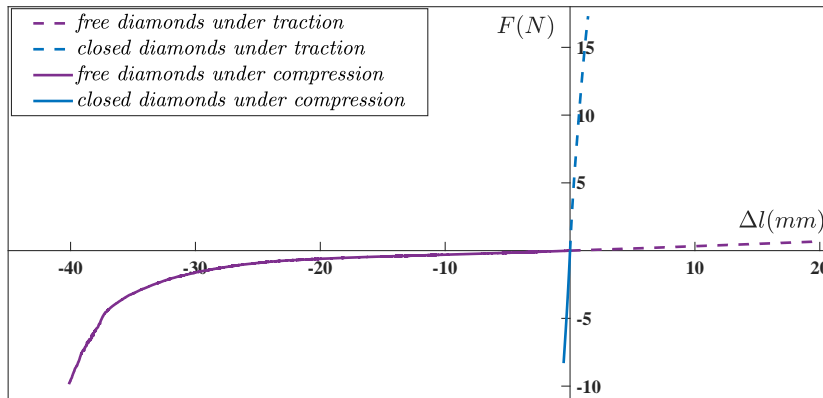


Figure 3.7 Sample containing blockers, tested directly (purple) or after being closed by a pulled internal wire (blue) in traction and compression. $C_i = 2$, $C_f = 4$, $l = 15\text{mm}$, $e = 0.8\text{mm}$

3.3 Programming with blockers

In order to obtain 3D shapes out of a planar network, the strain magnitude and direction have to be determined locally. The presence of blockers of different sizes inside the diamonds allows us to locally tune the strain and can thus be used to program 3D shapes: the larger the blockers, the lower the

compression strain. In this section, we will show how cells with blockers activated by wires can be used to program 3D shapes.

3.3.1 Aligned diamonds with different blockers

First we keep a tiling of aligned diamonds, but change the size of the blockers from one line to another. With two similar designs we can obtain shapes with positive or negative Gaussian curvature (figure 3.8). If the strain is larger on the edges than in the center, when the wires are pulled along the lines a barrel shape appears (figure 3.8 top). Conversely, if the strain is larger in the center than on the edges, a “catenoid-like surface” emerges when activated (figure 3.8 bottom). These two samples are designed to have negative and positive Gaussian curvature but we did not program a specific target geometry.

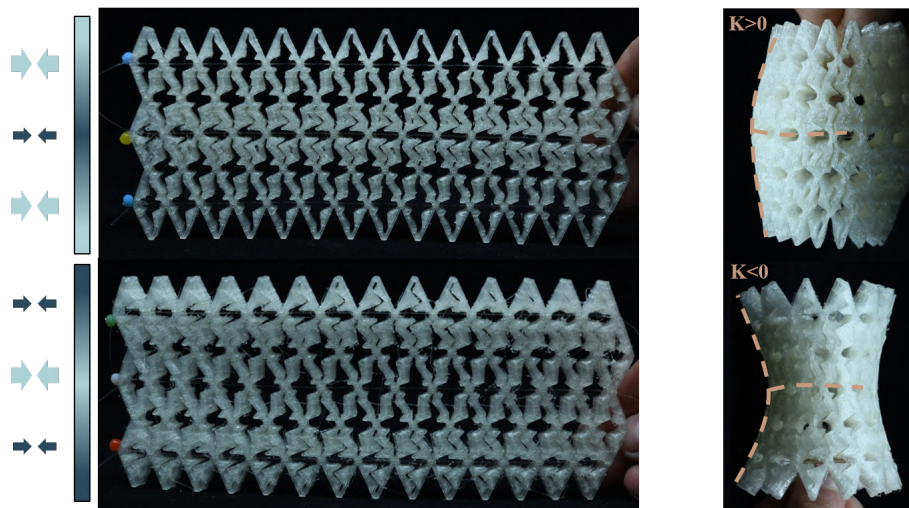


Figure 3.8 Variation of the size of the blockers along the rows. On top, the blockers are smaller on the edge than in the center, leading to a barrel. On the bottom, in contrast, the blockers are smaller in the center than on the edges which leads to a catenoid-like surface with a negative Gaussian curvature.

The two previous designs can be combined in one to obtain a sample with both positive and negative Gaussian curvatures. The top part of the sample is programmed to have a catenoid-like shape (large-small-large blockers) and the bottom part is programmed to have a barrel shape (small-large-small blockers) (figure 3.9 left). When the wires are pulled and the diamonds closed, a vase shape appear (figure 3.9) that exhibits both negative and positive Gaussian curvature.

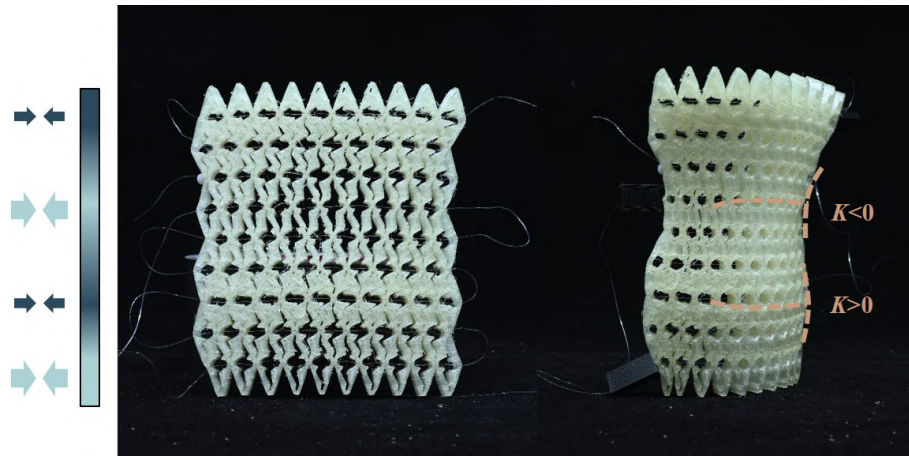


Figure 3.9 Diamond network, varying the size of the blockers from one line to another. It is a combination of the two samples figure 3.8. When the shape is activated, a portion of vase appears with both negative and positive Gaussian curvatures.

3.3.2 Axisymmetric actuation

In the previous section, an initially flat rectangle is transformed either into a barrel or in a catenoid shape by playing with the distribution of the closing angles with the blockers. The same strategy could be generalized to other shapes. However, programming the final shape requires solving an inverse problem: what distribution of final angles should we select to obtain a target shape after actuation? We first tackle this problem in the case of axisymmetric shapes. The designs are similar to the ones used in the second chapter to pave a disk with diamonds: logarithmic spirals. The plane can be tiled in multiple ways, but using logarithmic spirals ensures that the magnitude of the strain will be the same for all the cells. As a consequence if no blockers are put, a cone (figure 3.10) or e-cone should emerge.

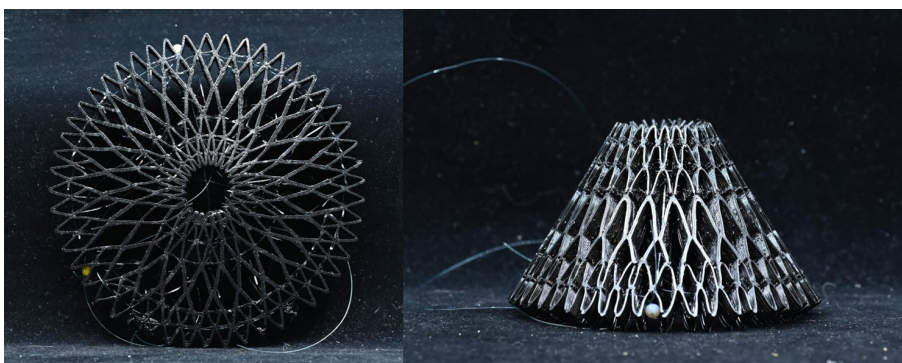


Figure 3.10 Diamonds network made with logarithmic spirals. When orthoradial wires are pulled, a conical shape emerges (right).

We start with the case where cells are programmed to close in the orthoradial direction. As the diamonds pave a disk, they are not exactly diamonds because all sides do not have the same length, the

sides close to the center are shorter than the two others. Each diamond can be divided into two isosceles triangles which share the same base but have different side lengths. Thus, for each diamond, two sets of blockers are calculated, one for each triangle. The size of the blockers is programmed to have the same base length for both half diamonds after being activated by wires.

To activate these shapes, a wire is inserted along the perimeters through the center of the diamonds. When the wire is taut, there is a negative strain along the orthoradial direction, and a corresponding positive one along the radial direction. As the magnitude of the strain is the same everywhere, a cone is obtained. The size of the blockers determines the slope of the cone: the smaller they are, the steeper the cone (figure 3.11).

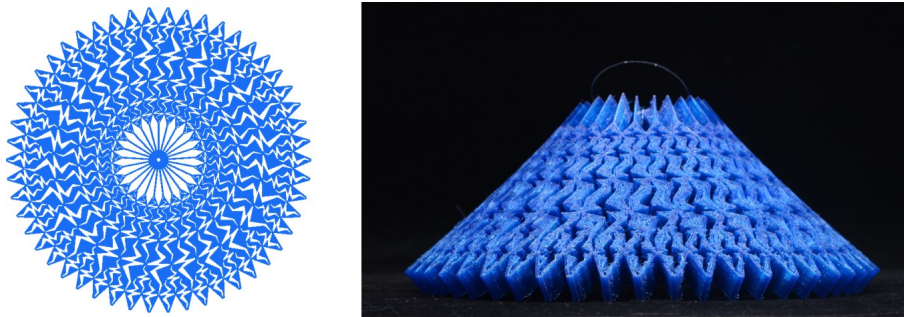


Figure 3.11 Conical shape obtained keeping the size of the blockers constant for all cells.

In the opposite case, cells close radially and are elongated along the perimeters. This configuration is more difficult to design because the two sides of the diamonds that are getting in contact do not have the same length, they are not on the same ring in the spiral construction. The design of the blockers is thus slightly adapted to take into account the movement of the diamonds when they are closed. When looking at the movement of a portion of disc, we see that the edge of the diamonds are following a circular trajectory when the cells are closed. In this configuration, the wires are put radially (figure 3.12), and we obtain an e-cone. Even when manipulating by hands (without wires), the e-cones appears spontaneously.

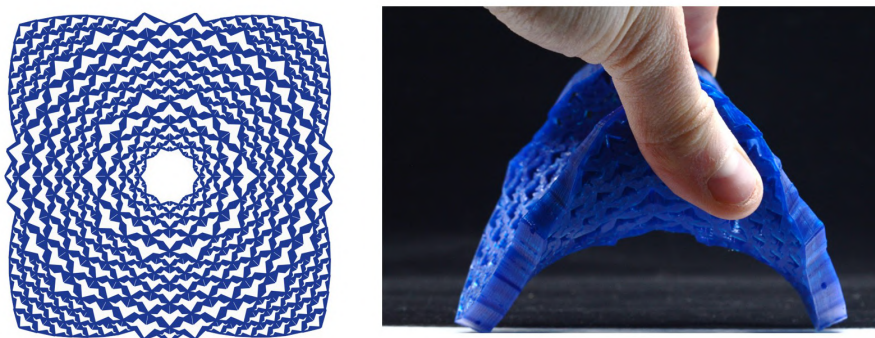


Figure 3.12 E-cone obtained keeping the size of the blockers constant for each cell.

Changing shape by closing cellular structures

In order to solve the inverse problem for more complex axisymmetric shapes than cones and e-cones, we choose to use diamonds network with orthoradial wires, because they are easier to design. In this method, shapes are designed from the profile that generates the shape through rotation along its axis of symmetry. We wrote an algorithm that computes the position of the points along the desired shape in the final state (figure 3.14 red crosses). To each of these points will correspond a given perimeter to match. The algorithm computes the solution step-by-step because of the coupling between strains in the radial and orthoradial directions. The drawing starts from the center of the sample and proceeds ring after ring (we consider as a ring a row of triangle at the same distance from the center. A triangle is defined as half a diamond). The diamond corner that is the closest to the center is assumed fixed, it is put on the profile at a given distance r from the center. To this new position corresponds a new radius R_f dictated by the profile, the perimeter of the ring has to be reduced from $2\pi r$ to $2\pi R_f$, the blockers are programmed accordingly. This orthoradial contraction induces a radial extension of the ring and thus gives the position of the next ring on the profile. The same process is then repeated for this new ring. By iteration, the whole profile is mapped. More details are presented in Appendix A.

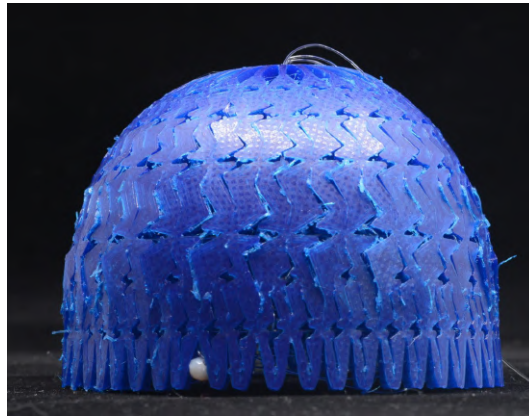


Figure 3.13 Non-uniform strain magnitude along the radius leads to domes.

With this design the closing is activated by wires, allowing us to control which diagonal will be closed (not necessarily the small one). Using diamonds with low θ angle ($\theta < \frac{\pi}{4}$) is interesting because the contraction strain obtained can be very large and a wider range of shapes can be obtained. In addition to cones and domes figure 3.13, we can obtain shapes that close onto themselves, such as spheres figure 3.14.

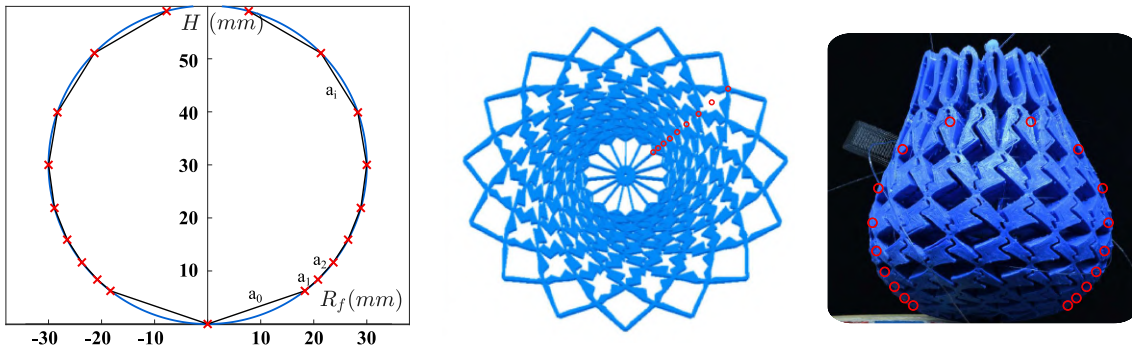


Figure 3.14 Sphere obtained from a profile following half a circle. On the left, the profile is in blue, the black segments correspond to the length of each closed ring and the red crosses correspond to the position of the bottom of the ring. In the center, the programmed network and on the right the samples closed by orthoradial wires. The red points correspond to the prediction of the profile.

In the case of figure 3.14 the profile is half a circle. On the left, the target profile is plotted in blue. The red crosses are the points at the base of each diamonds ring. The black segments correspond to the closed diamonds. On the center of figure 3.14 we show the sample in the flat open state. The diamonds that are far from the center have very small blockers whereas the ones in the center have bigger ones: the strain is much larger on the periphery than close to the center in order to close the sample onto itself. In the open state, a wire is laid trough the middle of the diamonds along the orthoradial direction, and when it is pulled an almost closed axisymmetric shape is obtained (figure 3.14 right). A pretty good agreement with the programmed profile (red circles) is obtained. The last ring should not be taken into account as it corresponds to an extra half of diamond added for practical purposes.

The same work is done for a profile of half an ellipse (figure 3.15). The blue network in the center seems very similar to the one for the sphere. With bare eyes it is difficult to distinguish the two, but in the activated state they are clearly different (one is a sphere and the other one an ellipsoid).

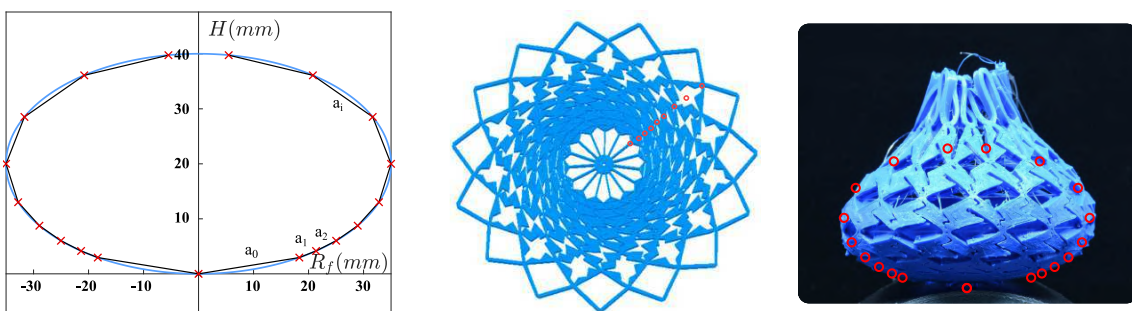


Figure 3.15 Ellipsoid obtained from a profile with half an ellipse. On the left, the profile is in blue, the black segments correspond to the length of each closed ring and the red crosses correspond to the position of the bottom of the ring. In the center, the programmed network and on the right the samples closed by orthoradial wires. The red points correspond to the prediction of the profile.

Changing shape by closing cellular structures

In both previous cases, the cellular structures undergo a transformation from zero Gaussian curvature to positive Gaussian curvature. Using diamonds with $\theta < \frac{\pi}{4}$ ($C < 1$), we can also design samples that go from zero Gaussian curvature to a distribution of positive and negative Gaussian curvatures, as in the case of the vase in figure 3.16. At the bottom of the vase, the Gaussian curvature is positive but it is negative at the neck of the vase.

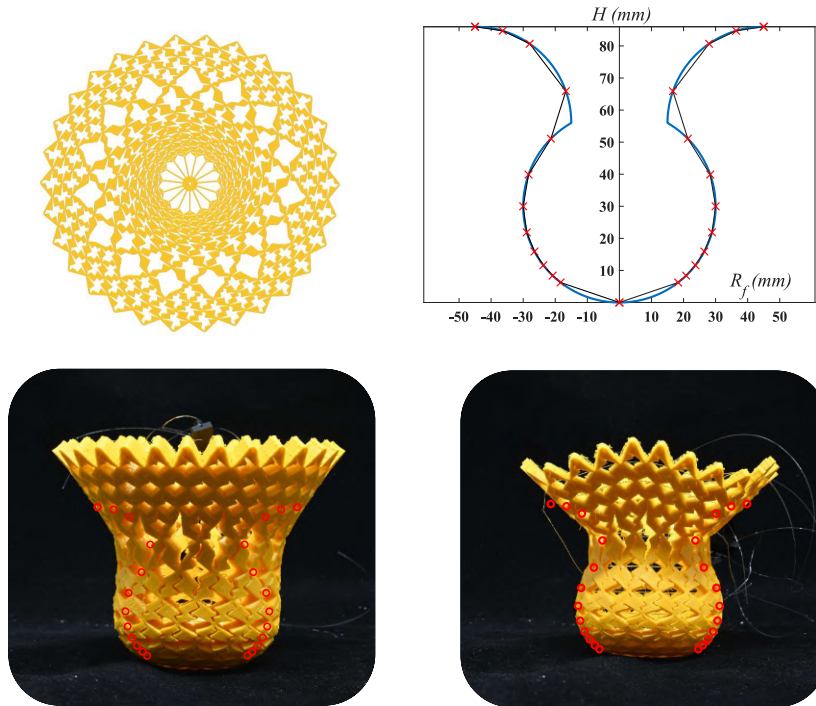


Figure 3.16 Vase obtained from a profile with vase. On the top right, the profile is in blue, the black segments correspond to the length of each closed ring and the red crosses correspond to the position of the bottom of the ring. On the top left, the programmed network. On the bottom activated samples with different thicknesses, $h = 8\text{mm}$ on the left and $h = 4\text{mm}$ on the right.

With this method, we demonstrated that different surfaces of revolution can be obtained, even shapes that can close onto themselves (such as spheres) or ones that have both positive and negative Gaussian curvature (such as the vase). The method only requires a profile that will be then translated into a 3D object.

There are however some limits to this technique. There is a minimal initial angle θ or C under which the blockers are too small to be activated. When the diamonds are very elongated in the closing direction, the initial area inside the diamond is very small and thus there is no room to insert blockers. In order not to have any issue, the minimal initial $C = \tan \theta$ is set to 0.7 and thus fixes the maximal contractions that can be obtained.

The other limit to this method is that the algorithm is only geometric and does not take into account the mechanical properties of the samples, especially the bending properties. That is why the solution

does not perfectly match the 3D object in figures 3.14, 3.15, 3.16 and why the thickness of the sample plays a role. When the sample is very thin, the bending is very easy, however some diamonds can bend out of plane due to the tension of the wire (figure 3.17). The final shape slightly deviate from the target: thicker samples comply more closely to the closing law for each individual cell. However, they are more difficult to bend out of the initial plane of the samples figures 3.18, 3.16 (bottom). An optimal thickness has to be used. To limit the bending in the wrong direction as in figure 3.17, the cells have to remain small, the size of the cells must be linked to the thickness of the sample. The bigger are the cells the thicker the samples have to be.



Figure 3.17 Vase shape from a sample with thickness 3mm. The external diamonds bend out of plane.

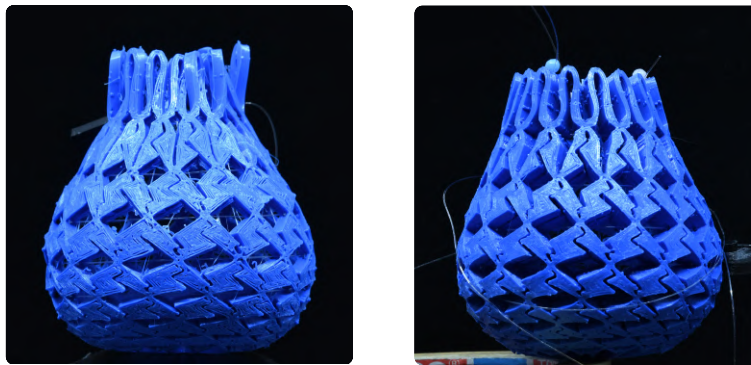


Figure 3.18 Spherical shapes from a sample of thickness 3mm on the left and 8mm on the right. The shapes are slightly different, on the left the overall structure bend more easily but on the right the individual cells close more in plane.

In this section, samples were activated with wires but some can also be activated by hand. Indeed, when an elastic plate is bent, at small deformation, a negative Gaussian curvature is obtained because of the Poisson coupling. Samples figure 3.12 can be activated by hand just with a simple torque applied by hand because they are programmed to reach negative Gaussian curvature when the diamonds deform along their natural mode.

3.3.3 General inverse problem

In this section we will focus on a more general inverse problem that is not restricted to axisymmetrical shapes. A technique used to map a 3D surface with diamond makes use of Chebyshev nets. Such nets are diamond meshes that can cover arbitrarily curved surfaces keeping the side length of the diamonds constant. They correspond to a deformation of a planar grid of identical diamonds: the lengths are conserved but the angles are not [103].

This idea of having a net that can change shape by adapting locally the angle of the diamonds can be applied in our case. A 3D surface can be mapped with a Chebyshev net, then be flattened to be printed to recover the 3D shape once activated. A solution to map smooth surfaces with a Chebyshev net is the “compass method” [104, 105] (figure 3.19). Two arbitrary geodesics are drawn on the surface (curves that are “straight lines” along the surface) that are intersecting at an arbitrary point. These two curves are divided in segments of equal length. Starting from the intersecting point, diamonds are drawn using a “compass”, all the diamond sides have the same length along the surface. The overall network is then drawn step-by-step.

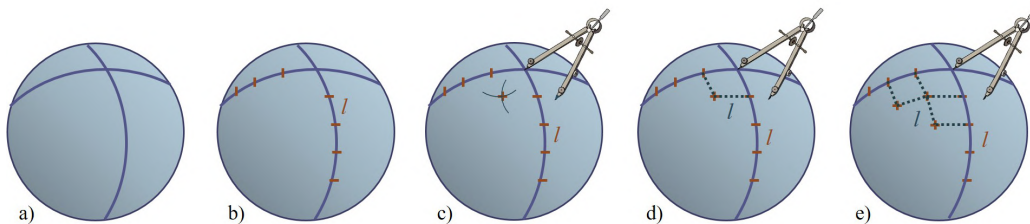


Figure 3.19 Successive steps of the compass method. a) Two geodesics (straight lines along the surface) are drawn; b) They are divided in equal length l ; c),d),e) Thank to a compass, diamonds of identical length are drawn on the surface.

Although the two geodesics can be chosen arbitrarily, it not always possible to map any shape without generating singularities. Thus the initial conditions have to be chosen carefully to map the desired shape entirely. Mapping 3D surfaces with Chebyshev net is mostly used to design gridshells [99, 105, 106].

The work of this section has been done in collaboration with Hillel Aharoni from the Weizmann Institute. He programmed 3D diamond meshes to map a 3D surface with the compass method. The algorithm takes a 3D surface as an input. Using well chosen initial conditions, it maps the 3D surface with diamonds of given length l . In order to ensure smooth deformations, the size of the diamonds is chosen smaller than the inverse of the local curvature. Once the 3D surface is mapped, the angles of all diamonds are measured and compiled. The output of the algorithm is a map of the cells with their angle on the deployed target shape (figures 3.20 and 3.21 top right).

We choose to start from an initially homogeneous network of identical diamonds. If their target angle is encoded in them, the 3D shape should appear when the structure is activated. We use the map to

set the position of the diamonds in the flat state and the blocker size of each diamonds is programmed to fit the final angle measured on the 3D shape in their activated state.

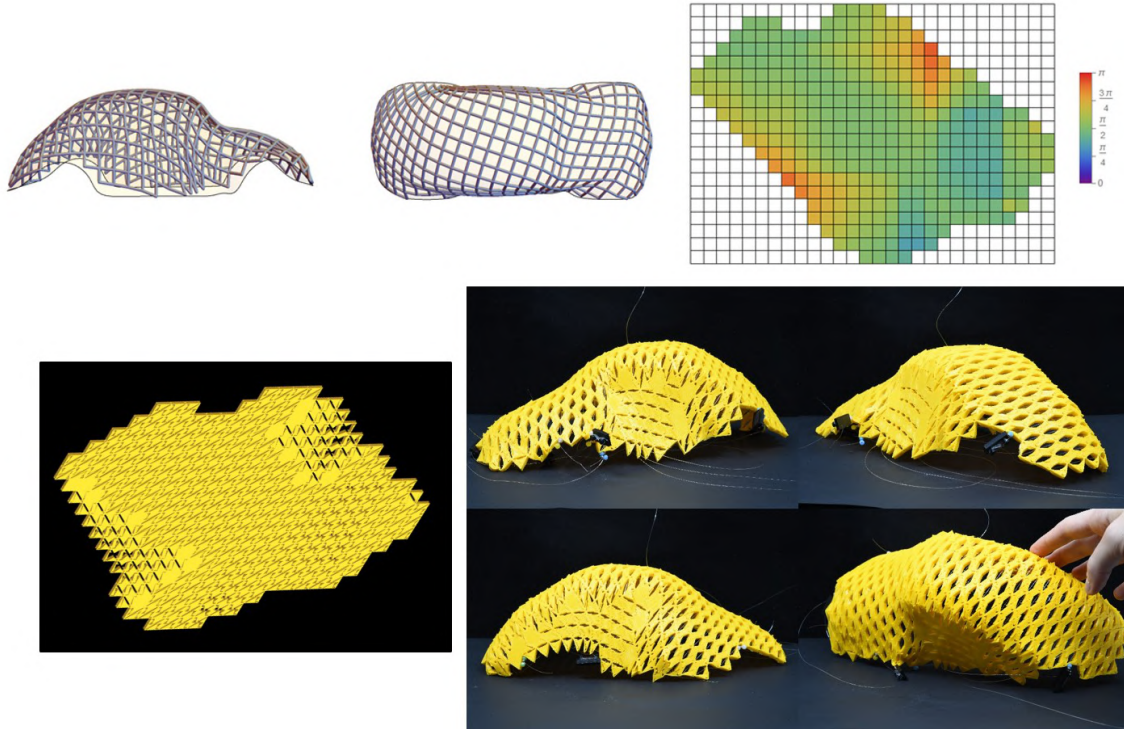


Figure 3.20 Upper left: car mapped with a Chebyshev net. Upper right: map of the angles, each color corresponds to a different final angle. Bottom: Network in the flat state (left) and activated by wires (right): a car emerges.

The final angles that have to be programmed are determined by the mapping of the 3D shape but the starting angle of the flat structure can be chosen arbitrarily. The final angle θ_f measured on the 3D surfaces varies from 0 to $\frac{\pi}{2}$. If the flat rest state grid is homogeneous, diamonds close in different directions of space depending on the local final angle of each cell. A simple solution is to take the initial angle at $\frac{\pi}{4}$ (square cells). However closing the cells in the two directions of space would require to have wires in the two directions and thus complexifies the task of inserting wires through the sample. In addition, it is better to have close initial and final angle as it allows to have bigger blockers and thus a better locking. For these two reasons, the initial angle is chosen such that the majority of the cells close in the same direction and have initial and final angles that are not too different.

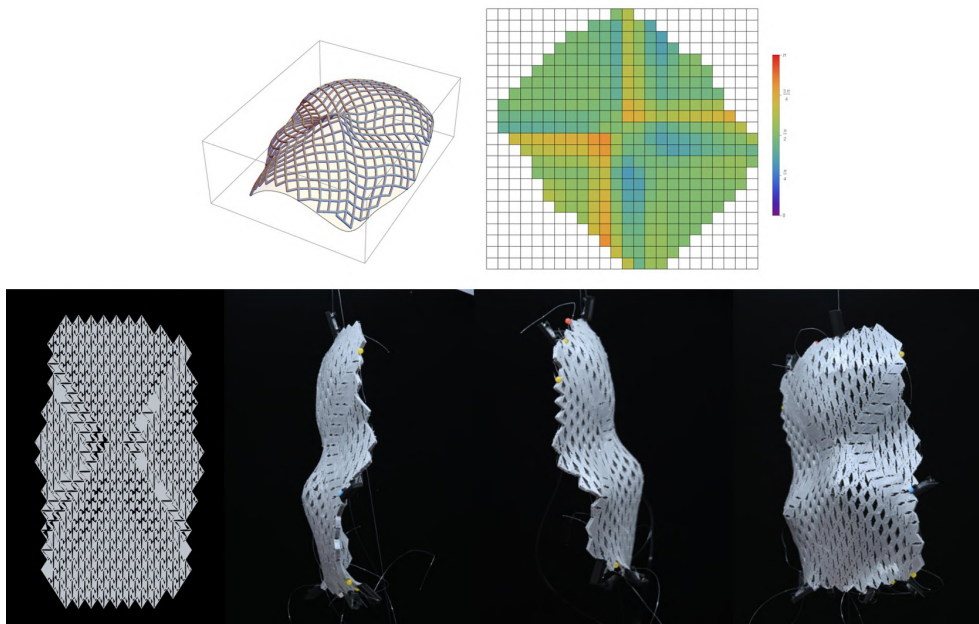


Figure 3.21 Upper left: face mapped with a Chebyshev net. Upper right: map of the target angles, each color corresponds to a different final angle. Bottom: Network in the flat state (left) and activated by wires (right): a face emerges.

Thus instead of calculating the distribution of strain to obtain 3D shapes out of planar structures, each diamond cell is programmed to fit the shape it should have on a 3D structure. The limit of this method is the existence of a solution that actually maps the target 3D structure with a Chebyshev net. A suitable initial conditions must be found in order for the solution to converge. This first step is not achievable to map any surface without forcing singularities.

3.3.4 Programming the curvature

The blockers used are straight and homogeneous through the thickness of our samples. When the sample bends, the outer face gets longer than the internal one, and the closing is thus not perfect along the thickness. The size of the blockers encodes the metric change but not the curvature. Any deployed shape can for instance be “popped out” inside out without changing the metric. The prediction of the 3D deformations is done in the limit of thin plates with vanishing thickness, which is not the case of our samples. In order to program the curvature, blockers must not be homogeneous across the thickness of the sample. Blockers must then have edges that are not vertical, or equivalently have different sizes on both faces of the samples. Changing the size of the blockers along the thickness of the sample allows to select a specific isometry. We can draw blockers of different sizes on the two faces of the diamonds according to the local curvature along the bending diagonal.

As a first experiment, we print a network of identical diamond cells which should keep a zero Gaussian curvature upon activation. However, the size of the blockers is varied linearly across the thickness of the structure, enabling to define the dimensional mismatch between both sides of the

deployed sample. Doing so, a cylindrical shape is selected among a family of developable surfaces (figure 3.22 left).

In a second attempt, this method is applied to samples with changing Gaussian curvature upon activation. Knowing the final shape and the thickness of the samples, we can determine the difference in curvature for both sides of the sample and program the blockers accordingly. In figure 3.22 right, a catenoid-like sample is programmed with both metric and curvature. The sample seems to be “full” compared to the sample one figure 3.8. This technique has a limit: it only allows to match the curvature along the diagonal that closes, the object in the final state is thus not always totally “full”.



Figure 3.22 Left: Cylinder obtained by varying the size of the blockers across the thickness of the sample. Right: Catenoid-like surface with curvature encoded in the blockers, the material appears as “full”.

3.4 Mechanical properties of cellular plates

In the previous section, we showed how to program 3D shapes with cellular structures. This programming only relies on geometry. The plates are assumed infinitely thin but it is not the case in reality. In this section we propose to study the mechanical properties of such systems to improve their design in order to program shapes more precisely.

3.4.1 Mechanical properties under traction/compression

In order to understand the mechanical behavior of complex diamonds networks, we first study the linear networks described in part 3.2. The samples are tested under traction and compression with an Instron test machine. They are held by jaws at both ends, along 3 points of the network, on a line drawn in orange on figure 3.2. One of the jaw is fixed to the ground while the other is connected to a 100 N force sensor. Displacement is imposed, and the force is measured. If deformations are relatively small,

Changing shape by closing cellular structures

responses in compression and tension exhibit the same stiffness. We observe a linear response at small displacements, figure 3.23.

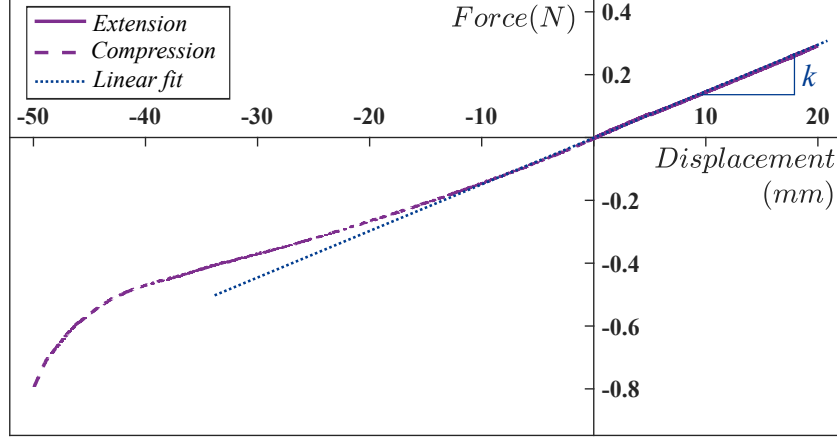


Figure 3.23 Force-displacement curve of a diamond network in traction and compression with: $l = 15\text{mm}$, $e = 0.6\text{mm}$, $h = 10\text{mm}$, $C = 3$, $N_w = 3$ and $N_L = 8$ (number of diamonds in the width and length) printed in TPU.

However for very large compressions ($\delta \sim L$), we measure a sudden increase in the force. This is the transition towards the state where the network is totally compressed: diamonds are closed and all beams are in contact. When this state is eventually reached, we expect the measured force to correspond to the compression of the bulk material. In addition to the shape change, the closing of the cells increases rigidity.

In this part we focus on the mechanics of small deformations in the linear regime. The deformation upon traction and compression of the samples is measured for different parameters l , e , h and θ . If the network is considered as a sample of homogeneous material, an effective Young modulus can be extracted from the slope k of the curves of figure 3.23.

$$F = k\Delta L = whE^* \frac{\Delta L}{L} \quad (3.2)$$

$$E^* = \frac{L}{wh}k \quad (3.3)$$

where F is the measured force, E^* the effective young modulus and k the slope of the force-displacement curve. The coefficient k considered is the average of k_{ext} and k_{comp} (values in traction and compression) for different trials. The effective modulus E^* can thus be experimentally measured.

This effective modulus results from the bending response of the walls that constitute each diamond cell. The stiffness of a honey-comb cellular structure has already been derived by Gibson and Ashby [107] in their book *Cellular solids*.

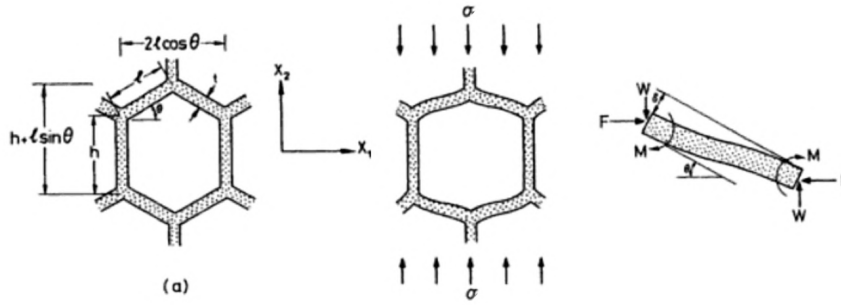


Figure 3.24 Compression of honeycomb structure. The mechanical response of the beams composing the cell results in an effective Young modulus for the homogeneous material. Picture from Gibson and Ashby book [107].

In this derivation, they assume that the clamping angle θ of honeycomb is conserved under loading, but when the cells deforms, the upper and lower sides of the cells of length l bend. Thus the loading is converted in bending of the beams. In the case of the diamonds, the vertical sides of the honeycomb are missing and the walls that bend form the diamond. This computation can be then extrapolated to diamonds that are similar to honeycomb with $h = 0$ (figure 3.24).

Following the same framework one can thus derive the effective modulus for a diamond network. For the derivation a loading F along X_1 is considered.

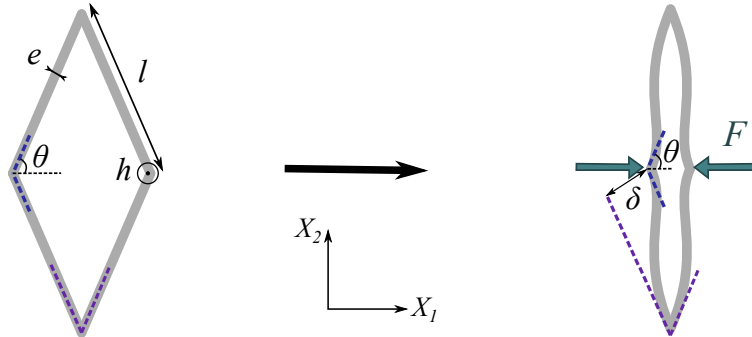


Figure 3.25 Compression of an elementary diamond-shaped cell. The sides bend under the loading F .

We consider half of the load $\frac{F}{2}$ that applies in an arm of length l on an elementary beam of the diamond of length l , thickness e and height h (figure 3.25). The resulting torque M (3.4) with respect to the lower corner of the cell reads:

$$M \sim Fl \sin \theta \tag{3.4}$$

We give here a simple law argument. For elastic beams the moment is given by the product of the bending stiffness by the induced curvature κ :

$$M = EI\kappa \sim EIw''(x) \tag{3.5}$$

Changing shape by closing cellular structures

with $w(x)$ the deflection of the beam at x .

In term of scaling $w''(x) \sim \frac{\delta}{l^2}$, $Fl \sin \theta \sim EI \frac{\delta}{l^2}$, which leads to the scaling law:

$$\delta \sim \frac{Fl^3 \sin \theta}{EI} \quad (3.6)$$

If the same calculation is conducted with the pre-factors, the deflection δ becomes:

$$\delta = \frac{Fl^3 \sin \theta}{24EI} \quad (3.7)$$

with I the second moment of area of a regular beam $I = \frac{he^3}{12}$.

Considering the deflection along X_1 , $\delta \sin \theta$, the corresponding effective strain ε can be computed.

$$\varepsilon = \frac{\delta \sin \theta}{l \cos \theta} = \frac{Fl^2 \sin^2 \theta}{24EI \cos \theta} \quad (3.8)$$

By defining $\sigma = \frac{F}{2hl \sin \theta}$ we obtain:

$$\varepsilon = \frac{2hl^3 \sin \theta^3}{24EI \cos \theta} \sigma = \frac{\sin \theta^3}{E \cos \theta} \left(\frac{l}{e}\right)^3 \sigma \quad (3.9)$$

The effective Young modulus E^* can thus be deduced as $\sigma = \varepsilon E^*$ for the sample.

$$E^* = \left(\frac{e}{l}\right)^3 \frac{\cos \theta}{\sin^3 \theta} E \quad (3.10)$$

The relation between E and E^* can be tested for different samples. The l used for the calculation is not easy to define if e is not very small. In our case we will take l as the inside edge length of the diamonds, which corresponds to the portions of each beam that is really free.

The measured effective modulus, E_{mes}^* is plotted as a function of $\left(\frac{e}{l}\right)^3 \frac{\cos \theta}{\sin^3 \theta}$ (figure 3.26). The relation between the two is linear and the prefactor is of the same order of magnitude as the modulus of the filament. On the plot, the measured modulus is $E_{mes} \sim 50$ MPa, in contrast with the 26 MPa measured on test samples of TPU. On the data sheet of Filaflex, the tensile modulus is 49 MPa. The tests on test samples were done with samples printed with oblique lines, which may explain the difference in the modulus.

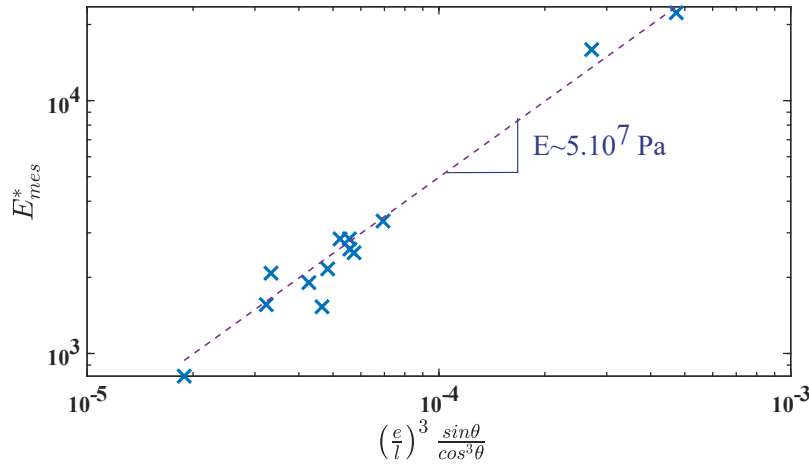


Figure 3.26 Effective modulus as a function of $\left(\frac{e}{l}\right)^3 \frac{\cos\theta}{\sin^3\theta}$, scaling obtained if we consider the bending of the beam as the mechanism involved in the closing of the diamonds (i.e. if the angles at the corner remain constant). During the experiments, e , l , θ and h .

The data on figure 3.26 validates the hypothesis on the bending of beams and the fact that the angle of the diamonds remains unchanged upon deformation. The sides of the diamonds appear to behave as clamped singular beams rather than long beams with joints, as seen in gridshells. The joints between diamonds do not seem to play a role at the first order.

The same measurements can be done on samples with blockers. Networks of aligned diamonds with blockers are put under traction and compression. Samples are tested with no blockers and with blockers corresponding to a final ratio $C_f = \frac{a_f}{b_f}$ of 8, 6 or 4 with a starting ratio $C_i = 2$ (figure 3.27). During the compression test, we can observe that there is a large break in the slope, the material becomes much stiffer. This slope break appears when the samples are totally closed and the blockers are in contact. At this point, the sample behaves almost like a bulk material. When the blockers are larger (C_f small), the slope break appears for smaller displacements (figure 3.27). The displacement measured at this slope break corresponds to the final strain encoded in the size of the blockers.

In the pre-closed state, when the cells are closed and blocked with a wire, we observe a similar response but the sample behaves directly as a bulk material as the cells are already closed and the blockers are in contact (figure 3.7). Indeed the slopes observed for large negative deformation for the free sample are similar to the slope observed for small negative deformations in the case of the pre-closed network.

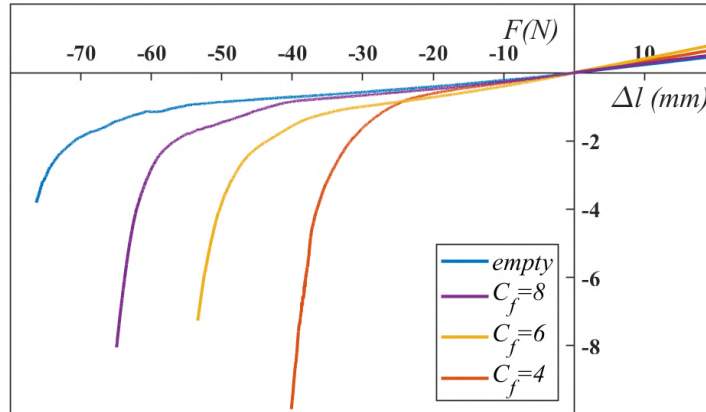


Figure 3.27 Open sample under traction and compression with $C_i = 2$, $C_f = 4 - 8$, $l = 15\text{mm}$, $e = 0.8\text{mm}$.

In the case of the samples with blockers, the rigidity for small displacements in the open state should not be dictated by the size of the blockers. As seen in the previous part, under loading, walls of each cell bend and the relevant parameter becomes the thickness of the walls e . In the case of the blockers, the average thickness of the diamonds increases when the final ratio C_f decreases, the rigidity should then increase when C_f decreases. This trend is true for samples without blockers to $C_f = 6$ but an inversion can be observed between $C_f = 4$ and $C_f = 6$ (figure 3.28). In all the previous theory we supposed that the cells were closing due to the bending of the wall, however, if the walls get too thick, the junctions of the diamonds may play a role in the opening/closing of the cells and may influence the rigidity of such samples. This might explain these observations.

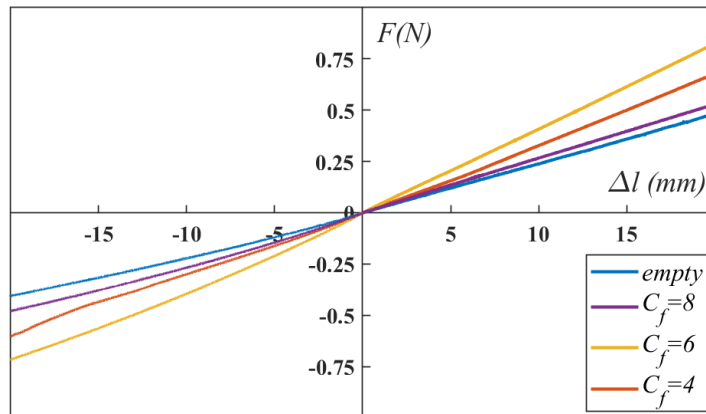


Figure 3.28 Zoom of figure 3.27. Open sample (without wires) under traction and compression with $C_i = 2$, $C_f = 4 - 8$, $l = 15\text{mm}$, $e = 0.8\text{mm}$.

3.4.2 Mechanical properties: bending of cellular networks

After characterizing the diamonds networks under tension/compression, we also characterize their bending stiffness. It might be useful since the structures will eventually be curved into 3D target shapes.

The samples used here are the same as in the previous part 3.4.1. A three point bending test is performed (see figure 3.29). The distance L_{bend} between the two bottom points can be modified. For each sample, the displacement is imposed at the center of the sample and the force F is recorded with a 100 N sensor. For each sample, the measurement is performed for different L_{bend} . The length L_{bend} is chosen not to be too small compared to h ($L_{bend} \gg h$), but smaller than the length beyond which the sample would bent significantly under its own weight, so that gravity can be neglected.

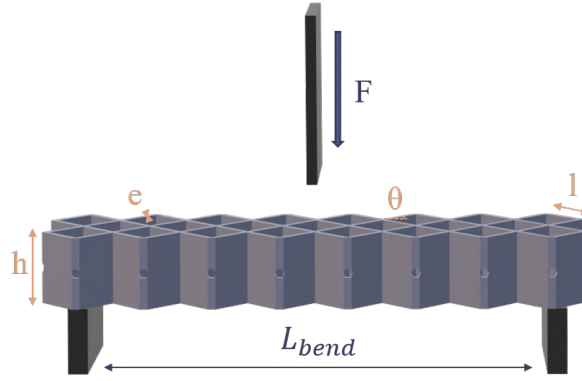


Figure 3.29 Three points bending test of a diamond network.

As in the previous section, the parameters that are modified are θ , l , e and h . In a similar way, we want to determine the relation between the effective bending modulus of the sample B^* and the geometric parameters of the sample. We interpret the 3 points bending test as if the the network was a regular beam with an effective bending modulus B^* . In scaling approach for the three point bending test, the applied moment is given by:

$$M \sim FL_{bend} \sim B^* w \kappa \quad (3.11)$$

with $\kappa \sim \frac{\delta}{L_{bend}^2}$ the curvature.

$$FL_{bend} \sim B^* w \frac{\delta}{L_{bend}^2} \quad (3.12)$$

which leads to:

$$F \sim B^* w \frac{\delta}{L_{bend}^3} \quad (3.13)$$

where δ is the imposed indentation, and w is the width of the sample.

Changing shape by closing cellular structures

We have now access to an experimental measurement of B^* and we can try to find its dependency with the geometrical parameters of the structure.

As a first approximation, the network could be considered as a beam with a reduced density \mathcal{D}_{beam} . In scaling law, $\mathcal{D}_{beam} \sim \frac{e}{l}$ (portion of material per cell). If the network is considered as a simple beam, the effective bending modulus should thus be written as:

$$B^* \sim \mathcal{D}_{bend} h^3 E \sim \frac{eh^3}{l} E \quad (3.14)$$

If this hypothesis were correct B^* should scale as e , h^3 and l^{-1} . However experiments reveal a different trend as shown in figure 3.30. According to the measurements, B^* displays a dependency in e^3 . This trend shows that the network cannot be described as large beam made of less dense material, but as a collection of individual beams of length l . Indeed the presence of a cubic dependency in e is a clue for a bending deformation of a beam of width e , so a deformation at the scale of the diamond cell walls.

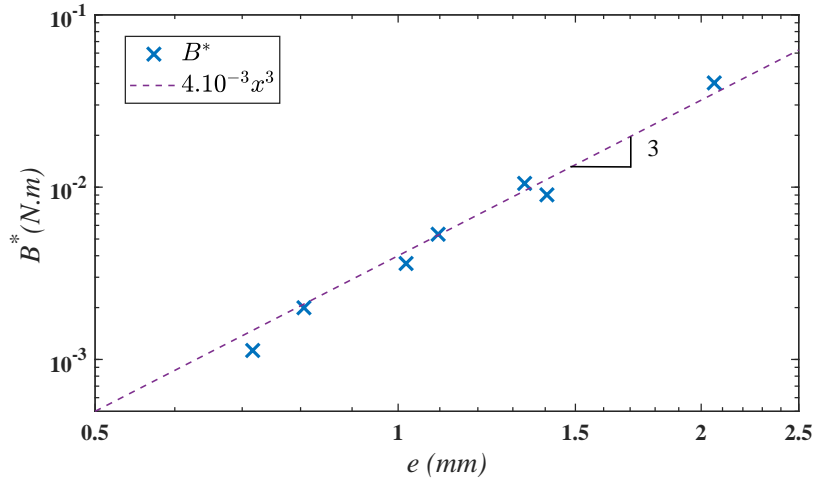


Figure 3.30 B^* measured as a function of the thickness of the walls e , a cubic dependency is observed.

Considering the sample bent globally by a radius R , the bending energy can be written dimensionally as:

$$\mathcal{E}_{tot} \sim \frac{B^* w L_{bend}}{R^2} \quad (3.15)$$

with B^* the effective bending modulus.

We now try to determine what is hidden in the scaling of B^* by estimating directly the elastic energy in the cells. The samples can be considered as a grid of crossing ribbons. Elastic energy of ribbons can be difficult to estimate [108]. However we use a simplified estimate.

Taking a closer look at the bent sample figure 3.31, unit diamond cells appear deformed. In order to obtain a global bending of the sample across its thickness h , one solution would be to bend each elementary beam across h . However, since $h \gg e$, bending across the thickness of the walls is much more favorable than across h . As a consequence, the walls tend to bend across e or to twist to match the

curvature. Each small beam of length l seems to twist to accommodate the overall bending of the sample. On the upper part of the sample, the cells are compressed to reduce the length, but on the bottom part, they open to increase the length, as imposed by the geometry of the overall bending.

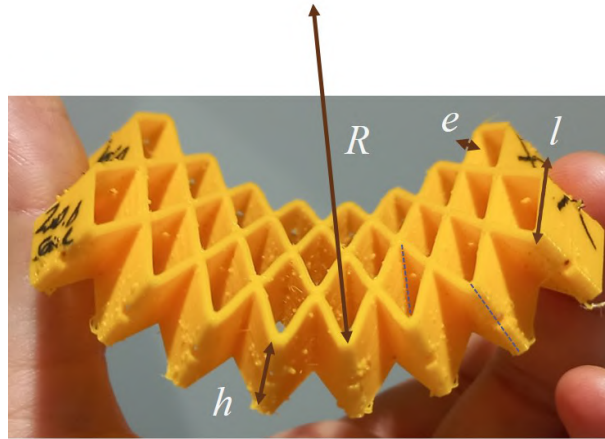


Figure 3.31 Bending of a linear diamonds network with a curvature $\kappa \sim \frac{1}{R}$. The upper part of the cells seems squeezed whereas the bottom part seems more open. The wall of each cells seem to twist (bue dotted lines).

According to the observations made on the picture (figure 3.31), the overall bending energy could be described by the twisting energy of a small beams of length l .

To estimate the twisting energy of a beam, the twisting rate defined as $\tau \sim \frac{\omega}{l}$ has to be estimated where ω is the twisting angle (figure 3.32).

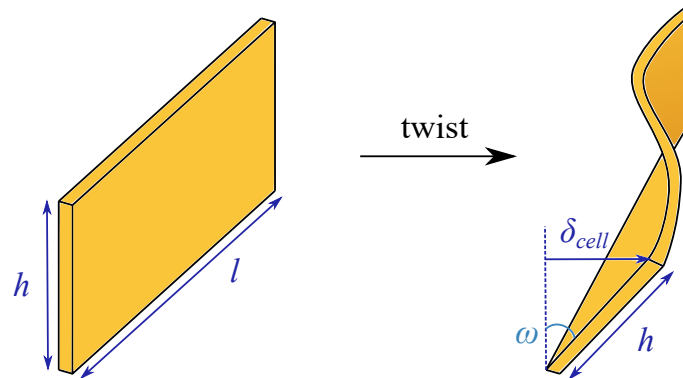


Figure 3.32 Twisting of a beam of length l

In the limit of small displacement $\delta_{cell} \ll h$ (figure 3.32), the twisting angle can be approximated as $\omega \sim \frac{\delta}{h}$, so that:

$$\tau \sim \frac{\delta_{cell}/h}{l} \quad (3.16)$$

Changing shape by closing cellular structures

with δ_{cell} the deflection of each cell so that the upper and bottom part of the sample have different lengths.

If the entire network is seen as a beam bent with a radius of curvature R , one side is stretched and the other is compressed. The strain between the neutral line and the edge is:

$$\epsilon_{tot} \sim \frac{h}{2R} \quad (3.17)$$

This global strain imposes a deflection δ_{cell} such as:

$$\epsilon_{tot} \sim \frac{\delta_{cell} \sin \theta}{l \cos \theta} \quad (3.18)$$

thus,

$$\delta_{cell} \sim \frac{hl}{R \tan \theta} \quad (3.19)$$

We can then deduce the twist rate:

$$\tau \sim \frac{hl}{R \tan \theta} \frac{1}{hl} \sim \frac{1}{R \tan \theta} \quad (3.20)$$

The twisting energy for a ribbon $\delta_{cell} \ll h \ll l$ can be approximated [109]:

$$\mathcal{E}_{twist} \sim \mu \tau^2 l h e^3 \sim \frac{E}{(1+\nu)} \frac{h e^3 l}{R^2 \tan^2 \theta} \quad (3.21)$$

We find here a similar result as in [110], in the case of high beams where the bending in the plane of the ribbons is prohibited. In addition, the derivation made by Lebée *et al.* that we applied to oblique networks with diamonds of angle θ , shows the coupling between the two curvatures along x and y , which are principal direction by symmetry:

$$\kappa_{\perp} = -\frac{1}{R} \tan^2 \theta \quad (3.22)$$

If the sample is bent in one direction, there is a bending coupling in the other direction in order for the ribbons not to bend in their plane. This coupling can be observed on figure 3.31.

By identification we can now determine the expression of the effective bending modulus in the case of pure twisting of the walls (i.e. if $\mathcal{E}_{tot} = \mathcal{E}_{twist}$). The surfacic density of elastic energy is:

$$\frac{\mathcal{E}_{tot}}{l^2 \sin \theta \cos \theta} \sim \frac{B^*}{R^2} \quad (3.23)$$

with $l^2 \sin \theta \cos \theta$ half the area of a diamond, so that the predicted value of B^* reads:

$$B^* \sim \left(\frac{h}{l}\right) e^3 \frac{\cos \theta}{\sin^3 \theta} \frac{E}{(1+\nu)} \quad (3.24)$$

This formula is compatible with a scaling in e^3 measured in figure 3.30. In order to test the different other parameters, the effective bending modulus B^* is experimentally measured for various values of the height h of the samples but keeping the other parameters θ , $l = 15\text{mm}$ and $e = 0.8\text{mm}$ constant (figure 3.33).

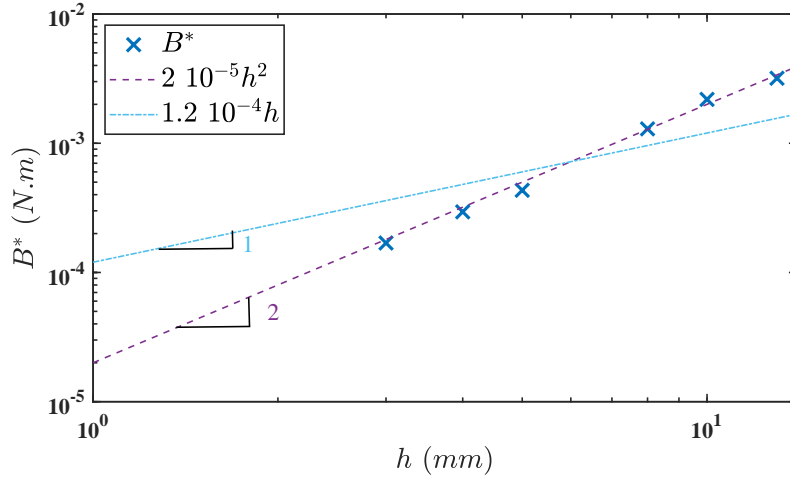


Figure 3.33 Effective bending modulus B^* as a function of h . For these samples, $C = 2$, $l = 15\text{mm}$, $e = 0.8\text{mm}$. The blue line corresponds to a linear dependency and the purple to a square dependency.

Within our experimental range, the effective bending modulus B^* seems to scale with h^2 (purple line figure 3.33). This scaling does not correspond to the one found before considering pure twist in equation 3.24 (h). Instead of having a dependency in $\frac{h}{l}$, the effective bending modulus seems to have a dependency in $(\frac{h}{l})^2$ by dimensional analysis (dependency in e^3 has already been proven experimentally). In order to test this experimental scaling on a wider range of data, the bending modulus B^* is normalized by $e^3 \frac{\cos \theta}{\sin^3 \theta} E_{th}$ considering that the geometrical parameter is true. This normalized effective bending modulus $B_{norm}^* = \frac{B^*}{e^3 \frac{\cos \theta}{\sin^3 \theta} E_{th}}$, with $E_{th} = 5.10^7 \text{Pa}$ the approximate value of the Young modulus, is plotted versus the ratio $\frac{h}{l}$ figure 3.34.

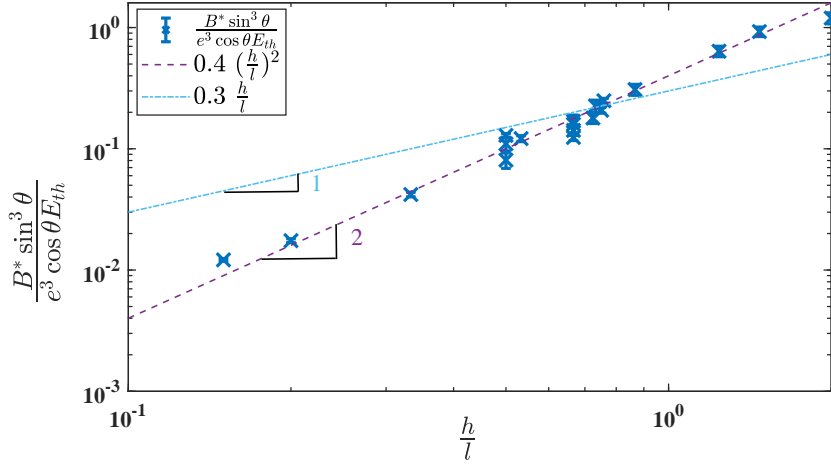


Figure 3.34 Effective bending modulus B^* normalized by $e^3 \frac{\cos \theta}{\sin^3 \theta} E_{th}$ against $\frac{h}{l}$ for all samples varying θ , h , e and l .

The experiments seem in good agreement with a scaling in $(\frac{h}{l})^2$, the experimental points are aligned in figure 3.34 and the prefactor is of the order of 1. Experimentally, the expression of the effective bending seems to be:

$$B_{exp}^* \sim \left(\frac{h}{l}\right)^2 e^3 \frac{\cos \theta}{\sin^3 \theta} E \quad (3.25)$$

It does not corresponds to the expression obtained considering only the twisting energy. This may be explained by different hypothesis. First, if the ribbons twist, they may also bend to help the overall bending. We did not succeed in modeling the bending perpendicularly to the walls, this component may help understanding this scaling. Secondly we may not measure the linear response of the system, the linear regime might only be true for small global deflection that are too small to be measured. Lastly we supposed that there were no bending in the height of the wall but the ribbons might be able to curve in their plane. Their twisting energy might also involve stretching [108].

In conclusion of this mechanical part, the mechanic of the diamond networks is driven by the small beams of length l that compose the network. We have shown that the bending and twisting of these beams that can be described as ribbons, drive the compression, extension and bending of the bigger object in the case of small strains.

3.5 Activation with vacuum

We have activated our networks with wires, but this method has some drawbacks. First the wires have to pass through all the diamonds which becomes very long when there are many of them, especially when they are not aligned in the same direction. In addition, as mentioned before, there is friction

between the wire and the structure when it is activated or released. Finally, it is difficult to maintain all the wires totally tensed and the blockers in contact.

Another option exists to close the cells: using vacuum. The samples are simply inserted in airtight bags connected to a vacuum pump. In contrast with the wires which force locally the diamonds to be closed, vacuum acts directly on all the wall and closes the cell by reducing the area between the walls. The advantage of the vacuum is that the forcing is homogeneous: all the cells experience the same forcing and act together when the pump is turned on.

Airtight bags are made of thermosealable fabric. The fabric can be extensible or not and is coated with TPU. When the two sides coated with TPU are heated, the TPU melt and seal the bag. The samples are also 3D-printed in TPU, and can thus be stuck to the fabric if needed. In most cases, the bag is not stuck to the samples. As in the case of wires, a hole is designed at the center of the walls on selected lines to ensure a uniform pumping of the air in the entire sample. The pump provides a residual pressure below 0.1 bar.

3.5.1 Network of aligned diamonds under vacuum

What is the compressive strain generated by a pressure difference? To program complex shapes and solve the inverse problem with this technique, the strain of the cells as a function of the parameters should be known. We start by characterizing simple uniform networks described in part 3.2. The parameters that are changed from one experiment to another are : h , l , e , θ (figure 3.35).

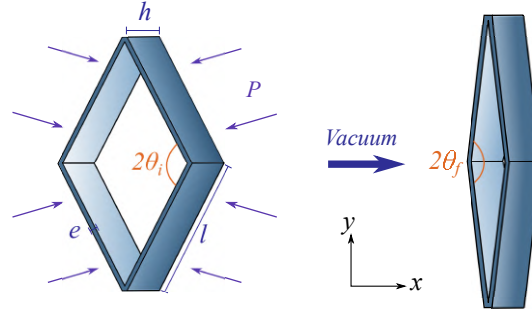


Figure 3.35 Diamond under vacuum. The area inside the cell decreases when the air is pumped out.

We first want to estimate the minimal pressure needed to completely close the cells. We firstly neglect the influence of the fabric in the closing of the cells and only consider small deformations $\epsilon \ll 1$. The total energy reads:

$$\mathcal{E}_{tot} = PV + \mathcal{E}_{elast} \quad (3.26)$$

with P the pressure applied on the cells, $V = h\mathcal{A}_{rea}$ the volume of one cell with \mathcal{A}_{rea} the area of the diamond, and \mathcal{E}_{elast} the elastic energy of one cell.

$$\mathcal{E}_{tot} = Ph\mathcal{A}_{rea} + \frac{1}{2}E^*h\mathcal{A}_{rea}\epsilon_x^2 \quad (3.27)$$

Changing shape by closing cellular structures

where ε_x is the strain in the x direction.

By conservation of the perimeters of the diamonds: $\varepsilon_x = -\tan^2 \theta \varepsilon_y$. At the first order, the area of the diamond can be written as $\mathcal{A}_{rea} \simeq A_0(1 + \varepsilon_x + \varepsilon_y) \simeq A_0(1 + \varepsilon_x(1 - \cot^2 \theta))$ where A_0 is the initial area of the cell. The energy can be thus written at first order:

$$\mathcal{E}_{tot} \sim PhA_0(1 + \varepsilon_x(1 - \cot^2 \theta)) + \frac{1}{2}E^*hA_0\varepsilon_x^2 \quad (3.28)$$

The equilibrium state is obtained by minimizing the energy with respect to ε_x :

$$\frac{\partial \mathcal{E}_{tot}}{\partial \varepsilon_x} = 0 \sim A_0h(P(1 - \cot^2 \theta) + E^*\varepsilon_x) \quad (3.29)$$

as $(1 - \cot^2 \theta) = \frac{\sin^2 \theta - \cos^2 \theta}{\sin^2 \theta} = -\frac{\cos 2\theta}{\sin^2 \theta}$, the linear strains can be written as:

$$\varepsilon_x = \frac{P}{E^*(\theta)} \frac{\cos 2\theta}{\sin^2 \theta} \quad \varepsilon_y = -\frac{P}{E^*(\theta)} \frac{\cos 2\theta \cos^2 \theta}{\sin^4 \theta} \quad (3.30)$$

The effective bending modulus $E^*(\theta)$ has been calculated earlier in equation 3.10 $E^* = \left(\frac{e}{l}\right)^3 \frac{\cos \theta}{\sin^3 \theta} E$:

$$\varepsilon_x = \frac{P}{E} \left(\frac{l}{e}\right)^3 \cos 2\theta \tan \theta \quad \varepsilon_y = -\frac{P}{E} \left(\frac{l}{e}\right)^3 \cos 2\theta \cot \theta \quad (3.31)$$

Thus we see that for $\theta > \frac{\pi}{4}$, $\varepsilon_x < 0$ and $\varepsilon_y > 0$: the cells close along the x direction. If $\theta = \frac{\pi}{2}$, $\varepsilon_x = \varepsilon_y$ the cells do not move with the pressure. Finally if $\theta < \frac{\pi}{4}$, $\varepsilon_x > 0$ and $\varepsilon_y < 0$: the cells close along the y direction. By programming the angle of the diamonds the direction of closing can be chosen.

We now estimate if the vacuum pump delivers high enough pressures to close the cells. If $\varepsilon_x \sim 1$, $P_{min} \sim E \left(\frac{e}{l}\right)^3 \sim 10^7(10^{-1})^3 \sim 10^4$ Pa. In the experiments, the residual pressure is below 0.1 bar, so that $\Delta P \gtrsim 0.9$ bar $> \delta P_{min}$, all the cells should close.

In the experiments, pictures are taken before and after putting the samples under an internal residual pressure of at most 0.1 bar. The total length and width of the samples as well as the length and width of each cell are measured on the two pictures. From these measurements, a final strain is computed. Both the global and local measurements are consistent with each other, which confirms that the closing of the cells is homogeneous across the sample. For better accuracy, the strain is taken for the total length because it includes all the cells and the measured displacement is larger.

NB: In this part, for simplicity we note compressive strain as positive (in contrast with the common definition in the rest of the manuscript).

When the total length is measured, it includes the empty areas that close but also the thickness of the walls that will define a minimal compacted length. A maximal strain is calculated for each dimension (length and high of the sample). This maximal strain, ε_{max} , corresponds to the strain that is obtained when all the cells are totally closed and the walls of the cells are totally in contact (for example $\varepsilon_{max_l} = \frac{L-2N_l e_h}{L}$). It is smaller when the walls are very thick. This value is reported on figure 3.36: it corresponds to the top points (blue stars). As the thickness of the wall is similar for all the sample, when

h is changed ϵ_{max} is quasi constant on this graph. In the following graphs, to get rid of this issue, ϵ is normalized by its corresponding ϵ_{max} ($\epsilon_{fin} = \frac{\epsilon}{\epsilon_{max}}$).

In the experiments, the internal pressure should provide strong enough forces to entirely close all the samples used and ϵ should be maximal for all samples. However, it appears that it is not true in the experiments. Indeed we did not consider the role of the fabric in the previous calculations.

When the strain ϵ is plotted versus the height h of the sample, a linear dependency appears (figure 3.36). Very thin samples barely close as seen on the left of figure 3.36. Conversely thicker samples almost totally close as seen on the right picture of figure 3.36. In the middle range the diamonds close but they also shear, a scale pattern appears (top left picture of figure 3.36).

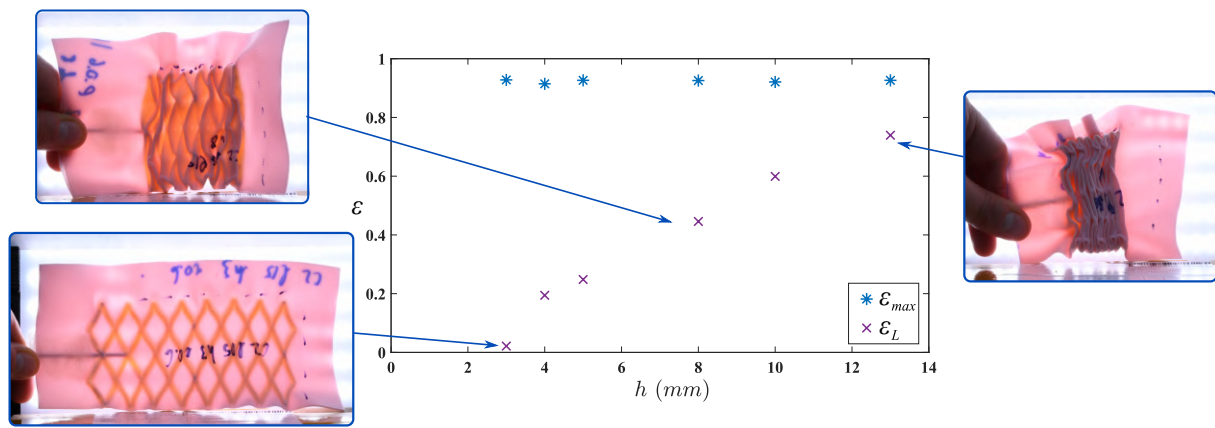


Figure 3.36 Compression ϵ as a function of the height h of the samples for e , l and θ constant. In blue star the theoretical maximal compression and in purple cross the experimental points.

The thicker the samples (large h), the more they close. The closing strain is smaller than expected because the fabric is suck into the cavities (figure 3.37). If the samples are too thin the fabric from both sides gets into contact and prevent in-plane closing. Thick samples (large $\frac{h}{l}$) undergo stronger in-plane compression. However if they are too thick the bending of the structure becomes more difficult. We expect that getting 3D-shapes out of planar sample (which is our final goal) will become more difficult.

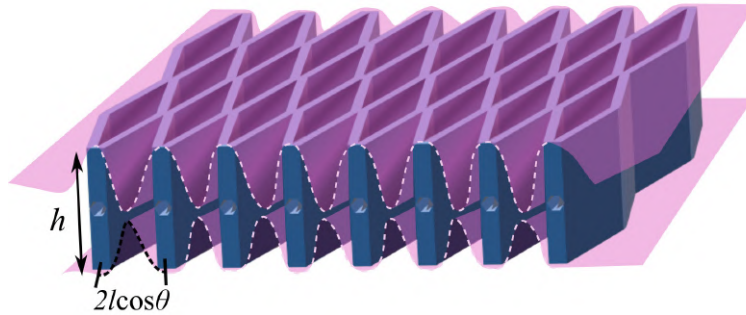


Figure 3.37 Network of aligned diamonds under vacuum. The fabric is sucked inside the cells when the sample is activated.

The other parameters l , e and θ also have an effect in vacuum closing. Changing the thickness e of the walls does not seem to have a strong effect as long as $\frac{e}{l} \ll 1$. Overall, closing strains tend to decrease when the thickness e of the walls is increased but the trend is not clear. In the following measurement, e is kept constant.

When θ is large, the cells are almost closed in the initial state, the final strain is higher than for small θ , the final state is closer to the total closing of the cells. It can also be noticed that the final strain is lower when l increases.

These two trends seem to be consistent with the fact that the fabric penetrates inside the cells. The area inside the cell in the initial state depends both on the l size of the cell and the initial angle θ . When both parameters increase, the initial area increase and thus the fabric gets more easily stuck inside the cells, stopping the closing.

A simple approach to try to determine the closing amplitude consists in assuming that the closing stops when the fabric of both sides get into contact. The fabric is considered inextensible and to not slide on the sample. The fabric of one side gets in contact with the other side when (figure 3.37):

$$2l \cos \theta_i = h \quad (3.32)$$

This should correspond to the maximal strain if there is no sliding of the fabric. If $2l \cos \theta < h$ the strain should be 1 as the fabric of both side cannot touch. For shallower samples, we expect the maximal strain to be (figure 3.37):

$$\varepsilon_{th} = \frac{h}{2l \cos \theta_i} \quad (3.33)$$

This equation is consistent with the observations made just above. When h or θ_i increase, the contraction strain increases but when l increases, the strain decreases.

The strain that is measured is normalized by ε_{max} and plotted against the approximated strain $\varepsilon_{th} \frac{h}{2l \cos \theta_i}$ (figure 3.38). The thickness of the walls e is kept constant. For $h > 2l \cos \theta$, the strain should

be maximal and equal to 1 as the fabric sides are not in contact and or $h < 2l \cos \theta$, the points should align with the slope 1 (orange dashed line in figure 3.38).

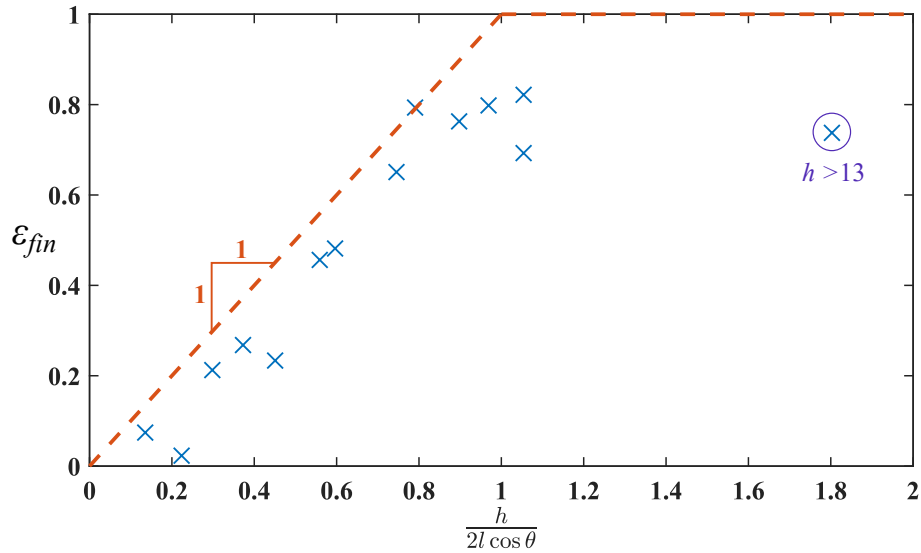


Figure 3.38 Normalized final strain plotted as a function of $\frac{h}{2l \cos \theta}$ for $e \sim 0.6\text{mm}$.

The experimental points (blue cross) do not totally collapse on the prediction, as the fabric has a finite size ($e_f = 0.65\text{mm}$), it should be taken into account in the estimation of ϵ_{max} . Considering the thickness of the sample, another ϵ_{max} can be calculated ($\epsilon_{max_2} = \frac{L - 2N_l(e_h + e_f)}{L}$). The new final strain ϵ_{fin_2} is thus plotted as a function of $\frac{h}{2l \cos \theta}$ (figure 3.39). The experimental points seem to better fit the prediction than for figure 3.38.

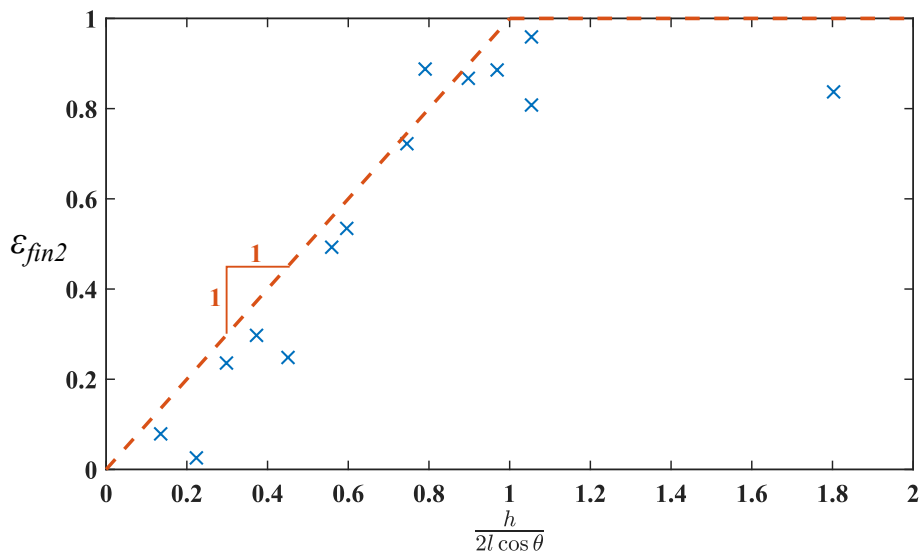


Figure 3.39 Normalized final strain plotted as a function of $\frac{h}{2l \cos \theta}$ for $e \sim 0.6\text{mm}$. The thickness of the fabric e_f is taken into account in the normalization.

Changing shape by closing cellular structures

Thus, at first order, the scaling law seems to be valid. However, the two hypotheses made are not totally respected. The fabric used is slightly extensible and the samples may move freely in the fabric bag. In practice, the sample does not slide much in the bag and the stretching of the fabric remains small. As both factors change the size of the fabric that is inside the cells in an opposite way the actions may compensate.

These two requirements could be met but the stretchy fabric and the loose bag where the sample can slide are used on purpose. Indeed, when the diamonds are activated, the short diagonal of a unit cell is compressed while the long one is elongated. A stretchy envelope favors smoother deformations and limits incompatibilities. As seen in figure 3.40, when the fabric is not extensible (right panel, grey Nylon fabric), the closing is not very smooth and they are many folds. As the long diagonal cannot stretch, it causes some frustration that tends to bend the diamonds in the other direction.

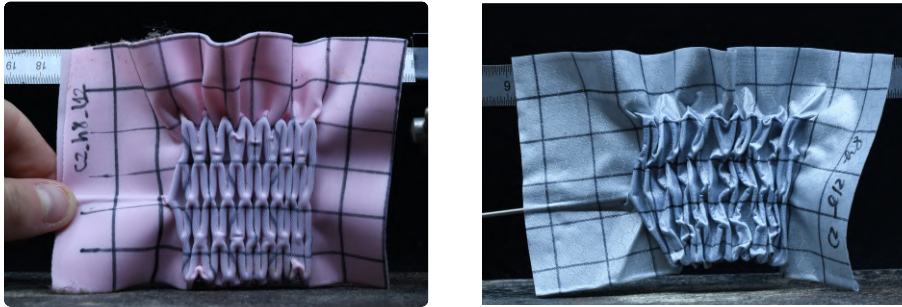


Figure 3.40 Networks with $C = 2$, $l = 12\text{mm}$, $h = 8\text{mm}$, $e_p = 1\text{mm}$ in a pink bag of extensible fabric (left) and in a grey bag of non extensible fabric (right). The extensible envelope leads to smoother collapsed shapes.

In conclusion, when cells close, the volume inside the cells decreases faster in the presence of a deformable fabric and thus help the closing. At the beginning, the fabric helps to deform by reducing the “pressure energy” component PV but as this energy is rapidly consumed the closing saturates. Having fabrics around the sample fasten the closing but stops it sooner. In order to observe the larger strain, it is better to use small cells with high wall. However the walls have to be small enough to allow bending and out of plane deformation.

Using vacuum does not allow to increase the rigidity of the samples. As the fabric goes inside the cells there is no real blocking of the shapes. Once the sample are under vacuum the walls do not touch and cannot be considered as a bulk material.

3.5.2 3D shapes with vacuum

When trying to do shape morphing, we select the pink extensible material to obtain smoother shapes. When the networks with blockers are put inside the bag, they only close of a very small amount. The fabric gets stuck on the blockers and only a small amount of fabric goes inside the cell in between the blockers. As blockers cannot be used in this configuration, the shapes have to be programmed by changing the orientation of the diamonds in space or the different geometrical parameters.

The strain of the cells depends on l , θ and h . Changing h across the sample is complicated and does not seem appropriate to 3D printing on a plate. Paving the space with diamonds with different lengths and angles is possible but quite complicated. It would be interesting but requires solving simultaneously the tiling and the local strain. We thus start by printing samples where diamonds have different orientations.

As in the second chapter 2 and in the section with the wires, the plane is paved by diamonds with similar angles, and they are subdivided when they get too large. The thickness e of the walls is also set to be proportional to the length l of the side of the diamonds to maintain the same stiffness E^* everywhere. To draw such diamonds, logarithmic spirals are used, as in the second chapter 2. The internal angle θ of all diamonds depends on the pitch of the spiral. They can be radially elongated (figure 3.41) or orthoradially elongated (figure 3.42). The final shapes obtained are opposite to the one get in the second chapter 2: indeed, the changes in distances due to vacuum have opposite signs compared to the case of expanding matrix.

In the case where diamonds are radially elongated (figure 3.41), the depression tends to shrink the perimeters and increase the radii. Considering that the contraction is the same for every ring as the angle is kept constant, a cone with a positive Gaussian curvature should emerge.

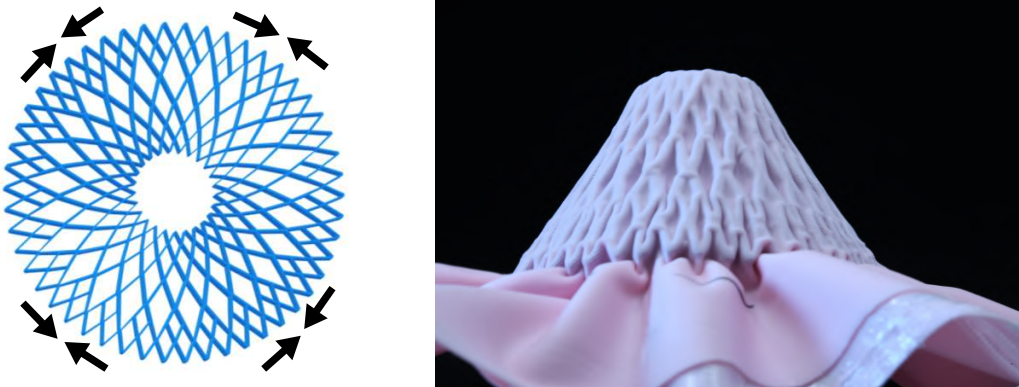


Figure 3.41 Diamonds network organized along logarithmic spirals with large angle $\theta > \frac{\pi}{4}$. When the sample is put under vacuum, the cells close in the orthoradial direction and a conical shape emerges.

In the case where diamonds are orthoradially elongated (figure 3.42), the depression tends to close the cells along the small diagonal, the radii shrink and the perimeters stretch. Considering that the squeezing is the same for every ring (as the angle θ is kept constant), an e-cone should emerge with a localized negative Gaussian curvature at the pole.

Changing shape by closing cellular structures



Figure 3.42 Diamond network organized along logarithmic spirals with small angle $\theta > \frac{\pi}{4}$. When the sample is put under vacuum, the cells close in the radial direction and an e-cone emerges

As in the last section of the second chapter figure 2.4.2.b, space can also be paved by diamonds with different shapes and sizes. If the same curve is drawn many times translated by the same distance and is added to its mirror image, a network of diamonds appears. In this case, the angle θ of the diamonds changes gradually from the center to the edge. If the angle increases gradually from the center to the edges, the compression is vertical in the center and horizontal on the edges. The center line gets “longer” than the edges so a positive Gaussian curvature appears (figure 3.43).

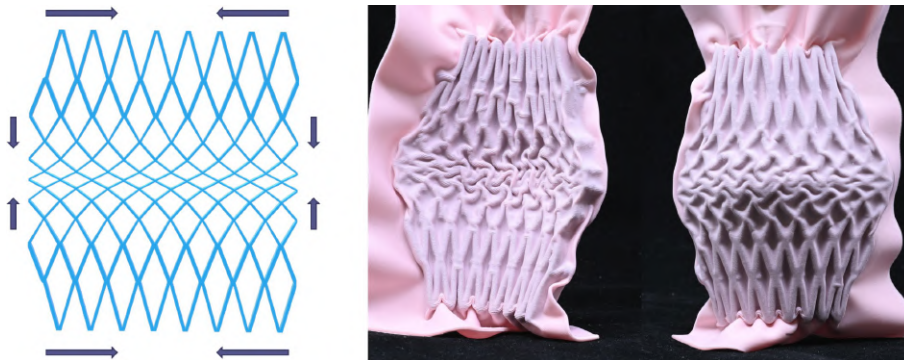


Figure 3.43 Diamond network with contraction in the vertical direction in the center and in the horizontal direction on the edges. The angle of the diamonds increases gradually from the center to the edges. When under vacuum, a positive Gaussian curvature appears.

If on the contrary, the angle decreases gradually from the center to the edges, the compression is horizontal in the center while vertical on the edges. The center line gets “shorter” than the edges so a negative Gaussian curvature, an helix-like appears (figure 3.44).

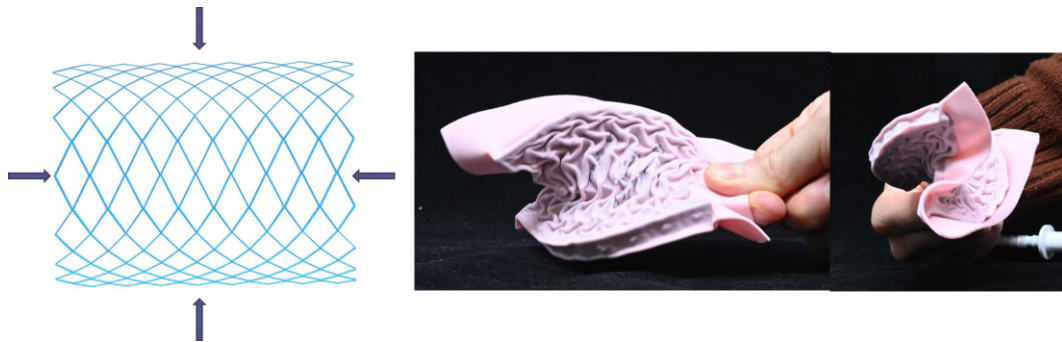


Figure 3.44 Diamond network with contraction in the horizontal direction in the center and in the vertical direction on the edges. The angle of the diamonds decreases gradually from the center to the edges. When under vacuum, a helix with a negative Gaussian curvature appears.

3.6 Rectangular unit cells

In this chapter we mainly focused on diamond shape networks but other kind of patterns can be used for activation with vacuum.

One of the other designs we have tested is the following: rectangles are aligned in a cartesian grid and are shifted by one half of their length from one row to another (figure 3.45). This particular tiling allows the global sample to reduce its width by a factor of two, keeping the length constant as can be seen in figure 3.45.

Unlike the diamonds, the deformation in the direction perpendicular to the direction of contraction is nearly zero. This property is convenient when using the vacuum in bags because they do not need to stretch the external pocket.

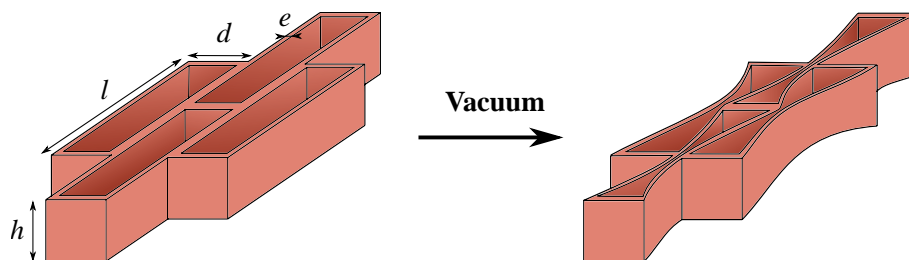


Figure 3.45 Network of aligned rectangles shifted of half a length from one row to the next, before and after being activated by vacuum

In the case of the rectangles, the strain does not depend on the parameters of the cells, it is always 0.5 (considering the wall infinitely small) and cannot be higher than 0.5. In order to program 3D shapes, the orientation of the rectangle must change spatially. However, some specific ratios are kept constant in order for the rigidity to be the same everywhere in the sample.

Considering that $h \gg d$ and $l \gg d$, when the cells are closed (figure 3.45), for a deflection δ at the center of the beam, the long side l is bending with typical curvature $\frac{\delta}{l^2}$. The bending related energy is:

$$\mathcal{E}_{bend} \sim E e^3 h \left(\frac{\delta}{l^2} \right)^2 l \quad (3.34)$$

where E is the Young modulus of the sample, h the height, e the thickness of the walls, l the length of the long side and d the length of the small side.

If we want that all the cells close in a similar way when placed under vacuum, the effective bending modulus E^* of the sample have to be constant over the sample. The bending energy of a cell is:

$$\mathcal{E}_{bend} = \frac{1}{2} E^* \varepsilon^2 h l d = \frac{1}{2} E^* \left(\frac{\delta}{d} \right)^2 h l d \quad (3.35)$$

with $\varepsilon = \frac{\delta}{d}$ the strain corresponding to deflection δ at the center of the beam of length l . By identification:

$$E^* = \left(\frac{e}{l} \right)^3 \frac{d}{l} E \quad (3.36)$$

Keeping the aspect ratio $\frac{l}{d}$ of the cell constant, the ratio $\frac{l}{e}$ has to be kept constant in order to conserve E^* across the sample.

In order for the cells to totally close, the global strain of the sample $\varepsilon > 0.5$. $\varepsilon = \frac{P}{E^*}$, so the following inequality has to be satisfied:

$$\frac{P}{E} \left(\frac{l}{e} \right)^3 \frac{l}{d} > 0.5 \quad (3.37)$$

Considering that the aspect ratio of the cell is set to $\frac{l}{d} = 3$:

$$\frac{l}{e} > \left(0.5 \frac{d E}{l P} \right)^3 \sim \left(0.5 \frac{1.5 \cdot 10^7}{3 \cdot 1 \cdot 10^5} \right)^{1/3} \sim 5 \quad (3.38)$$

If this inequality is respected, the pressure should close the cell (only the fabric could interfere). In the design, this ratio is set between 10 and 50 to be sure that all cells close. The fabric seems to be less an issue with this design because there is still some “volume” that is available at the two ends when the cells are closed.

3.6.1 3D shapes with angular sectors

We start, as we did for the diamonds, to arrange rectangles radially or orthoradially. As it is difficult to pave a disk with rectangles, we chose to use curved rectangle (sectors) to pave the disk. Depending on the orientation, of the long axis of the rectangles, it is possible to obtain positive or negative Gaussian curvatures.

In order to program positive Gaussian curvature, the rectangles have to be elongated along the radial direction (figure 3.46) and shrink mainly azimuthally. The disk is divided into angular sectors which are closed with straight segments. Rectangles are shifted by half their length between the two neighbor sectors.



Figure 3.46 Rectangles with their long axis orientated in the radial directions before (left) and after (right) being activated by vacuum. When the cells close, the perimeters shrink while the radius keep their length: a shape with positive Gaussian curvature emerges.

In order to program negative Gaussian curvature, the rectangles must be orthoradially elongated. Concentric rings are drawn keeping the aspect ratio $\frac{l}{d}$ constant and the number of rectangle per ring constant. When rectangles get too large they are subdivided to keep them relatively small compared to their curvature. From one ring to the next, the rectangles are shifted by half their length.

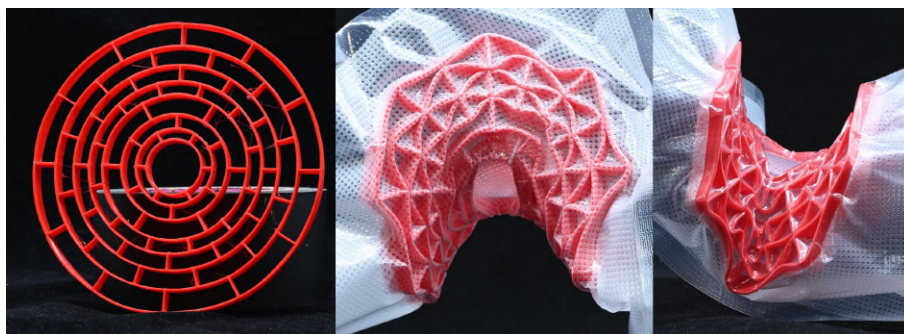


Figure 3.47 Rectangles with their long axis orientated in the orthoradial directions before (left) and after (right) being activated by vacuum. When the cells close, the radius shrink while the perimeters keep their length: a shape with negative Gaussian curvature emerges.

As shown in figures 3.46 and 3.47, these qualitative design rules indeed lead to the production of the expected family of shapes.

3.6.2 3D shapes from logarithmic spirals

Logarithmic spirals can also be used to arrange rectangles. The notation are the same as in section 2.4.2.a. They are drawn starting from the center, all in the same direction with a given spiral angle. The subdivision of these portions is done by arc of spirals in the perpendicular direction.

As before, between neighbors section of spirals, the rectangles are shifted by half their length. In this case it is difficult to have them shifted exactly by half their length because the spirals rotate. If a portion is exactly shifted of half a rectangle with the previous portion, it will not be well shifted with the next section. Moreover, keeping the aspect ratio $\frac{l}{d}$ constant on the disk makes the shifting even more difficult.

Changing shape by closing cellular structures

To keep a significant shift of the rectangle from a spiral to another, the length of the first rectangle of the even spiral is multiplied by a number between 0.5 and 1 depending on the angle β of the spirals.

When the angle of the spiral β varies from $\frac{\pi}{3}$ to $\frac{\pi}{10}$, the shape of the sample varies from an e-cone (figure 3.48) to a cone (figure 3.49). The strain direction is perpendicular to the direction of the spirals. The two previous cases are limit case of the spirals with $\beta = 0$ and $\frac{\pi}{2}$.

Having spirals allow to have strains in both the radial and orthoradial directions. The distribution between the two depends on the value of the angle β of the spirals. When β is smaller than $\frac{\pi}{4}$, the shape has a negative Gaussian curvature (figure 3.48). When β is larger than $\frac{\pi}{4}$, the shape has a positive Gaussian curvature (figure 3.49). A similar behavior will be observed in section 4.3.2.



Figure 3.48 Logarithmic spirals with an angle $\beta = \frac{\pi}{3}$. The aspect ratio of the cells $\frac{l}{d}$ as well as the ratio $\frac{e}{l}$ are kept constant. As the cells close, a shape with a negative Gaussian curvature emerges.

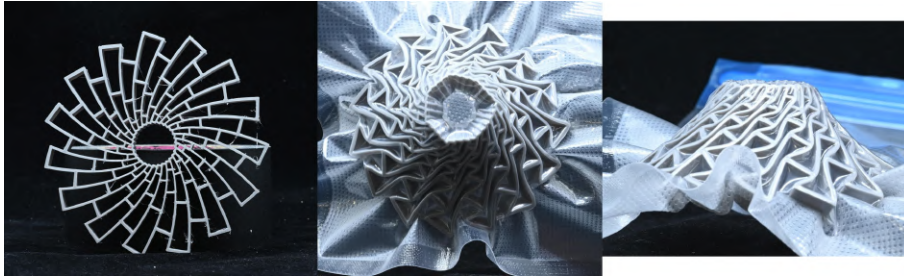


Figure 3.49 Logarithmic spirals with an angle $\beta = \frac{\pi}{10}$. The aspect ratio of the cells $\frac{l}{d}$ as well as the ratio $\frac{e}{l}$ are kept constant. As the cells close, a shape with a positive Gaussian curvature emerges.

By keeping the aspect ratio $\frac{l}{d}$ of the cells as well as the ratio $\frac{e}{l}$ constant in the sample, the deformation of the sample is homogeneous and all the cells close at the same time. With this homogeneous activation, in the case of the negative Gaussian curvature (figure 3.48), the shape first close in plane before going out of plane when the forces are strong enough to bend the sample in its height.

3.7 Conclusion

In this chapter, we have studied the mechanics and geometry of shape change in networks of diamond unit cells.

We found that the low bending stiffness of the beams in the network provides a mode of deformation that couples expansion in one direction and contraction in the perpendicular one. We characterized the corresponding elastic stiffness, both in-plane and out-of-plane.

We showed how to control the amplitude of deformation by inserting blockers that limit the movement of the beams. We used this technique to program axisymmetric shapes when internal wires are put under tension. We also demonstrated experimentally a method to program arbitrary shapes (the compass method).

Another way to activate these structure is to put them inside an airtight pocket from which air is pumped. External pressure partially closes the compliant network, depending on its geometry. We showed that this can be used to induce the spontaneous buckling into simple axisymmetric 3D shapes.

We note that actuation through wires is very efficient as it provides very large contractions, because we can arbitrarily impose the direction of contraction. However, it requires manual installation of the wires, which turned out to be very time consuming. The depressurization of an external pocket is simpler and really appealing. We conclude that these metamaterials do present very interesting shape-change properties that can be programmed rather simply and manufactured with any consumer-grade 3D printer.

An obvious extension of this work would be to study the possibility of programming more complex shapes through negative pressure. One possibility would be to extend the strategy used for the axisymmetric shapes: use diamonds with (almost) the same shape, and only use their orientation as a parameter for programming, adapting theoretical tools developed for liquid crystal elastomers [15]. We also could translate inverse problems developed for uniaxial contraction[80] to the network of rectangles. It might also be interesting to program a spatial distribution of stiffness which would produce different local deformation (and adapt the compass method, for example). In all these cases, we will have to solve challenging geometrical puzzles.

Another question that we did not tackle is the geometrical precision of the morphing. In this study, we have mainly triggered in-plane deformations (metric distortion) to obtain 3D shapes. This method implicitly assumes that the sheets are very thin, or more exactly that bending to stretching stiffness (which scales as a length square, the thickness) is very small, so that the system will "obey" the metric at the cost of any curvature. It would be interesting to estimate and control this parameter in our system. But we note that the mechanical properties are strongly anisotropic. Indeed, the beams in our networks tend to have a ribbon-like geometry, which hinders some specific bending directions of the resulting structure seen as an equivalent plate. Could this limit the family of 3D surfaces available as target for morphing?

In the next chapter, we consider a very different type of matrix for the actuation of these structures: a simple soap film...

Chapter 4

Sculpting soap films

In the previous chapters we show how to change shape using cellular structures which were able to expand or contract. Two different strategies have been developed to contract the structures: wires and pressure. In the search for new ways of reducing the area of cells in cellular structures, surface tension appears to be an elegant solution. Surface tension tends to minimize the area and thus to close the cells. It seems that the structures developed in the other chapters of the thesis could be dipped in a soap bath and should then deform. In reality, we will see that the designs have to be adapted: they have to be very thin, and the geometrical parameters have to be changed.

The work of this chapter has been done in collaboration with Pierre-Brice Bintein with the help of Rémi Abdallah.

Contents

4.1 Introduction	111
4.2 Unit cell and principle	113
4.2.1 Networks of aligned cells	114
4.3 Deploying 3D structures	124
4.3.1 Aligned rectangles on a cone	124
4.3.2 Logarithmic spirals	129
4.3.3 Influence of the curvature of “rectangular” cells	133
4.4 Other types of cells	136
4.5 Conclusion	137

4.1 Introduction

Capillary forces are often negligible but they can be dominant at small scale. In order for the capillarity forces to have an influence on the object we consider, the capillary force has to be stronger than the other forces involved. In scaling law, for a structure with a typical length of L , the capillary

Sculpting soap films

force scales like L whereas the pressure force scales like L^2 and volume forces such as gravity scale like L^3 . For large L , the capillary force does not influence the behavior of the structure. The capillary forces begin to have an influence when the typical length of the structure is small. For example when the typical length L is smaller than the gravito-capillary length L_c :

$$L_c = \sqrt{\frac{\gamma}{\rho g}} \quad (4.1)$$

(with γ the surface tension, ρ the density and g the gravity), droplets are spherical when deposited on a surface instead of flat.

Surface tension is mostly known for its effect on liquid surfaces but capillary interactions can also deform bodies that are soft enough [111]. In this chapter we will focus on the coupling between capillary and elastic forces. This coupling can generate many different behaviors, 3D deformation of bulk solids, 1D bending of rod-structure or 2D bending or stretching of thin sheets.

When a droplet of liquid is deposited on a solid substrate, due to vertical component of the force on the substrate, the substrate can be deformed if it is soft enough [112]. The deformation of such bulk elastic solids with surface forces scales with the ratio $\frac{\gamma}{E}$ [113], on the order of at tenth of micron even for soft elastomers.

Bulk deformations are often quite small compare to the size of the object, but using slender structures instead will generate larger deformations due to capillary forces. This phenomenon is for example present in nature and explains why wet hair bundle [114]. Another example or flexible lamellae that collapsed with capillary forces can be used to mimic the opening of ferns of temperate forests. The shell of the spore capsule is composed of parallel water cavities separated with lamellae. When the water evaporates, the lamellae collapse and open the capsule releasing the spores [115] [116] (figure 4.1).



Figure 4.1 Fern capsule model opened with capillary forces [116] [113]

In order to understand why such slender structures (rod or thin sheets) deform, the capillary forces have to be compared with the bending forces. In a similar way as the gravito-capillary length, an elasto-capillary length L_{ec} can be defined. This length compares the bending stiffness to the surface tension, and gives the typical curvature that the capillary forces induced on flexible slender structure. Considering a thin plate of length L and thickness h :

$$L_{ec} = \sqrt{\frac{B}{\gamma}} \sim \sqrt{\frac{Eh^3}{\gamma}} \quad (4.2)$$

with $B \sim Eh^3$ the bending modulus. The deformation of the object becomes significant when the typical length of the sample L is much larger than L_{ec} .

Thus, for objects that have a typical length higher than the L_{ec} , capillary forces are strong enough to bend the object, it can be thin sheet or rods. It is then possible to fold thin sheets in 3D such as the “Capillary origami” [117]: an elastic sheet self may wrap when a liquid droplet is deposited.

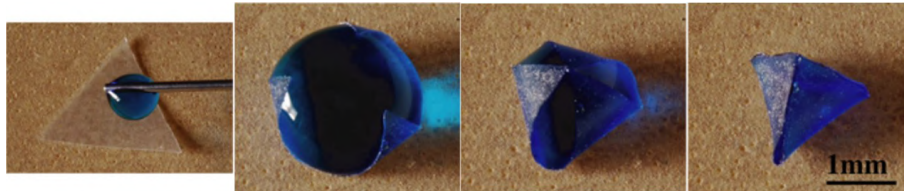


Figure 4.2 Folding on a “capillary origami” from article [117]

In the examples cited above, the liquid was most of the time water drops, but soap films can also be used to bend structures. Using soap instead of water allows one to create films (rather than drops) that may deform closed structure such as flexible rod loop [118, 119]. The soap film tends to adopt a minimal surface and adopt a negative Gaussian curvature. Instead of a rod, a 2D ring can be used, when a soap film is only put inside the ring, the ring buckle to reduce the radius of the ring [120]. Soap can even be used to fold thin ribbons [121] or thin flexible sheets [113] (figure 4.3).

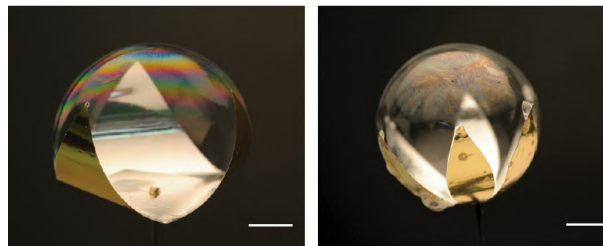


Figure 4.3 Folding on a “capillary origami” with soap bubble from article [113]

Capillary forces can also be used to deform cellular structures and change the pattern of the network [122].

In our work, we also propose to deform cellular structures of slender beam with soap film such as they become 3D shape. The design mostly used is the rectangle. Putting a soap film inside a rectangle makes it close as the long sides bend. This shape is for example used to create small tensiometers by measuring the deflection of the long sides [123] or to measure surface tension profile in vertical soap film by probing the surface tension locally [124].

4.2 Unit cell and principle

We start by using rectangles as in section 3.6. When such a rectangular frame is dipped and withdrawn from a soap water bath, a soap film forms on the frame. As surface tension tends to minimize

Sculpting soap films

the film area, the rectangles tend to close along their widths (figure 4.4). We consider a uniform assembly of rectangles aligned along the same direction. The rectangles are shifted by half a length from one row to the next (as in section 3.6). When the soap film is laid on the structure, we expect the network to contract by a maximal factor 2. However, experiments show that depending on the geometrical parameters of the networks, the rectangles close by different amount when the soap is added 4.4.

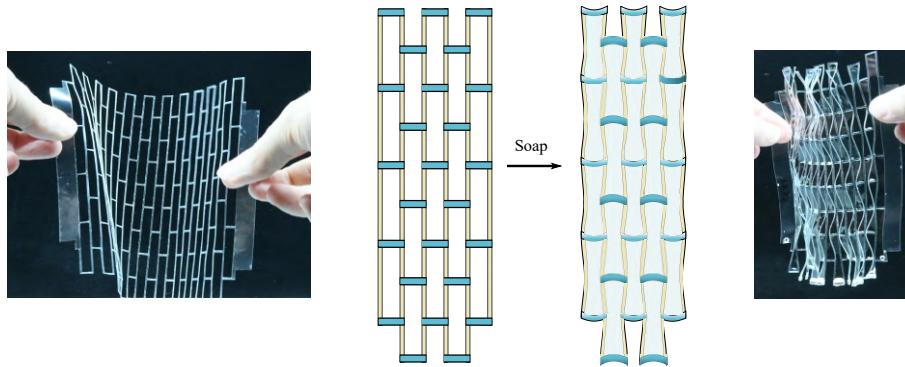


Figure 4.4 Network of rectangles without (left) and with a soap film (right).

In the following part we will explain how to use these rectangle unit cells to create 3D shapes but we first focus on the unit cells and determine the geometrical characteristics of cells which ensure their closing by surface tension.

In experiments, we use thin sheets of Mylar that we laser cut in different geometries. *NB*: Because of this fabrication process, the beams forming the rectangles are often ribbon-like (with a width much larger than their thickness).

4.2.1 Networks of aligned cells

As a first approach, we consider a network of aligned rectangles shifted by half a length from one row to the next (figure 4.4). To estimate the deformation of the networks by surface tension, we compare the surface energy with the elastic bending energy of the rectangles.

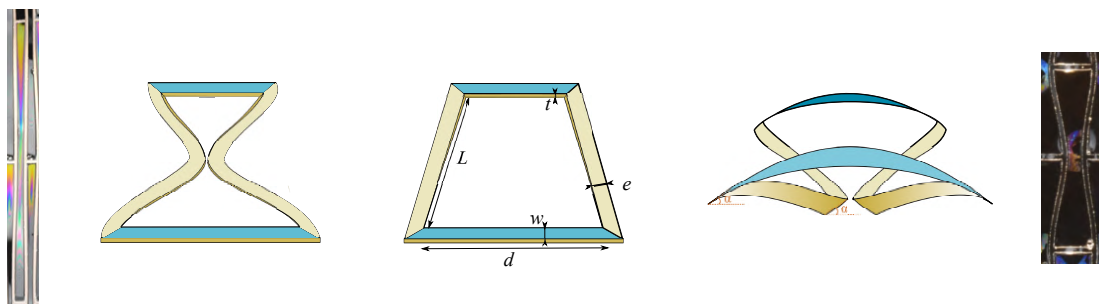


Figure 4.5 Scheme of the rectangle before activation (center) and after closing in its plane (2D case, left) and 3D case (right).

When the rectangles close, two modes of deformation are observed: a 2D deformation (in the initial plane of the network) and a 3D deformation (out of the initial plane of the network). Depending on the geometrical parameters, the rectangle goes out of plane when closed (figure 4.5 right) or remains in the plane (figure 4.5 left).

In the following, we characterize the closing of rectangles by the minimal distance X between the two opposed sides. X varies from 0 (totally closed) to d (totally open) (figure 4.6).

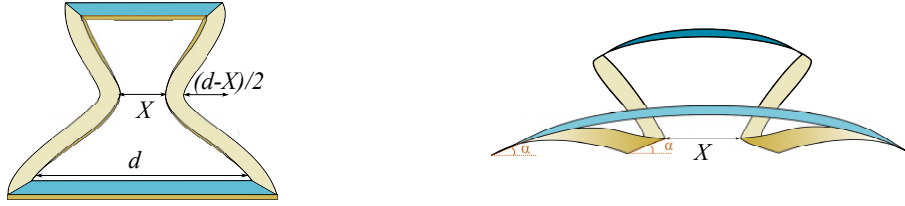


Figure 4.6 Sketch of a rectangle partially closed in 2D (left) and 3D (right).

When the width of the cells is reduced to a distance X (for both 2D and 3D case), the energy gain of surface tension that is provided to the system is of the order of:

$$\mathcal{E}_{soap} \sim \gamma(d - X)L \quad (4.3)$$

where γ is the surface tension of the soapy water, L , d and X respectively the inside length and width of the rectangles and the distance between the two sides (see figures 4.5 and 4.6).

We now estimate the elastic energy of deformed cells, first for in-plane deformations, and then for 3D deformations. In this section we will consider that the sides are relatively thin $d \gg e$ and $L \gg w$. We also assume that cells are elongated: $L \gg d$ (see figure 4.5 for definitions).

4.2.1.a Case of in plane deformation

When the cells close in 2D (in-plane deformation), the sides of the rectangles bend in the perpendicular direction. As the cells are elongated ($L \gg d$), it can be considered that only the sides of length L bend. The deflection at the center of the side is approximately $\delta_{2D} \sim \frac{(d-X)}{2}$ (figure 4.6 left). The related elastic energy can then be written as :

$$\mathcal{E}_{elast2D} \sim Ee^3 \left(\frac{\delta_{2D}}{L^2} \right)^2 Lt \sim E \frac{e^3 t (d-X)^2}{L^3} \quad (4.4)$$

where E is the Young modulus of the network, e , L , d , t and X detailed in figure 4.5 and 4.6.

At equilibrium, the elastic energy balances the work of surface tension :

$$E \frac{e^3 t (d-X)^2}{L^3} \sim \gamma(d - X)L \quad (4.5)$$

so that:

$$(d - X) \sim \frac{\gamma L^4}{E e^3 t} \quad (4.6)$$

Thus the sides of length L are always bent (at least slightly) by the presence of the soap film but the deflection of the sides becomes significant and noticeable with bare eyes when the deflection is close to d . When the cells are totally closed ($X = 0$), the following equation is verified:

$$\frac{E e^3 t d}{\gamma L^4} \sim c^{st} \quad (4.7)$$

Equation 4.6 becomes $(d - X) \sim \frac{d}{A_{2D}}$ and we define the elastocapillary number $A_{2D} = \frac{1}{\varepsilon_{2D}} = \frac{E e^3 t d}{\gamma L^4}$, with perfect closing occurring for $A_{2D} = c^{st}$.

4.2.1.b Case of 3D deformation

We now consider the case of rectangles that deform out of plane. We consider that there is no twisting but only bending of the sides.

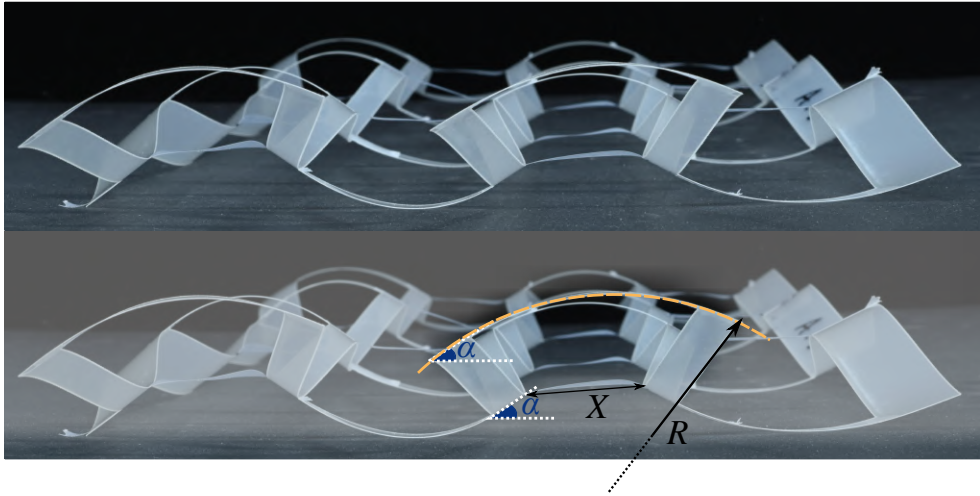


Figure 4.7 Rectangle network close mechanically with a distance X between the two long sides. The small edge bends in half a circle and the angle α is conserved as expected

We also assume that the small sides d bend with a constant curvature of radius R (orange portion of circle in figure 4.7). From the pictures and the experiments, a single cell partially opened can be drawn as in figure 4.8.

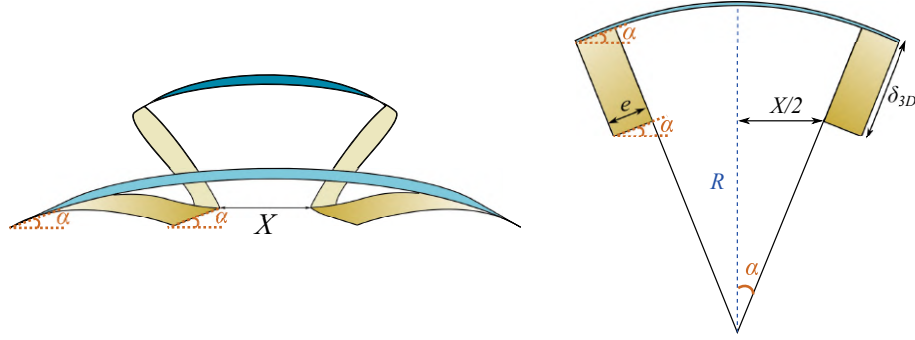


Figure 4.8 3D deformation of a unit rectangle (left) and its schematic side view (right) when the cell is partially closed with a distance X between the sides.

When the rectangle is deformed, both the ribbon along the width d (blue in figure 4.8) and the ribbon along the length L (yellow in figure 4.8) of the rectangle bend. Looking at the sketch (figure 4.8 right) of the experiment, the curvature of the small side is $\kappa \sim \frac{2\alpha}{d}$.

The bending energy of the width d (blue in figure 4.8) can be written as:

$$\mathcal{E}_{elast3D_d} \sim EI_d d \kappa^2 \sim Et^3 \frac{w\alpha^2}{d} \quad (4.8)$$

where $I_d \sim t^3 w$ is the second moment of inertia of the ribbon, E the Young modulus of Mylar and t , e , w , α are defined in figure 4.5.

We now estimate the bending of the ribbon forming the rectangle length L (yellow in figure 4.8). The deflection δ_{3D} can be deduced and approximated from the geometrical parameters:

$$\delta_{3D} \sim R - \frac{X}{2 \sin \alpha} \sim \frac{d}{2\alpha} - \frac{X}{2\alpha} \sim \frac{(d-X)}{\alpha} \quad (4.9)$$

in the case of elongated cells ($L \gg d$). Thus the bending energy of the ribbon of length L can be written as:

$$\mathcal{E}_{elast3D_L} \sim EI_L L \left(\frac{\delta_{3D}}{L^2} \right)^2 \sim Et^3 e \frac{(d-X)^2}{\alpha^2 L^3} \quad (4.10)$$

with $I_L \sim t^3 e$ the second moment of inertia of the other ribbon.

The total 3D bending energy is thus:

$$\mathcal{E}_{elast3D_{tot}} \sim Et^3 e \frac{(d-X)^2}{\alpha^2 L^3} + Et^3 \frac{w\alpha^2}{d} \quad (4.11)$$

where the angle α of bending is unknown at this point. We find α_{eq} by minimizing the total energy with respect to α .

$$\frac{\partial \mathcal{E}_{elast3D_{tot}}(\alpha_{eq})}{\partial \alpha} \sim 2Et^3 \left(\frac{w\alpha_{eq}}{d} - \frac{e(d-X)^2}{L^3\alpha_{eq}^3} \right) = 0 \quad (4.12)$$

so:

$$\alpha_{eq}^4 \sim \frac{e}{w} \frac{d(d-X)^2}{L^3} \quad (4.13)$$

The value of this angle α_{eq} as a function of the different geometrical parameters can be measured experimentally using a different, simpler experiment (figure 4.9). Large stiff networks cut in thick Mylar sheet are closed at the center of every cell by a piece of tape of a given length X . The measures are not directly taken on samples dipped into soap bath because it is very difficult to take pictures on which the angles can be measured. Using tape allows us to test the “dry” samples with many different geometries as the closing distance X is defined and not the force to close the cells.

For the different samples, in a first series of experiments, the aspect ratio $\frac{d}{l}$ is kept constant with $l = 50\text{mm}$ and $d = 10\text{mm}$, choosing $e = 2$ or 4mm and w varying from 2 to 15mm. Then in a second series, the ratio $\frac{e}{w}$ is kept constant with $w = e = 4\text{mm}$, varying l between 40 and 100mm and d between 10 and 60mm.

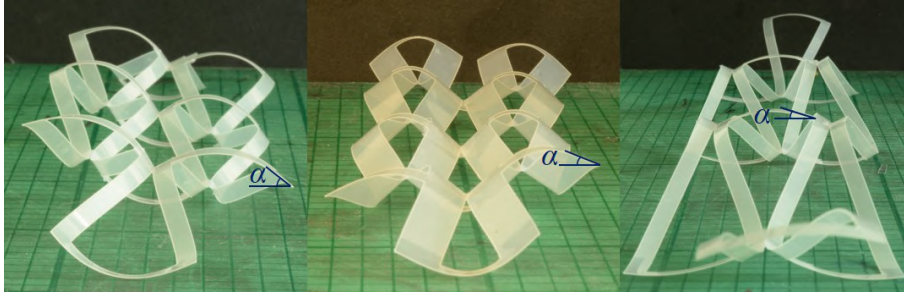


Figure 4.9 Networks closed at contact with tape. The angle α is measured for different geometrical parameters.

The different α_{exp} that are measured are plotted as a function of the theoretical prediction of equation 4.13: $\alpha_{th} = \left(\frac{ed(d-X)^2}{wL^3} \right)^{1/4}$ (figure 4.10).

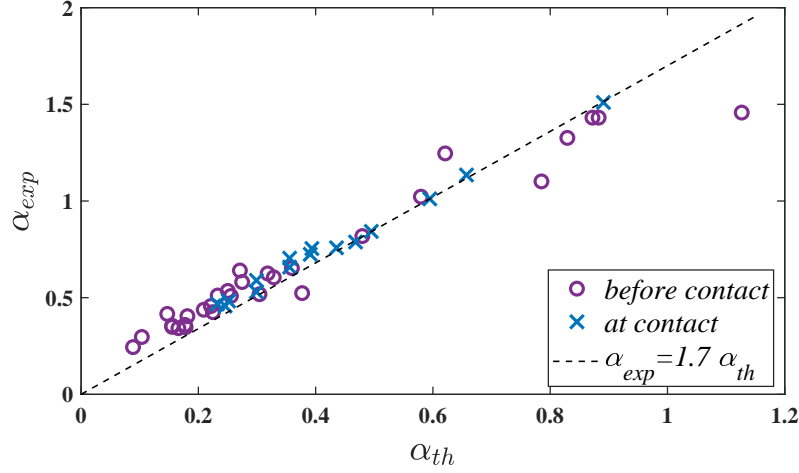


Figure 4.10 Measured α_{exp} as a function of the theoretical α_{th} , varying e from 2 to 4mm, w from 2 to 15mm, d from 10 to 60mm and L from 40 to 100mm. A linear fit is done with a resulting slope of 1.7 (dashed line). In blue cross the measures for $X = 0$ at contact and in purple circles the measures for $X \neq 0$.

The measured α_{exp} seem to be consistent with the scaling laws derived earlier. A prefactor of order 1 appears, another fact in favor of the geometrical description done in figure 4.8. As we know the expression of α , it can then be replaced in the expression for the elastic energy:

$$\mathcal{E}_{elast3D_{tot}} \sim Et^3 \sqrt{\frac{ew}{dL^3}} (d - X) \quad (4.14)$$

When the rectangles are totally closed, $X = 0$. If the closing is due to surface tension, the following equation is verified:

$$Et^3 \sqrt{\frac{ew}{dL^3}} d \sim \gamma dL \quad (4.15)$$

so that:

$$\frac{Et^3}{\gamma} \sqrt{\frac{ew}{dL^5}} \sim c^{st} \quad (4.16)$$

We define here another non dimensional number $A_{3D} = \frac{1}{\Gamma_{3D}} = \frac{Et^3}{\gamma} \sqrt{\frac{ew}{dL^5}}$, when the cells are closed in 3D, $A_{3D} = c^{st}$. Small variations in L induce large change in this parameter.

4.2.1.c Phase diagram and soap experiments

Thus for both the 3D and 2D deformation cases, we calculated the energies involved in the closure of the cells. It has been shown that in the case of 2D deformation, the cells always deform, however the separation with the case of 3D deformation has not been explained yet.

Sculpting soap films

When the cells are almost totally closed, $X \sim 0$, they remain in plane if:

$$\mathcal{E}_{elast2D}(X \sim 0) < \mathcal{E}_{elast3D_{tot}}(X \sim 0) \quad (4.17)$$

so:

$$e^5 d^3 < L^3 w t^4 \quad \text{or} \quad A_{2D} < A_{3D} \quad (4.18)$$

For any other X , the limit between 2D and 3D deformations can be seen as an instability reminiscent of lateral torsional buckling [108]. The bending energy in 2D scales like $(d - X)^2$ whereas the bending energy for the 3D deformations scales like $(d - X)$. Thus for small deflections $(d - X)$, the 2D bending energy is smaller whereas at large deflection $(d - X)$, the elastic bending energy of the 3D mode more favorable (figure 4.11 left). Thus for a critical value of the deflection $(d - X)_b$, found when $\mathcal{E}_{elast2D} = \mathcal{E}_{elast3D}$, the system chooses to buckle out of plane:

$$Et^3 \sqrt{\frac{ew}{dL^3}} (d - X)_b \sim \frac{Ee^3 t}{L^3} (d - X)_b^2 \quad (4.19)$$

so :

$$(d - X)_b \sim t^2 \sqrt{\frac{L^3 w}{e^5 d}} \quad (4.20)$$

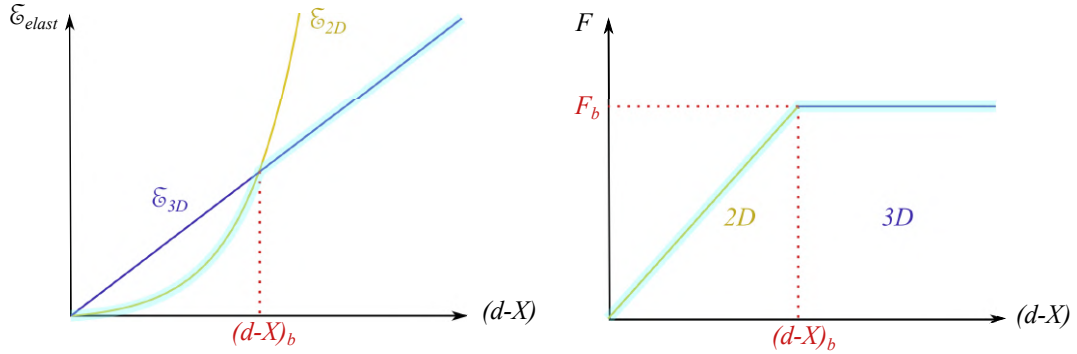


Figure 4.11 Elastic energy as a function of the deflection (left). The 2D elastic energy is quadratic whereas the 3D one is linear with $(d - X)$. On the right, the force needed to induce a deflection $(d - X)$.

Knowing the elastic energy of the system as a function of deflection (figure 4.11, left), it is possible to calculate the force needed to achieve a given deflection (figure 4.11, right):

$$F \sim \frac{\partial \mathcal{E}_{elast}}{\partial (d - X)} \quad (4.21)$$

It is thus possible to know the force needed for the sample to buckle in 3D:

$$F_b \sim Et^3 \sqrt{\frac{ew}{dL^3}} \quad (4.22)$$

In our system, the force considered is the surface tension γL . If $\gamma L < F_b$, this model predicts deformations in the plane, with a deflection $(d - X) \sim \frac{d}{A_{2D}}$ that leads to complete closure when $A_{2D} \sim 1$. If $\gamma L = F_b$, then the model predicts buckling in 3D, and in fact very large deflection (up to closure).

With all these conditions on the geometrical parameters, it is convenient to draw a phase diagram to summarize the different results of the experiments. We will use the two non dimensional numbers defined earlier:

$$A_{3D} = \frac{\mathcal{E}_{elast3D}}{\mathcal{E}_{soap}} = \frac{Et^3}{\gamma} \sqrt{\frac{ew}{dL^5}} \quad (4.23)$$

$$A_{2D} = \frac{\mathcal{E}_{elast2D}}{\mathcal{E}_{soap}} \Big|_{contact} = \frac{Ee^3td}{\gamma L^4} \quad (4.24)$$

In figure 4.12, we represent the expected phase diagram in the $A_{2D} - A_{3D}$ plane. The full vertical line represents the separation between the networks with cells partially and totally closed in the 2D mode. The full horizontal line corresponds to the separation between the networks partially closed in 2D and closed in 3D. The region with stripes represents the region where the cells are expected to fully close.

In scaling law there is no difference between condition to be fully closed in 3D and the transition between partial closing in 2D and 3D. The separation has to be checked experimentally.

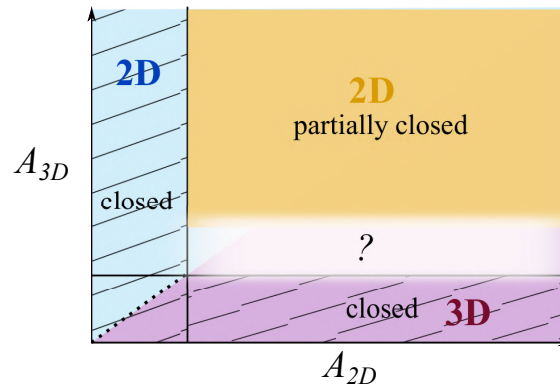


Figure 4.12 Theoretical phase diagram of the rectangular cells. The $A_{2D} - A_{3D}$ plane is divided in three zones: one where the rectangles totally close in plane (2D, blue), one where they totally close out of plane (3D, purple) and a region where the cell are partially closed in plane (2D, yellow). The region with stripes represent the region where the cells are expected to fully close.

To check the theoretical predictions, experiments are performed with many different networks. First networks are cut off Mylar sheets with $t = 30 \mu\text{m}$, varying the distances d , L , e and w . Later the same experiments are performed with thicker Mylar networks (different symbols in figure 4.14) or with networks of different materials (different Young modulus E : PLA, TPU, Filaflex (elastic filament)). The

Sculpting soap films

networks are dipped in a soap solution (glycerol, water and Fairy® dish washing liquid) and are hung by hands vertically. The observation of the different behaviors is done by eyes.

In order to obtain shapes that close and that are easily handable when put in soap, the networks cells are much smaller than in the study of the angle α (cells with $L \sim 1\text{cm}$ instead of 10cm).

All points are collected in a phase diagram in the $A_{2D} - A_{3D}$ plane in figure 4.14. Five different behaviors can be observed: in blue the in-plane deformation, in light blue the total 2D closing, in dark blue the partial 2D closing; in purple the 3D deformation, in light purple the total 3D closing, dark purple the 3D partial closing. Finally in yellow, the points for the networks that do not deform with soap.

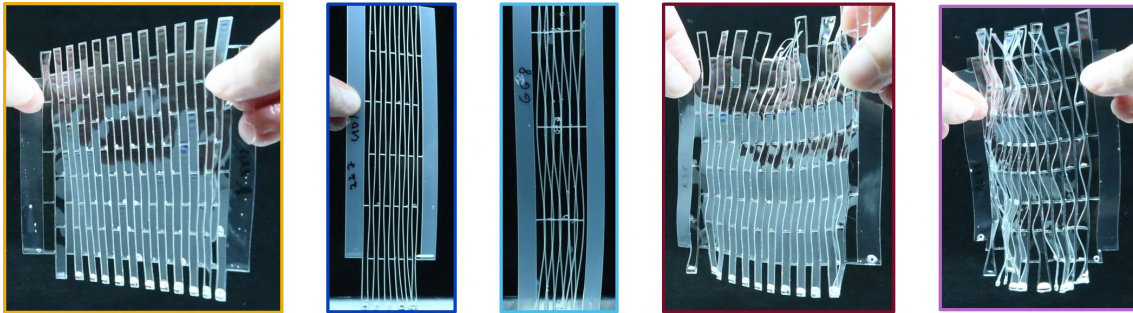


Figure 4.13 Examples of networks present in the three zones. On the left (yellow frame) a network that does not deform, in the center (blue frames) networks that close in 2D, on the right (purple frames) networks that undergo 3D deformations. The colors correspond to the ones in the diagram figure 4.14.

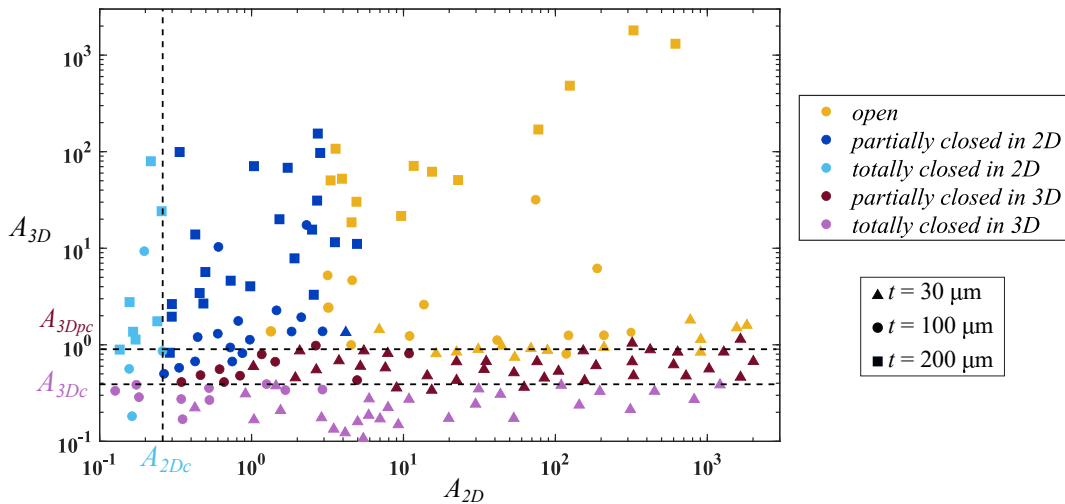


Figure 4.14 Phase diagram of the rectangles networks in the $A_{2D} - A_{3D}$ plane. The colors represent the 5 different cases observed: in blue the deformations in 2D and in purple the deformations in 3D. The light colors represent cells that totally close and the dark the cells that partially close. The yellow points correspond to networks that do not seem to close. The symbol shapes corresponds to different Mylar thicknesses. Lines are drawn for $A_{3D} = 0.39$ and 0.85 and $A_{2D} = 0.26$.

According to the equation derived earlier, the limits between networks that are totally closed and the others are horizontal in the case of the 3D deformations and vertical in the case of the planar one. This behavior is indeed observed in the phase diagram (figure 4.14). The equations only allows to determine scaling laws, the position of the vertical and horizontal lines are drawn experimentally by finding the limit between the networks that are partially and totally closed. Experimentally, the area where the cells are totally closed is relatively small as the networks fold into themselves and become a ball when $A_{2D} < A_{2Dc} = 0.26$ or $A_{3D} < A_{3Dc} = 0.39$.

Doing the experiment it appears that the cells can partially close in both modes. In the case of in-plane deformation, the limit observed seems to be limited by eye resolution. If the deflection is very small, the networks appear as open. In the case of the deformation in 3D, two limits can be clearly observed: $A_{3D} = A_{3Dc} = 0.39$ and $A_{3D} = A_{3Dpc} = 0.85$ (separation between the different phases). Using only scaling laws, the theory predicts that there is only one limit and that the cells should go from partially closed in 2D to totally closed in 3D but it is not the case experimentally. This might be due to the fact that many terms are neglected in the energy estimate.

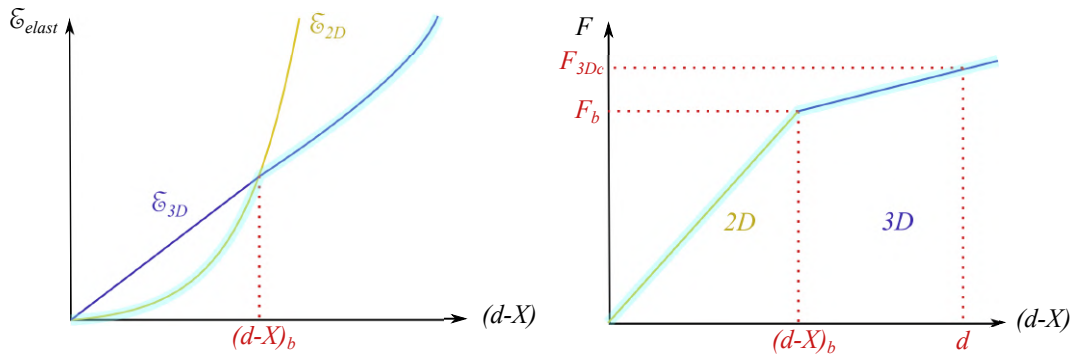


Figure 4.15 Schematic elastic energy as a function of the deflection (left). The energy due to 3D deformations is approximated at the second order in $(d - X)$. On the right the force needed to have a deflection of $(d - X)$ and the position of the transition 2D-3D and the total closure in 3D.

If the bending energy in the case of 3D deformations is not a linear function of $(d - X)$ but has higher order terms, the forces needed to partially and totally close in 3D are different (figure 4.15). The calculation done earlier were not precise enough to capture this details. Moreover in the experiments, it seems that the separation between 3D et 2D for $A_{3D} = A_{2D}$ seems to be true for values of X higher than zero.

Finally, the diagram can be summarized as figure 4.16.

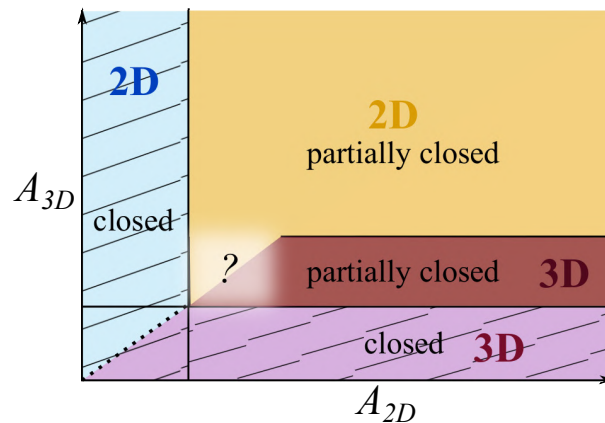


Figure 4.16 Theoretical phase diagram of figure 4.12 filled with a new frontier that put the limit between the state partially open in the 2D and 3D case. The dark purple part corresponds to the rectangle partially closed in 3D.

4.3 Deploying 3D structures

Soap films can only adopt zero and negative Gaussian curvature due to pressure equilibrium. Since then, obtain shape with positive Gaussian curvature with soap seems to be a challenge.

In the previous section we have calibrated the new system of actuation with surface tension to close cells. As we now know how much a cell closes as a function of its geometrical parameters and the surface tension, it becomes possible to design 3D shapes. As in the previous chapter 3, by orienting differently the rectangles in space it is possible to program 3D shapes. Rectangle cells close according to their width d . If the rectangles are shifted by half their length, the network shrinks by a factor 2 on average.

We mostly programmed axisymmetric metric distortions obtained from networks designed in cylindrical coordinates. The observation and characterization of 3D shapes is a challenge since soap films are very fragile and have a limited lifetime about ten seconds. The networks are dipped into soapy water and then hung from the center, and then from one edge. If the soap film is thick, its weight is not always negligible, and the shape observed are thus influenced by the gravity. To estimate this effect, we also take pictures of the samples when they are hung from the edge. We also take picture of the dry network as a comparison to evidence the shaping role of the surface tension.

4.3.1 Aligned rectangles on a disk

As seen earlier 3, a simple way to obtain 3D shapes is to program negative strain in the radial or orthoradial direction only. To impose such strain patterns, we use rectangles that are elongated in the radial direction or in the orthoradial direction. However, this requires geometrical adjustments of the unit pattern.

4.3.1.a Cells elongated along the radial direction

When the cells are elongated in the radial direction, they must take trapezoid shape (the smaller side being close to the center of the circle) to tile the disk (figure 4.17). We wish to obtain a shape with constant programmed strain with the cells closing the same amount everywhere. It is thus important to choose rectangles that belong to the closed zone or next to the limits in the phase diagram (figure ??). The length e and w of the network are fixed, the width d is fixed by the number of rectangle on a ring and the distance to the center. The length L of the cells is chosen in order for the cells to close under surface tension forces. When cells become too large far from the center of the samples, they are divided into 3 rectangles in order to maintain a smooth deformations (cells with roughly the same size).

The mean width d_{mean} of a rectangle depends on the length of the rectangle L . Rectangles are drawn from the center to the edge, ring by ring. d_{mean} corresponds to d_{i+1} in the figure 4.17. To make sure that all the cells close in a similar way, we keep the coefficient A_{3D} constant (in order to stay in 3D closing). The following equation has then to be obeyed:

$$A_{3D} = \frac{Et^3}{\gamma} \sqrt{\frac{ew}{d_{mean}L^5}} = c^{st} \tag{4.25}$$

For the ring i , $d_{mean} = d_{i+1} = \frac{2\pi}{N}(R_i + \frac{L}{2})$, with R_i the radius at the base of the rectangles and L the height of the rectangle and N the number of rectangle per ring (figure 4.17). Thus:

$$A_{3D} = \frac{Et^3}{\gamma} \sqrt{\frac{ew}{\frac{2\pi}{N}(R_i + \frac{L}{2})L^5}} \tag{4.26}$$

so L has to be solution of:

$$L^6 + 2R_iL^5 = \frac{NE^2t^6ew}{\pi\gamma^2A_{3D}^2} \tag{4.27}$$

The value of A_{3D} is varied upon experiment to change the closing of the cells.

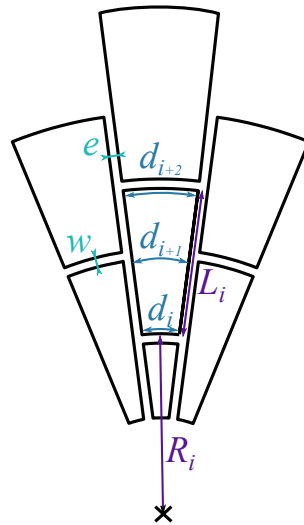


Figure 4.17 Part of a network designed to produce cones when activated by soap films. Rectangular cells close along the orthoradial direction

Equation 4.27 is solved at each step by Matlab in the algorithm that draws the networks. The single positive solution at each i gives the position of the next ring of rectangle. From one ring to the next, rectangles are shifted to observe the same configuration as in the case of aligned rectangles. Keeping A_{3D} truly constant is not convenient to have rectangles that are exactly shifted by half a length along a radius, as their length is dictated by equation 4.27 it changes from a ring to the next one.

If such network is dipped in a soap solution and that the cells are totally closed, the radial strain is zero whereas the strain contraction in the orthoradial direction is around 0.5. Due to this metric change, the sample should go out of plane and a conical shape should emerge.

In our experiments, the dry network is first hung by a wire in its center. It is dipped into soapy water together with a circular annulus. When it is pulled off, a planar film is supported by the annulus (first picture of figure 4.18). When the soap film outside the structure burst, the final 3D shape appears (second picture of figure 4.18). Finally when all the films inside the rectangles are broken, we recover the initial network (third picture of figure 4.18). While gravity appears to induce limited sagging of the structure, the effect of soap films dominates the programmed 3D-shape of the network.



Figure 4.18 Network with radially elongated cells shrunk by soap films. On the left, the design then the network before, after being deformed by the soaps films, and finally the shape when all soap films burst.

For each network a value of A_{3D} is chosen and gives different results. The cells does not close by the same amount when A_{3D} is changed. We expect the angle of the cone to be different for each sample with different A_{3D} . However as the deformation is not smooth and since the cells tend to deform in 3D, it is difficult to measure the angles of the cones. Due to the 3D deformation of the cells, depending on the view angle, the observed 3D shapes are different that is why two pictures of the same cones are taken (figure 4.19).

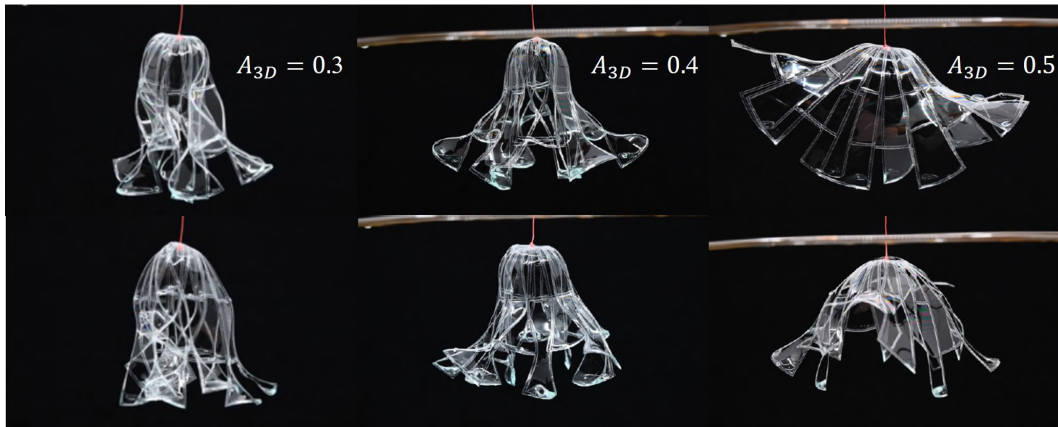


Figure 4.19 Network of radially elongated cells with different values of the elasto-capillary number A_{3D} . The top and bottom pictures are taken at 90° . Positive Gaussian curvature appears.

Qualitatively, we can see that when the value of A_{3D} is decreased, the cells close more and the angle of the cone is thus lower (figure 4.19).

4.3.1.b Rectangles elongated in the orthoradial direction

When the rectangles are elongated in the orthoradial direction, they are curved in order to pave the disk (figure 4.20). The closer they are to the center, the higher is their curvature. However if the rectangle are small enough ($L \ll R$) they can be considered as “straight” rectangles. We will first consider that this condition is satisfied. In a second part, we will study the influence of curvature on the closure of the cells later in section 4.3.3.

We choose to keep the lengths e and w constant throughout a given sample. Fixing the number of rectangles per ring sets the length L of the rectangles. The width d is then chosen for each ring in order for the rectangle to be in a configuration where they totally close. As in the previous case, the cells within a given sample are designed to have the same A_{3D} . This number is changed from a sample to another: the lower A_{3D} , the higher is the negative strain of the cells.

In order to keep the number A_{3D} constant for the rectangle of each ring, the same equation as in section 4.3.1.a has to be imposed of each cell:

$$A_{3D} = \frac{Et^3}{\gamma} \sqrt{\frac{ew}{dL_m^5}} \quad (4.28)$$

looking at ring i , we define $L_{m_i} = \frac{2\pi}{N} \left(R_i + \frac{d_i}{2} \right)$ as the length at the center of the rectangle, R_i the radius at the base of the rectangle, d_i the height of the rectangle and N the number of rectangle per ring (figure 4.20). The height d_i is then expressed as $d_i = 2 \left(\frac{N}{2\pi} L_{m_i} - R_i \right)$. Thus:

$$A_{3D} = \frac{Et^3}{\gamma} \sqrt{\frac{ew}{2 \left(\frac{N}{2\pi} L_{m_i} - R_i \right) L_{m_i}^5}} \quad (4.29)$$

so that L_{m_i} is solution of:

$$L_{m_i}^6 - \frac{2\pi R_i}{N} L_{m_i}^5 = \frac{\pi E^2 t^6 ew}{N \gamma^2 A_{3D}^2} \quad (4.30)$$

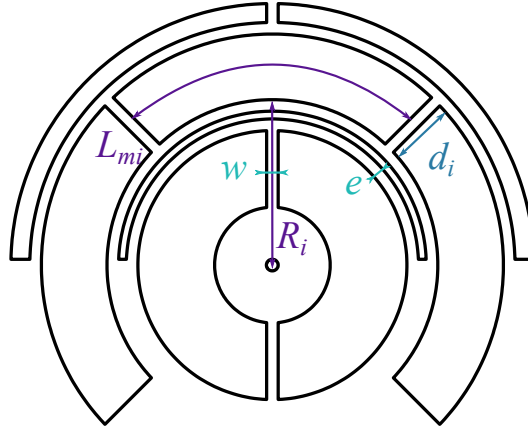


Figure 4.20 Part of a network designed to produce an e-cone shape when covered with soap films.

As in section 4.3.1.a, equation 4.30 is solved by Matlab and the positive solution is retained. To avoid too large rectangles, a maximal value of d_i is set, around 1cm in our experiments. When this criteria is met, there are two options. The first option is to multiply the number of rectangles by two. The new rectangles are exactly shifted of half a length from one ring to the next one. However the length L_{m_i} is divided by two and the aspect ratio is then very different. The second option consists in adding only a finite number of rectangle to the ring (most of the time 2). Doing so, the new rectangles are not exactly shifted by half a length, but the change in L_{m_i} is smoother. We retain this option in the experiments.

When soap films are added to the rectangles that are oriented perdicularly to the radii, there is a contraction strain in the radial direction, whereas the length of the perimeters remains constant. The resulting relative excess of length on the edge should lead to the emergence of a saddle shape (figure 4.21).



Figure 4.21 Network with orthoradial cells with soap film. From left to right: the design, the shape before and after being deformed by the soap and the shape when all the soap films have disappeared.

As in the previous section 4.3.1.a, the number A_{3D} can be modified from one sample to another. The curvature of the saddle increases when the number A_{3D} decreases (figure 4.22). As in the previous section it is difficult to characterize the 3D shapes quantitatively. If A_{3D} is too low, it is more difficult to get a controlled shape and the network often ends up as a ball of wool.

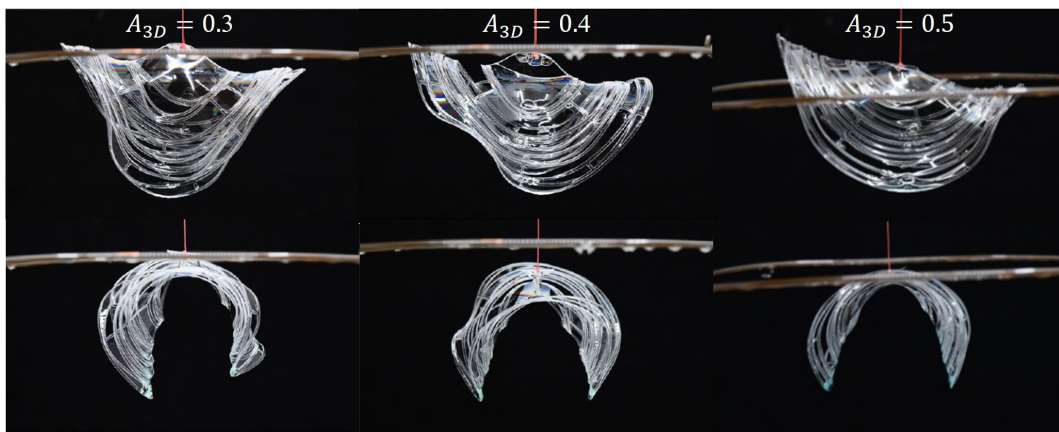


Figure 4.22 Network of orthoradially elongated cells with different number A_{3D} covered with soap film. The top and bottom rows display pictures of the same sample taken at 90° . A negative Gaussian curvature appears.

Thus we show how to obtain 3D shapes out of a 2D axisymmetric networks covered with soap films. Here we focused on two different directions of shrinking. However using logarithmic spirals as in chapter 2 and 3, it is possible to obtain all the range of negative strain direction from orthoradial (90°) to radial (0°) direction giving access to a larger variety of shapes.

4.3.2 Logarithmic spirals

In this section we will consider the logarithmic spirals defined in chapter 3. An even number of spirals of the same pitch angle are drawn, separated by an equal angular distance. We define a section of the spiral as the area delimited by two consecutive spirals (white or blue in figure 4.23). Each section is then divided in rectangles using perpendicular spirals. As in all other networks of rectangles, the

Sculpting soap films

rectangles have to be shifted of half their length from a spiral section to the next. In addition, as before we keep the number A_{3D} constant.

As drawing logarithmic spirals is more complicated than the more symmetric networks drawn in the previous section 4.3.1, we do not have an explicit way of solving the dimensions of the rectangles to give a constant A_{3D} . The width d_{mean} is difficult to approximate as a function of the radius R_i and the length L_i . To simplify the problem, L_i is calculated with the bottom width d_b , the value at the mean d_m is then measured with such L_i and a new L'_i is calculated from this new d_m (figure 4.23) by using the equation $A_{3D} = c^{st}$. It is a sort of iterative process with only two iterations to obtain a value of L_i that is more precise.

As the length of the rectangles satisfy the equation $A_{3D} = c^{st}$, it is then difficult to shift them by half a length from one section to the next. In the experiments, the shifting is done manually. The top width d_t of the first rectangle from the center is not taken at the same position (distance from the center) for even and uneven section of spiral (white and blue sections in figure 4.23). The position of the top first rectangle of the uneven section is chosen as a fraction of the length of the first rectangle of the even portion. This number changes when the spiral angle β changes. It ranges from 0.5 to 1. The rectangles are perfectly shifted only in the case of $\beta = 90^\circ$ or $\beta = 0^\circ$ that corresponds to the two purely orthoradial and radial limit regimes presented in the previous section.

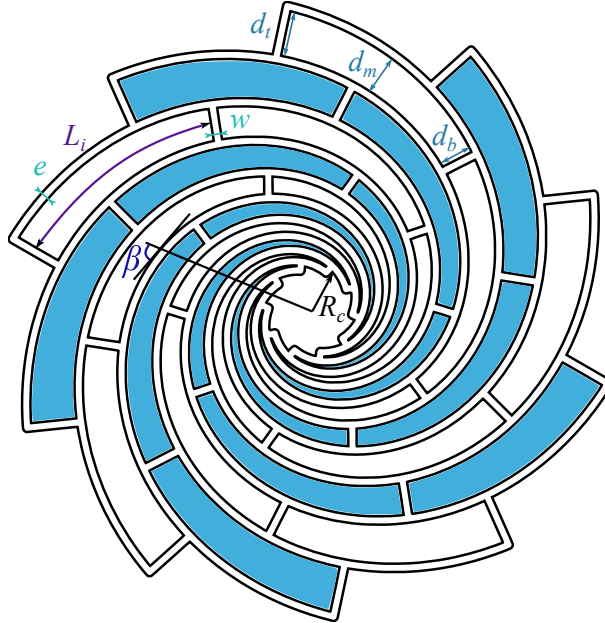


Figure 4.23 Spiral network with $\beta = \frac{\pi}{2.5}$, $R_c = 5\text{mm}$ (starting radius of the spirals), $N = 10$, $e = w = 1\text{mm}$ and $A_{3D} = 2$ (the value γ is considered constant in the experiments $\gamma = 25.10^{-3}\text{N.m}^{-1}$ and $t = 30\mu\text{m}$).

By changing the angle β of the spirals, it is possible to obtain a continuous family of shapes from cones to anti-cones. It is also possible to change the value of A_{3D} to change the amount of closure of the cells. The phase diagram (figure 4.14) gives an approximation of the value of A_{3D} that have to be taken but in order to find the best one for the experiments, three different values of A_{3D} are tested for a sample

with $\beta = \frac{\pi}{10}$ (figure 4.24). We select the samples that deform with surface tension but do not fold too much onto themselves when dipped into soap. With this networks, different conical shapes are obtained.

We choose the central one to be the best, in the following the A_{3D} chosen is thus 0.4 because for $A_{3D} = 0.3$, the cells have the tendency to fold onto themselves with the soap and for $A_{3D} = 0.5$ the closing is too small. On the top of figure 4.24, the networks look similar but the length of the rectangles slightly change from one sample to another that lead to shapes that look very different. This shows that the size of the cells have to be taken carefully in order to get precise shapes.

For a given number $A_{3D} = 0.4$, the angle β of the spirals is changed from $\frac{\pi}{2.5}$ to $\frac{\pi}{10}$, in order to keep approximately the same size of rectangles between the sample, the number N is increased when the angle get smaller. N goes from 10 to 20 (figure 4.25, top). When the angle β is close to $\frac{\pi}{2}$, a shape of an e cone appears, on the contrary if β is close to zero, a cone appears.

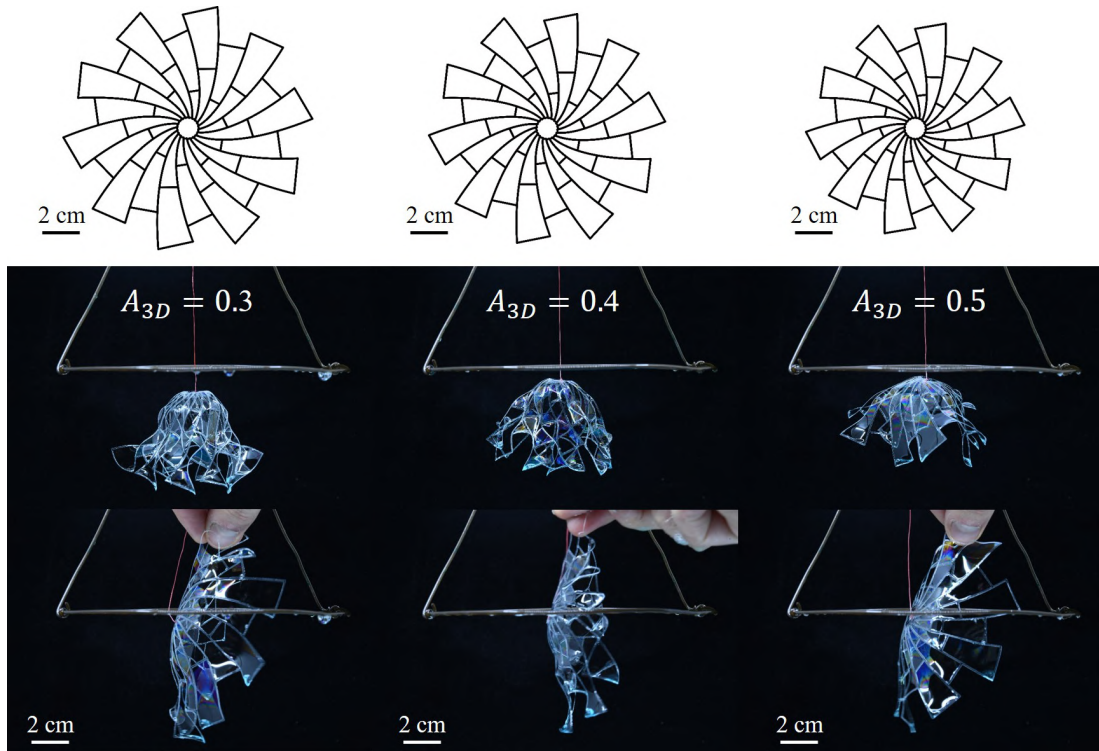


Figure 4.24 Spiral network in soapy water with $\beta = \frac{\pi}{10}$, $R_c = 5\text{mm}$, $N = 20$, $e = w = 1\text{mm}$ with different closing number A_{3D} .

The closing of the cells occurs perpendicularly to the spirals. There is a mismatch in the plane if the radial and orthoradial strains are different. In the the case of the rectangle elongated purely radially or orthoradially, one strain is negative and the other zero. In the configuration of spirals, as the cells close perpendicularly to the spirals, the negative strain has a radial and orthoradial components [77].

If the radial contraction strain component is higher than the orthoradial one, the final shape should have a positive Gaussian curvature and look like a cone (figure 4.25 $\beta = \frac{\pi}{5}$ and $\frac{\pi}{10}$). Conversely, if the

Sculpting soap films

radial contraction strain component is lower than the orthoradial one, a shape with a negative Gaussian curvature should appear (figure 4.25, $\beta = \frac{\pi}{2.5}$ and $\frac{\pi}{3}$). Following this reasoning at $\beta = \frac{\pi}{4}$ or close to this angle, the network should only shrink in plane. However in our case (figure 4.25, when the angle β is close to $\frac{\pi}{4}$, the deformation is not totally in plane. According to Siefert *et al.* [77], the exact angle that gives a deformation that is only in plane is $\beta_c = \frac{\pi}{2} - \arcsin \frac{1}{\sqrt{1+\lambda}}$ with λ the contraction perpendicularly to the spirals. This angle is different from $\frac{\pi}{4}$ because it takes into account the final direction of the spirals that is different from the beginning.

In our case, λ is 0.5 at most, taking this value $\beta_c \sim 0.6 \sim \frac{\pi}{5}$. Thus the angle that lead on only in plane deformation should be around $\beta_c \sim \frac{\pi}{5}$. However in the experiments, it seems that at $\beta = \frac{\pi}{5}$ and $\beta = \frac{\pi}{4.05}$, the shapes obtained have positive Gaussian curvature. It might be due to the gravity that is not taken into account and that could influence the shape or that the rectangles are not exactly shifted by half a length or lastly that the wall width of the cells plays a role.

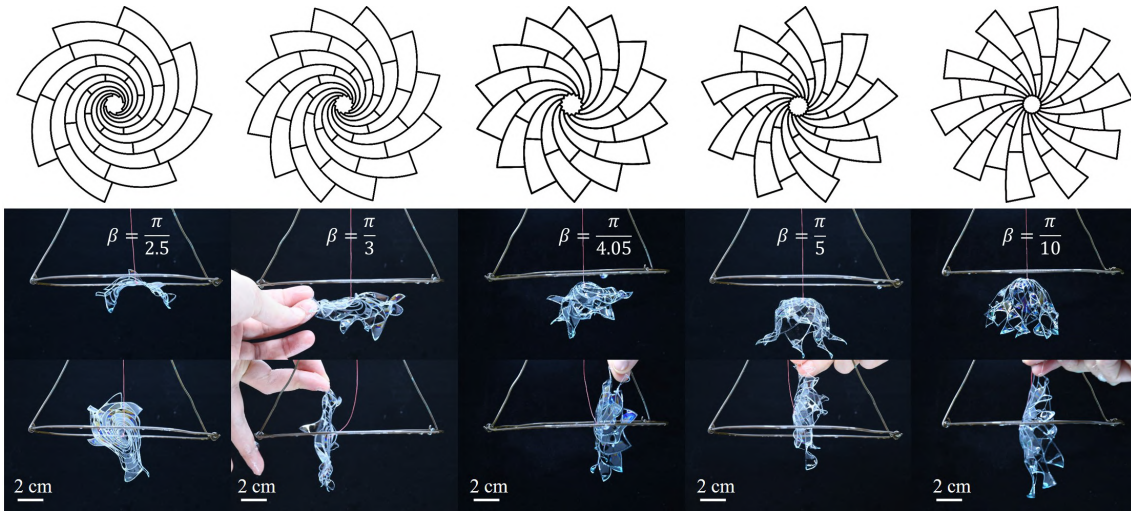


Figure 4.25 Spiral network in soapy water with $A_{3D} = 0.4$, $R_i = 5\text{mm}$, $e = w = 1\text{mm}$ and various values of β . A continuous family of shapes is obtained.

Observation (and taking pictures) requires care and patience. Setting up the soap film bath is not easy as the cells tend to close onto themselves when taken out of the bath. The final shape depends on the number of rectangles that are actually closed by a soap film. Since the films break easily, pictures have to be taken immediately after the outside film breaks. The final shape can vary for different experiments with the same network. The shape can thus only be characterized qualitatively. We also notice that the shape is not axisymmetric, due to the fact that the tiling of the disk is discrete.

Up to now we have neglected the overall curvature of the rectangular cells. This makes sense if $L \ll R_c$ (with R_c the curvature radius of the cell), a reasonable hypothesis when the angle β is close to zero, but it is not the case when β approaches $\frac{\pi}{2}$. When the rectangles are more elongated along the orthoradial direction the curvature of the cell should play a role in its capillary closing.

4.3.3 Influence of the curvature of “rectangular” cells

When the orientation of the rectangular cells is close to the orthoradial direction, the condition $L \ll R_c$ is no longer respected. When rectangular cells are oriented with an angle β close to $\frac{\pi}{2}$, they do not all close by the same amount when dipped in soap and the total closing does not occur for the predicted A_{3Dc} . In order to better program shapes with a constant strain when activated, the influence of the curvature on the closing of the rectangular cells should be understood.

As drawing a network of aligned curved rectangles is difficult, single rectangular cells with a given curvature are used instead. They are covered with soap films and a phase diagram is realized. In the experiments, the ratio A_{3D} is changed as well as the radius of curvature R_c , the width d and the length of the cell L , the thicknesses e and w are kept constant. The curvature of such cells is then $\kappa \sim \frac{1}{R_c}$. The L and d considered in the study are L_θ and d_r , the radial and orthoradial distances.

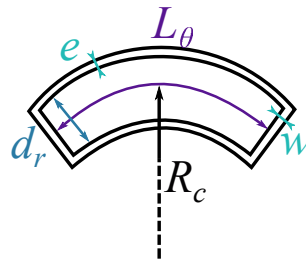


Figure 4.26 Sketch of a unit rectangular cell with a given curvature $\kappa = \frac{1}{R_c}$

As mentioned earlier, when the ratio $L/R_c \sim \kappa L$ is small, the cells should behave as regular rectangles. When the ratio is large, the curvature can no longer be neglected. Thus the axes used for the phase diagram to find the influence of the curvature are the ratio L/R_c and the number elasto-capillary number A_{3D} (figure 4.27).

As in the previous phase diagram, three cases can be observed: totally closed, partially closed and open (truly 2D partially closed). If the curvature was not influencing the closure of the cells, the different phases in the phase diagram should be delimited by horizontal lines. Here we actually observe that the different phases are delimited by a decreasing function. We describe the boundary between the different phases by a function of the form : $A_{3D} = \frac{1}{a_{corr} + b_{corr} \frac{L}{R_c}}$, with a_{corr} and b_{corr} coefficients to be determined. $\frac{1}{a_{corr}}$ correspond to the y-intercept and b_{corr} to the slope.

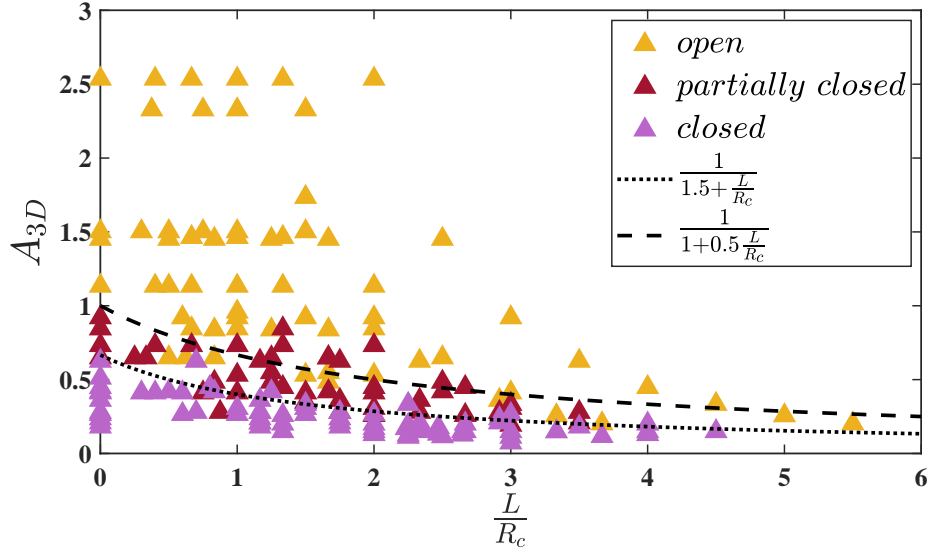


Figure 4.27 Phase diagram of the rectangles as a function in the plane formed by the ratio $\frac{L}{R_c}$ and the elasto-capillary number A_{3D} .

On figure 4.27, two different sets of a_{corr} and b_{corr} are chosen to approximate the boundaries between the different phases. The criterion for uniform actuation strain was:

$$A_{3D} = \frac{Et^3}{\gamma} \sqrt{\frac{ew}{dL^5}} = c^{ste} \quad (4.31)$$

To take the curvature of the cells into account, the new criterion is:

$$\frac{Et^3}{\gamma} \sqrt{\frac{ew}{dL^5}} = \frac{1}{a_{corr} + b_{corr} \frac{L}{R_c}} \quad (4.32)$$

The phase diagram (figure 4.27) gives an interesting indication for an isolated cell but does not exactly describe the actual experiment as the shapes are obtained with networks and not individual cells.

This new correction can be applied both to the spiral with β angles close to $\frac{\pi}{2}$, and to networks with orthoradial cells.

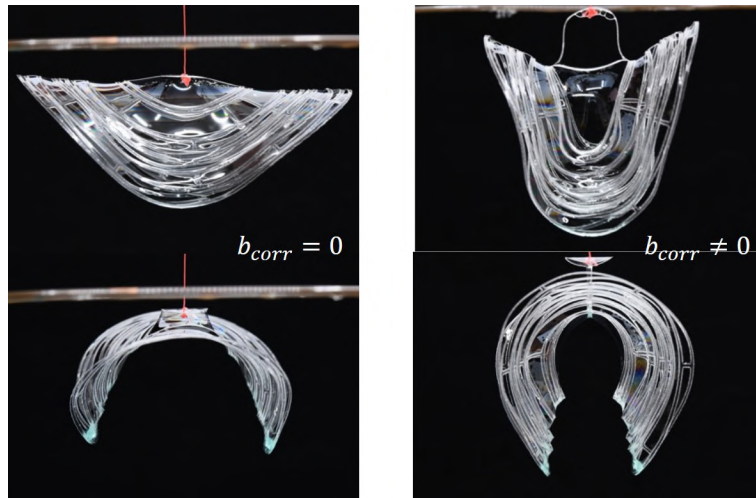


Figure 4.28 Network with orthoradial cells with and without correction (respectively left and right).

In the case of the spirals, instead of considering $\frac{L}{R_c}$ the parameter taken into account is $L\kappa$ thus the new equation to satisfy is :

$$\frac{Et^3}{\gamma} \sqrt{\frac{ew}{dL^5}} = \frac{1}{a_{corr} + b_{corr} \frac{L \sin \beta}{r}} \quad (4.33)$$

with r the radial coordinate of the center of the rectangle and L the curved length ($L = \int dS$ with dS the curvilinear path).

This new correction is used the same way as the A_{3D} number in the spiral case. Equation 4.33 is used with the bottom width d_b to find the length L , with this value L the width at half length d_m can be measured, this d_m is then used in equation 4.33 to determine the final L that will be used in the end.

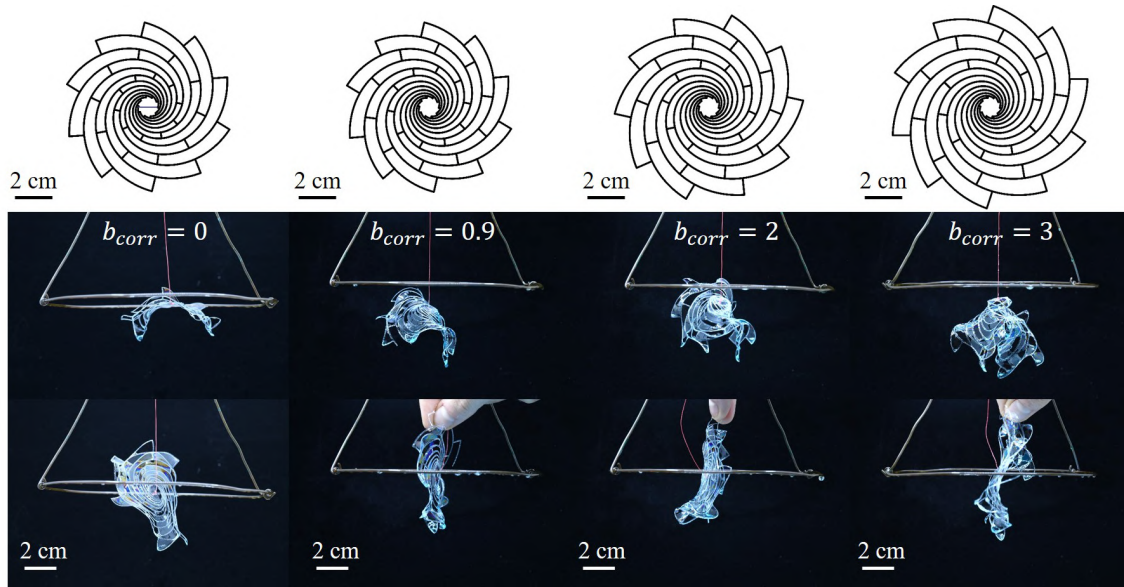


Figure 4.29 Spirals with $\beta = \frac{\pi}{2}$, $N = 10$, $e = w = 1\text{mm}$ and with a correction parameter $a_{corr} = 2.5$ that corresponds to $A_{3D} = 0.4$ when $b_{corr}=0$. The correction parameter b_{corr} is increased from 0 to 3.

For a given correction parameter a_{corr} , the parameter b_{corr} is changed, on the phase diagram it only changes where the curve goes. By increasing the value of b_{corr} , we stay in a part that is more closed. This effect can be seen on figure 4.29, when the correction parameter β is increased, the shape with negative Gaussian curvature seems more and more pronounced.

In conclusion we can experimentally determine parameters that can be used to correct the influence of curvature on the closing of cells. As opposite sides of the rectangles do not have the same length when the cells are curved, it is hard to determine the deformation when the cells close and the exact expression of the energy.

4.4 Other types of cells

So far we exposed how to create shape using rectangular cells. We did not discuss the case of other designs. In the previous section, the cells had large aspect ratio. The case of the square was not predicted by the model. When networks of cells that are almost square are dipped in the soap film, the behavior is different, the phase diagram figure 4.16 is no longer true. Moreover the deformation is also different, in addition to the 2D and 3D mode of deformation, some shear of the cells can be observed.

Another cell that can be tested is the diamond, a recurrent shape in this PhD work. Following the same pattern as for the rectangular cells, a network of shifted diamonds is drawn: from a diagonal to the next, the diamonds are shifted by half their length. Similarly to the squares, the cells experience shear. Indeed, to close, the cells tend to bring opposite sides closer causing shear.

These two other patterns were not used to create shapes as their deformation with soap was not well understood and as closing with shear increases the chance of having cells folding onto themselves.

4.5 Conclusion

We have shown that it is possible to use capillary forces to design 3D objects. By using a cellular network, it is possible to obtain shapes with positive Gaussian curvature whereas soap film can usually only adopt negative or zero Gaussian curvature.

By measuring the degree of closing of the cells as a function of geometrical parameters on simple networks, it appears possible to create more complex networks that deform in 3D. By changing the orientation of rectangular cells, it is possible to obtain shapes from positive to negative Gaussian curvature.

Soap film are ephemeral. Such shapes do not last long, which makes them beautiful but not easy to handle. The study has been done considering soap film as a surface that closes the cells, but surface tension might be replaced by another force. For example, actual cells (biological term) could be put in every holes to pull on the side as the soap film does .



Figure 4.30 Spiral network with $N = 20$, $A_{3D} = 0.4$ and $\beta = \pi/10$.

Conclusion

In this manuscript we have presented several approaches to shape-change, all based on networks of deformable units. These cells, often diamond-shaped, are composed of slender members that bend easily, and therefore have a preferred mode of deformation that is defined by their geometry.

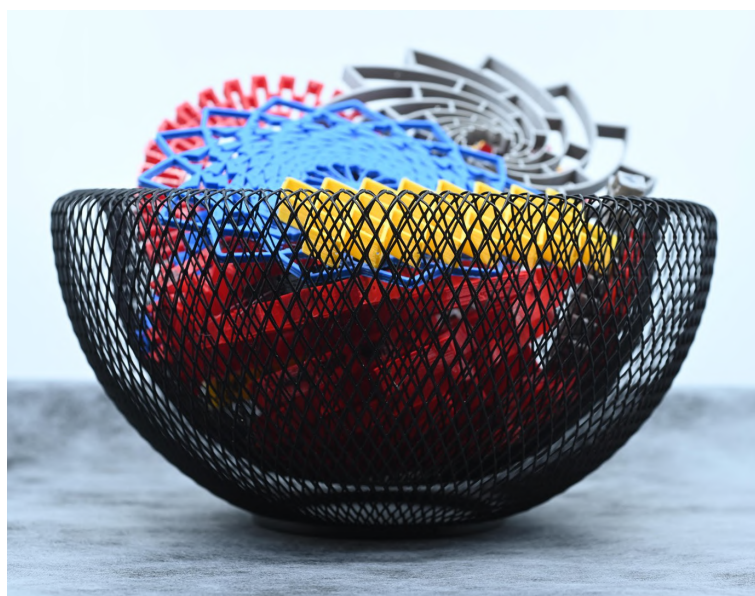


Figure 4.31 Diamond-based deployed basket with many of the samples used in this PhD work

In a first part (chapter 2), we have studied how these cellular structures can be activated when embedded in an active matrix. We used a hybrid material (elastomer matrix + cavities containing alcohol) that undergoes large expansion when heated above the boiling temperature of alcohol. We found that adding a compliant restrictive network (representing a very small mass fraction of the total material) is enough to program large, untethered shape-change, as demonstrated on simple shapes. Such independent active devices are interesting: they directly respond to their environment, from which they extract energy (in this case, heat powers the liquid-gas phase transition, which produces mechanical work), and are not very difficult to produce. In our experiments, the drawbacks were that it is not easy to achieve a fine control of the expansion rate, and that alcohol eventually leaks out of the matrix. However this idea could be interesting at small scales (using another swelling matrix, such as a responsive

Sculpting soap films

hydrogel) as a microscopic grabber or manipulator, capable for example to mechanically probe living cell tissue.

In a second part (chapter 3), we have studied the mechanical deformation of 3D-printed networks and the mode of deformation of each cells. When they are not homogeneously distributed in the plane, their in-plane deformation leads to 3D shapes. We showed how to activate these structures, either directly through wires (and in this case the programmable contraction can be used to program complex shapes), or by vacuum. These techniques are promising as it should be possible to scale them up (we studied their stiffness).

In a third part (chapter 4), we showed how surface tension could also be used as an activation mechanism on our networks. We showed that when a soap film is laid across the network, two modes of closing can occur: in plane, or out-of-plane when a buckling threshold is reached. We characterized the condition for capillary closing, and showed how it also leads to 3D shapes. Even though soap films always present a negative Gaussian curvature, we showed how to sculpt soap film surfaces with a global Gaussian curvature that can be either negative or positive.

Throughout this work, we have therefore seen how an internal structure that restrains or guides the deformation can be used to control the local in-plane strain. We have made extensive use of the powerful and beautiful geometry obtained from a family of intersecting logarithmic (scale-free) spirals to provide a diamond tiling of the plane with almost axisymmetric properties. Because the local deformation depends on the geometry of the unit element, we were able to program a spatial distribution of deformation. In each case, we found that the resulting object spontaneously buckles into a 3D shape. We were able to program simple shapes (cones or e-cones) and sometimes more advanced geometries.

We made the initial observation that there are hardly any applications of shape-changing materials. We think that combining a powerful but featureless actuation mechanism to an internal structure that orients and guide the deformation could help overcome the limitations of many shape-changing devices: the manufacturing is not technically complex, and the stiffness can be much larger. However, many questions remain open, that are common to the three studies and hinder the potential of these systems. First, we note that it is not easy to infer the final 3D surface from a simple look at the network pattern. For example, spiraling patterns leading to positive and negatively curved shape may look quite similar to the untrained eye. It is even more difficult to solve the inverse question: what pattern should we produce to obtain a specific 3D surface? We did not go very deep into this inverse problem, and this is clearly a very important next step.

A natural extension of this work would be to consider networks initially drawn along a non-flat surface. That is to say: can we imagine a shell morphing into another shell? The design, the inverse problem and the practical fabrication will all be more complex, but we expect the principle to hold. In the same line, it would be important for the reliability of the process to program not only the distances compatible with a new 3D surface, but also the curvature, ensuring that the system does not evolve towards an isometry of the target shape.

Another problem which should be discussed is the prediction of the mechanical properties of the 3D

objects when activated. It should be possible to infer them from the stretching and bending stiffness of uniform patterns, but the task is made more difficult by the strong anisotropic properties that they exhibit. In particular, in the case of wire activation, we expect the 3D structure to become stiffer. Such stiffening effect would be very promising for applications, and it would be very interesting to devise and characterize other strategies capable of stiffening the structure once deployed.

Advances in these open questions require the blending of different disciplines: computational design, physics, digital fabrication, mechanics, geometry, physico-chemistry, robotics, computer graphics. The fact that these domains are currently starting to connect is an encouraging sign for more interesting developments in the future.

References

- [1] Trevor J Jones, Etienne Jambon-Puillet, Joel Marthelot, and P-T Brun. Bubble casting soft robotics. *Nature*, 599(7884):229–233, 2021.
- [2] Changjin Huang, Zilu Wang, David Quinn, Subra Suresh, and K. Jimmy Hsia. Differential growth and shape formation in plant organs. *Proceedings of the National Academy of Sciences*, 115(49):12359–12364, 2018.
- [3] Taylor H Ware, Michael E McConney, Jeong Jae Wie, Vincent P Tondiglia, and Timothy J White. Voxelated liquid crystal elastomers. *Science*, 347(6225):982–984, 2015.
- [4] Gary P. T. Choi, Levi H. Dudte, and L. Mahadevan. Programming shape using kirigami tessellations. *Nature Materials*, 18(9):999–1004, 2019.
- [5] George M. Whitesides. Soft robotics. *Angewandte Chemie International Edition*, 57(16):4258–4273, 2018.
- [6] Kaushik Bhattacharya and Richard D. James. The material is the machine. *Science*, 307(5706):53–54, 2005.
- [7] Robert F Shepherd, Filip Ilievski, Wonjae Choi, Stephen A Morin, Adam A Stokes, Aaron D Mazzeo, Xin Chen, Michael Wang, and George M Whitesides. Multigait soft robot. *Proceedings of the national academy of sciences*, 108(51):20400–20403, 2011.
- [8] Filip Ilievski, Aaron D Mazzeo, Robert F Shepherd, Xin Chen, and George M Whitesides. Soft robotics for chemists. *Angewandte Chemie*, 123(8):1930–1935, 2011.
- [9] Martin Michael Müller, Martine Ben Amar, and Jemal Guven. Conical defects in growing sheets. *Physical review letters*, 101(15):156104, 2008.
- [10] Vincent Mirabet, Pradeep Das, Arezki Boudaoud, and Olivier Hamant. The role of mechanical forces in plant morphogenesis. *Annual review of plant biology*, 62(1):365–385, 2011.
- [11] Renate Sachse, Anna Westermeier, Max Mylo, Joey Nadasdi, Manfred Bischoff, Thomas Speck, and Simon Poppinga. Snapping mechanics of the venus flytrap. *Proceedings of the National Academy of Sciences*, 117(27):16035–16042, 2020.
- [12] Enrico Coen, Anne-Gaëlle Rolland-Lagan, Mark Matthews, J. Andrew Bangham, and Przemyslaw Prusinkiewicz. The genetics of geometry. *Proceedings of the National Academy of Sciences*, 101(14):4728–4735, 2004.
- [13] Yoël Forterre, Jan M. Skotheim, Jacques Dumais, and L. Mahadevan. How the venus flytrap snaps. *Nature*, 433(7024):421–425, 2005.
- [14] Eran Sharon, Benoît Roman, Michael Marder, Gyu-Seung Shin, and Harry L Swinney. Buckling cascades in free sheets. *Nature*, 419(6907):579–579, 2002.

References

- [15] Hillel Aharoni, Yu Xia, Xinyue Zhang, Randall D Kamien, and Shu Yang. Universal inverse design of surfaces with thin nematic elastomer sheets. *Proceedings of the National Academy of Sciences*, 115(28):7206–7211, 2018.
- [16] Qi Ge, Amir Hosein Sakhaei, Howon Lee, Conner K Dunn, Nicholas X Fang, and Martin L Dunn. Multimaterial 4d printing with tailorable shape memory polymers. *Scientific reports*, 6(1):1–11, 2016.
- [17] Ehsan Hajjiesmaili, Eesha Khare, Alex Chortos, Jennifer Lewis, and David R Clarke. Voltage-controlled morphing of dielectric elastomer circular sheets into conical surfaces. *Extreme Mechanics Letters*, 30:100504, 2019.
- [18] Hadrien Bense, Miguel Trejo, Etienne Reyssat, José Bico, and Benoît Roman. Buckling of elastomer sheets under non-uniform electro-actuation. *Soft matter*, 13(15):2876–2885, 2017.
- [19] Bastiaan Florijn, Corentin Coulais, and Martin van Hecke. Programmable mechanical metamaterials. *Physical review letters*, 113(17):175503, 2014.
- [20] Farhang Momeni, Seyed M.Mehdi Hassani.N, Xun Liu, and Jun Ni. A review of 4d printing. *Materials Design*, 122:42–79, 2017.
- [21] Stephen Timoshenko. Analysis of bi-metal thermostats. *Josa*, 11(3):233–255, 1925.
- [22] Aslan Miriyev, Kenneth Stack, and Hod Lipson. Soft material for soft actuators. *Nature Communications*, 8(1):596, 2017.
- [23] Etienne Reyssat and Lakshminarayanan Mahadevan. Hygromorphs: from pine cones to biomimetic bilayers. *Journal of the Royal Society Interface*, 6(39):951–957, 2009.
- [24] Achim Menges and Steffen Reichert. Performative wood: physically programming the responsive architecture of the hygroscope and hygroskin projects. *Architectural Design*, 85(5):66–73, 2015.
- [25] Tiffany Cheng, Marc Thielen, Simon Poppinga, Yasaman Tahouni, Dylan Wood, Thorsten Steinberg, Achim Menges, and Thomas Speck. Bio-inspired motion mechanisms: Computational design and material programming of self-adjusting 4d-printed wearable systems. *Advanced Science*, 8(13):2100411, 2021.
- [26] Yasaman Tahouni, Tiffany Cheng, Dylan Wood, Renate Sachse, Rebecca Thierer, Manfred Bischoff, and Achim Menges. Self-shaping curved folding: A 4d-printing method for fabrication of self-folding curved crease structures. In *Symposium on computational fabrication*, pages 1–11, 2020.
- [27] Amirali Nojoomi, Junha Jeon, and Kyungsuk Yum. 2d material programming for 3d shaping. *Nature communications*, 12(1):1–8, 2021.
- [28] Zhen Ding, Oliver Weeger, H Jerry Qi, and Martin L Dunn. 4d rods: 3d structures via programmable 1d composite rods. *Materials & design*, 137:256–265, 2018.
- [29] Yousif Saad Alshebly, Khameel B Mustapha, Ali Zolfagharian, Mahdi Bodaghi, Mohamed Sultan Mohamed Ali, Haider Abbas Almurib, and Marwan Nafea. Bioinspired pattern-driven single-material 4d printing for self-morphing actuators. *Sustainability*, 14(16):10141, 2022.
- [30] Jihyun Ryu, Mehdi Tahernia, Maedeh Mohammadifar, Yang Gao, and Seokheun Choi. Moisture-responsive paper robotics. *Journal of Microelectromechanical Systems*, 29(5):1049–1053, 2020.
- [31] Matteo Pezulla, Gabriel P. Smith, Paola Nardinocchi, and Douglas P. Holmes. Geometry and mechanics of thin growing bilayers. *Soft Matter*, 12(19):4435–4442, 2016.

-
- [32] Basile Audoly and Yves Pomeau. *Elasticity and geometry: from hair curls to the non-linear response of shells*. Oxford university press, 2010.
- [33] Tomohiro Tachi. Origamizing polyhedral surfaces. *IEEE transactions on visualization and computer graphics*, 16(2):298–311, 2009.
- [34] Evgueni T. Filipov, Tomohiro Tachi, and Glaucio H. Paulino. Origami tubes assembled into stiff, yet reconfigurable structures and metamaterials. *Proceedings of the National Academy of Sciences*, 112(40):12321–12326, 2015.
- [35] Koryo Miura. Map fold a la miura style, its physical characteristics and application to the space science. *Research of Pattern Formation*, pages 77–90, 1994.
- [36] Shannon A Zirbel, Brian P Trease, Mark W Thomson, Robert J Lang, Spencer P Magleby, and Larry H Howell. Hanaflex: a large solar array for space applications. In *Micro-and Nanotechnology Sensors, Systems, and Applications VII*, volume 9467, pages 179–187. SPIE, 2015.
- [37] Qiji Ze, Shuai Wu, Jun Nishikawa, Jize Dai, Yue Sun, Sophie Leanza, Cole Zemelka, Larissa S Novelino, Glaucio H Paulino, and Ruike Renee Zhao. Soft robotic origami crawler. *Science advances*, 8(13):eabm7834, 2022.
- [38] Shuai Wu, Qiji Ze, Jize Dai, Nupur Udipi, Glaucio H Paulino, and Ruike Zhao. Stretchable origami robotic arm with omnidirectional bending and twisting. *Proceedings of the National Academy of Sciences*, 118(36):e2110023118, 2021.
- [39] Shuguang Li, Daniel M. Vogt, Daniela Rus, and Robert J. Wood. Fluid-driven origami-inspired artificial muscles. *Proceedings of the National Academy of Sciences*, 114(50):13132–13137, 2017.
- [40] Hillel Aharoni, Desislava V Todorova, Octavio Albarrán, Lucas Goehring, Randall D Kamien, and Eleni Katifori. The smectic order of wrinkles. *Nature communications*, 8(1):15809, 2017.
- [41] Yousra Timounay, Alexander R Hartwell, Mengfei He, D Eric King, Lindsay K Murphy, Vincent Démery, and Joseph D Paulsen. Sculpting liquids with ultrathin shells. *Physical Review Letters*, 127(10):108002, 2021.
- [42] Jérémy Hure, Benoît Roman, and José Bico. Stamping and wrinkling of elastic plates. *Physical review letters*, 109(5):054302, 2012.
- [43] Yigil Cho, Joong-Ho Shin, Avelino Costa, Tae Ann Kim, Valentin Kunin, Ju Li, Su Yeon Lee, Shu Yang, Heung Nam Han, In-Suk Choi, and David J. Srolovitz. Engineering the shape and structure of materials by fractal cut. *Proceedings of the National Academy of Sciences*, 111(49):17390–17395, 2014.
- [44] Paolo Celli, Connor McMahan, Brian Ramirez, Anton Bauhofer, Christina Naify, Douglas Hofmann, Basile Audoly, and Chiara Daraio. Shape-morphing architected sheets with non-periodic cut patterns. *Soft Matter*, 14(48):9744–9749, 2018.
- [45] Ahmad Rafsanjani, Yuerou Zhang, Bangyuan Liu, Shmuel M Rubinstein, and Katia Bertoldi. Kirigami skins make a simple soft actuator crawl. *Science Robotics*, 3(15):eaar7555, 2018.
- [46] Yi Yang, Katherine Vella, and Douglas P Holmes. Grasping with kirigami shells. *Science Robotics*, 6(54):eabd6426, 2021.

References

- [47] Sebastien J.P. Callens and Amir A. Zadpoor. From flat sheets to curved geometries: Origami and kirigami approaches. *Materials Today*, 21(3):241–264, 2018.
- [48] Kyle A Serikawa and Dina F Mandoli. An analysis of morphogenesis of the reproductive whorl of acetabularia acetabulum. *Planta*, 207(1):96–104, 1998.
- [49] Julien Dervaux and Martine Ben Amar. Morphogenesis of growing soft tissues. *Physical review letters*, 101(6):068101, 2008.
- [50] Yael Klein, Efi Efrati, and Eran Sharon. Shaping of elastic sheets by prescription of non-euclidean metrics. *Science*, 315(5815):1116–1120, 2007.
- [51] Jungwook Kim, James A Hanna, Myunghwan Byun, Christian D Santangelo, and Ryan C Hayward. Designing responsive buckled surfaces by halftone gel lithography. *Science*, 335(6073):1201–1205, 2012.
- [52] Limei Huang, Ruiqi Jiang, Jingjun Wu, Jizhou Song, Hao Bai, Bogeng Li, Qian Zhao, and Tao Xie. Ultrafast digital printing toward 4d shape changing materials. *Advanced Materials*, 29(7):1605390, 2017.
- [53] Amirali Nojoomi, Hakan Arslan, Kwan Lee, and Kyungsuk Yum. Bioinspired 3d structures with programmable morphologies and motions. *Nature communications*, 9(1):1–11, 2018.
- [54] Myunghwan Byun, Christian D Santangelo, and Ryan C Hayward. Swelling-driven rolling and anisotropic expansion of striped gel sheets. *Soft Matter*, 9(34):8264–8273, 2013.
- [55] Zi Liang Wu, Michael Moshe, Jesse Greener, Heloise Therien-Aubin, Zhihong Nie, Eran Sharon, and Eugenia Kumacheva. Three-dimensional shape transformations of hydrogel sheets induced by small-scale modulation of internal stresses. *Nature communications*, 4(1):1586, 2013.
- [56] Seog-Jin Jeon, Adam W Hauser, and Ryan C Hayward. Shape-morphing materials from stimuli-responsive hydrogel hybrids. *Accounts of chemical research*, 50(2):161–169, 2017.
- [57] A Sydney Gladman, Elisabetta A Matsumoto, Ralph G Nuzzo, Lakshminarayanan Mahadevan, and Jennifer A Lewis. Biomimetic 4d printing. *Nature materials*, 15(4):413–418, 2016.
- [58] Mark Warner and Eugene Michael Terentjev. *Liquid crystal elastomers*, volume 120. Oxford university press, 2007.
- [59] Cyrus Mostajeran, Mark Warner, Taylor H Ware, and Timothy J White. Encoding gaussian curvature in glassy and elastomeric liquid crystal solids. *Proceedings of the Royal Society A: Mathematical, Physical and Engineering Sciences*, 472(2189):20160112, 2016.
- [60] Michael E McConney, Angel Martinez, Vincent P Tondiglia, Kyung Min Lee, Derrick Langley, Ivan I Smalyukh, and Timothy J White. Topography from topology: photoinduced surface features generated in liquid crystal polymer networks. *Advanced Materials*, 25(41):5880–5885, 2013.
- [61] Paul Plucinsky, Marius Lemm, and Kaushik Bhattacharya. Programming complex shapes in thin nematic elastomer and glass sheets. *Physical Review E*, 94(1):010701, 2016.
- [62] Morgan Barnes, Seyed M. Sajadi, Shaan Parekh, Muhammad M. Rahman, Pulickel M. Ajayan, and Rafael Verduzco. Reactive 3d printing of shape-programmable liquid crystal elastomer actuators. *ACS Applied Materials Interfaces*, 12(25):28692–28699, 2020.

- [63] Cedric P Ambulo, Julia J Burroughs, Jennifer M Boothby, Hyun Kim, M Ravi Shankar, and Taylor H Ware. Four-dimensional printing of liquid crystal elastomers. *ACS applied materials & interfaces*, 9(42):37332–37339, 2017.
- [64] Arda Kotikian, Ryan L Truby, John William Boley, Timothy J White, and Jennifer A Lewis. 3d printing of liquid crystal elastomeric actuators with spatially programed nematic order. *Advanced materials*, 30(10):1706164, 2018.
- [65] Ron Pelrine, Roy Kornbluh, Qibing Pei, and Jose Joseph. High-speed electrically actuated elastomers with strain greater than 100%. *Science*, 287(5454):836–839, 2000.
- [66] Christoph Keplinger, Martin Kaltenbrunner, Nikita Arnold, and Siegfried Bauer. Röntgen’s electrode-free elastomer actuators without electromechanical pull-in instability. *Proceedings of the National Academy of Sciences*, 107(10):4505–4510, 2010.
- [67] Jiangshui Huang, Tiefeng Li, Choon Chiang Foo, Jian Zhu, David R Clarke, and Zhigang Suo. Giant, voltage-actuated deformation of a dielectric elastomer under dead load. *Applied Physics Letters*, 100(4):041911, 2012.
- [68] Ehsan Hajiesmaili and David R Clarke. Reconfigurable shape-morphing dielectric elastomers using spatially varying electric fields. *Nature communications*, 10(1):1–7, 2019.
- [69] R Ortigosa and J Martínez-Frutos. Topology optimisation of stiffeners layout for shape-morphing of dielectric elastomers. *Structural and Multidisciplinary Optimization*, 64(6):3681–3703, 2021.
- [70] Ehsan Hajiesmaili, Natalie M Larson, Jennifer A Lewis, and David R Clarke. Programmed shape-morphing into complex target shapes using architected dielectric elastomer actuators. *Science Advances*, 8(28):eabn9198, 2022.
- [71] David Cadogan, William Graham, and Timothy Smith. Inflatable and rigidizable wings for unmanned aerial vehicles. In *2nd AIAA "Unmanned Unlimited" Conf. and Workshop & Exhibit*, page 6630, 2003.
- [72] Ignacio Andrade-Silva and Joel Marthelot. Fabric-based star soft robotic gripper. *arXiv preprint arXiv:2209.02491*, 2022.
- [73] Shuguang Li, John J Stampfli, Helen J Xu, Elian Malkin, Evelin Villegas Diaz, Daniela Rus, and Robert J Wood. A vacuum-driven origami “magic-ball” soft gripper. In *2019 International Conference on Robotics and Automation (ICRA)*, pages 7401–7408. IEEE, 2019.
- [74] Eric Brown, Nicholas Rodenberg, John Amend, Annan Mozeika, Erik Steltz, Mitchell R. Zakin, Hod Lipson, and Heinrich M. Jaeger. Universal robotic gripper based on the jamming of granular material. *Proceedings of the National Academy of Sciences*, 107(44):18809–18814, 2010.
- [75] Emmanuel Siéfert. *Inflating to shape: from soft architected elastomers to patterned fabric sheets*. PhD thesis, Sorbonne université, 2019.
- [76] Emmanuel Siéfert, Etienne Reyssat, José Bico, and Benoît Roman. Bio-inspired pneumatic shape-morphing elastomers. *Nature materials*, 18(1):24–28, 2019.
- [77] Emmanuel Siéfert and Mark Warner. Inflationary routes to gaussian curved topography. *Proceedings of the Royal Society A*, 476(2240):20200047, 2020.
- [78] Emmanuel Siéfert, Etienne Reyssat, José Bico, and Benoît Roman. Programming stiff inflatable shells from planar patterned fabrics. *Soft Matter*, 16(34):7898–7903, 2020.

References

- [79] Tian Gao, Emmanuel Siéfert, Antonio DeSimone, and Benoît Roman. Shape programming by modulating actuation over hierarchical length scales. *Advanced Materials*, 32(47):2004515, 2020.
- [80] Julian Panetta, Florin Isvoranu, Tian Chen, Emmanuel Siéfert, Benoît Roman, and Mark Pauly. Computational inverse design of surface-based inflatables. *ACM Transactions on Graphics (TOG)*, 40(4):1–14, 2021.
- [81] Lishuai Jin, Antonio Elia Forte, Bolei Deng, Ahmad Rafsanjani, and Katia Bertoldi. Kirigami-inspired inflatables with programmable shapes. *Advanced Materials*, 32(33):2001863, 2020.
- [82] Ruslan Guseinov, Connor McMahan, Jesús Pérez, Chiara Daraio, and Bernd Bickel. Programming temporal morphing of self-actuated shells. *Nature communications*, 11(1):237, 2020.
- [83] Tian Chen, Julian Panetta, Max Schnaubelt, and Mark Pauly. Bistable auxetic surface structures. *ACM Transactions on Graphics*, 40(4):1–9, 2021.
- [84] Tian Chen and Kristina Shea. Computational design of multi-stable, reconfigurable surfaces. *Materials Design*, 205:109688, 2021.
- [85] Lu Liu, Chuan Qiao, Haichao An, and Damiano Pasini. Encoding kirigami bi-materials to morph on target in response to temperature. *Scientific reports*, 9(1):1–14, 2019.
- [86] J. William Boley, Wim M. van Rees, Charles Lissandrello, Mark N. Horenstein, Ryan L. Truby, Arda Kotikian, Jennifer A. Lewis, and L. Mahadevan. Shape-shifting structured lattices via multimaterial 4d printing. *Proceedings of the National Academy of Sciences*, 116(42):20856–20862, 2019.
- [87] Marius Wagner, Tian Chen, and Kristina Shea. Large shape transforming 4d auxetic structures. *3D printing and Additive Manufacturing*, 4(3):133–142, 2017.
- [88] R.C. Hosney, K. Zeleznak, and A. Abdelrahman. Mechanism of popcorn popping. *Journal of Cereal Science*, 1(1):43–52, 1983.
- [89] Emmanuel Virost and Alexandre Ponomarenko. Popcorn: critical temperature, jump and sound. *Journal of The Royal Society Interface*, 12(104):20141247, 2015.
- [90] TK Taewee. Cracker “keropok”: A review on factors influencing expansion. *International Food Research Journal*, 18(3):855–866, 2011.
- [91] Wen Wang, Lining Yao, Teng Zhang, Chin-Yi Cheng, Daniel Levine, and Hiroshi Ishii. Transformative appetite: shape-changing food transforms from 2d to 3d by water interaction through cooking. In *Proceedings of the 2017 CHI conference on human factors in computing systems*, pages 6123–6132, 2017.
- [92] S. Cafieri, M. Mastromatteo, S. Chillo, and M.A. Del Nobile. Modeling the mechanical properties of pasta cooked at different times. *Journal of Food Engineering*, 100(2):336–342, 2010.
- [93] Burebi Yiming, Tao Liu, Guodong Nian, Zilong Han, Zheng Jia, and Shaoxing Qu. Mechanics-guided design of shape-morphing composite sheets with hard and soft materials. *Extreme Mechanics Letters*, 35:100643, 2020.
- [94] Qingrui Wang, Xiaoyong Tian, Lan Huang, Dichen Li, Andrei V. Malakhov, and Alexander N. Polilov. Programmable morphing composites with embedded continuous fibers by 4d printing. *Materials Design*, 155:404–413, 2018.
- [95] Darcy Wentworth Thompson. *On growth and form*, volume 2. Cambridge university press Cambridge, 1942.

-
- [96] Loïc D'eraimo, Benjamin Chollet, Marie Leman, Ekkachai Martwong, Mengxing Li, Hubert Geisler, Jules Dupire, Margaux Kerdraon, Clémence Vergne, Fabrice Monti, et al. Microfluidic actuators based on temperature-responsive hydrogels. *Microsystems & Nanoengineering*, 4(1):1–7, 2018.
- [97] Frédéric Tayeb, Baptiste Lefevre, Olivier Baverel, Jean-François Caron, and Lionel Du Peloux. Design and realisation of composite gridshell structures. *Journal of the International Association for Shell and Spatial Structures*, 56(1):49–59, 2015.
- [98] Eike Schling, Denis Hitrec, Jonas Schikore, and Rainer Barthel. Design and construction of the asymptotic pavilion. In *VIII International Conference on Textile Composites and Inflatable Structures. STRUCTURAL MEMBRANES 2017. Barcelona: International Center for Numerical Methods in Engineering (CIMNE)*, pages S–178, 2017.
- [99] Changyeob Baek, Andrew O. Sageman-Furnas, Mohammad K. Jawed, and Pedro M. Reis. Form finding in elastic gridshells. *Proceedings of the National Academy of Sciences*, 115(1):75–80, 2017.
- [100] Xiaonan Hou and Vadim V. Silberschmidt. Metamaterials with negative poisson's ratio: a review of mechanical properties and deformation mechanisms. In *Mechanics of Advanced Materials*, pages 155–179. Springer International Publishing, 2015.
- [101] Corentin Coulais, Alberico Sabbadini, Fré Vink, and Martin van Hecke. Multi-step self-guided pathways for shape-changing metamaterials. *Nature*, 561(7724):512–515, 2018.
- [102] Yongkang Jiang, Diansheng Chen, Che Liu, and Jian Li. Chain-like granular jamming: a novel stiffness-programmable mechanism for soft robotics. *Soft robotics*, 6(1):118–132, 2019.
- [103] Jan Koenderink and Andrea van Doorn. Shape from chebyshev nets. In *European Conference on Computer Vision*, pages 215–225. Springer, 1998.
- [104] F Otto, J Henniecke, and K Matsushita. II10 gitterschalen. *Institut für leichte Flächentragwerke (IL)*, 1974.
- [105] Lina Bouhaya, Olivier Baverel, and Jean-François Caron. Mapping two-way continuous elastic grid on an imposed surface: Application to grid shells. In *IASS 2009: Evolution and Trends in Design, Analysis and Construction of Shell and Spatial Structures*, pages 989–998, 2009.
- [106] Lionel Du Peloux, Olivier Baverel, Jean-François Caron, and Frédéric Tayeb. From shape to shell: a design tool to materialize freeform shapes using gridshell structures. In *Design Modelling Symposium Berlin*, 2013.
- [107] Lorna J. Gibson and Michael F. Ashby. *Cellular solids*. 1997.
- [108] Basile Audoly and Sébastien Neukirch. A one-dimensional model for elastic ribbons: a little stretching makes a big difference. *Journal of the Mechanics and Physics of Solids*, 153:104457, 2021.
- [109] Albert Edward Green. The equilibrium and elastic stability of a thin twisted strip. *Proceedings of the Royal Society of London. Series A-Mathematical and Physical Sciences*, 154(882):430–455, 1936.
- [110] Arthur Lebée and Karam Sab. Homogenization of a space frame as a thick plate: Application of the bending-gradient theory to a beam lattice. *Computers & Structures*, 127:88–101, 2013.

References

- [111] José Bico, Étienne Reyssat, and Benoît Roman. Elastocapillarity: When Surface Tension Deforms Elastic Solids. *Annual Review of Fluid Mechanics*, 50(1):629–659, 2018.
- [112] M. E. R. Shanahan and A. Carre. Viscoelastic dissipation in wetting and adhesion phenomena. *Langmuir*, 11(4):1396–1402, 1995.
- [113] Benoit Roman and José Bico. Elasto-capillarity: deforming an elastic structure with a liquid droplet. *Journal of Physics: Condensed Matter*, 22(49):493101, 2010.
- [114] José Bico, Benoît Roman, Loic Moulin, and Arezki Boudaoud. Elastocapillary coalescence in wet hair. *Nature*, 432(7018):690–690, 2004.
- [115] Xavier Noblin, Jared Westbrook, Nicolas Rojas, Médéric Argentina, and Jacques Dumais. Biomechanics of fern spores discharge: the sporangium opening. In *Proceedings of the 6th Plant Biomechanics Conference. Cayenne: Ecofog*, pages 179–86, 2009.
- [116] Ruba T Borno, Joseph D Steinmeyer, and Michel M Maharbiz. Transpiration actuation: the design, fabrication and characterization of biomimetic microactuators driven by the surface tension of water. *Journal of Micromechanics and Microengineering*, 16(11):2375–2383, 2006.
- [117] Charlotte Py, Paul Reverdy, Lionel Doppler, José Bico, Benoît Roman, and Charles N. Baroud. Capillary Origami: Spontaneous Wrapping of a Droplet with an Elastic Sheet. *Physical Review Letters*, 98(15):156103, 2007.
- [118] Aisa Biria and Eliot Fried. Theoretical and experimental study of the stability of a soap film spanning a flexible loop, 2015. arXiv:1412.1210 [cond-mat].
- [119] Luca Giomi and Lakshminarayanan Mahadevan. Minimal surfaces bounded by elastic lines. *Proceedings of the Royal Society A: Mathematical, Physical and Engineering Sciences*, 468(2143):1851–1864, 2012.
- [120] Finn Box, Ousmane Kodio, Doireann O’Kiely, Vincent Cantelli, Alain Goriely, and Dominic Vella. Dynamic Buckling of an Elastic Ring in a Soap Film. *Physical Review Letters*, 124(19):198003, 2020.
- [121] Manon Jouanlanne, Antoine Egelé, Damien Favier, Wiebke Drenckhan, Jean Farago, and Aurélie Hourlier-Fargette. Elastocapillary deformation of thin elastic ribbons in 2d foam columns. *Soft Matter*, 18(12):2325–2331, 2022.
- [122] Shucong Li, Bolei Deng, Alison Grinthal, Alyssa Schneider-Yamamura, Jinliang Kang, Reese S. Martens, Cathy T. Zhang, Jian Li, Siqin Yu, Katia Bertoldi, and Joanna Aizenberg. Liquid-induced topological transformations of cellular microstructures. *Nature*, 592(7854):386–391, 2021.
- [123] Zachary A Zell, SiYoung Q Choi, L Gary Leal, and Todd M Squires. Microfabricated deflection tensiometers for insoluble surfactants. *Applied physics letters*, 97(13):133505, 2010.
- [124] N Adami and H Caps. Surface tension profiles in vertical soap films. *Physical Review E*, 91(1):013007, 2015.

Appendix A

Code for sample drawing

A.1 Code for blockers

In order for the cells to only squeeze a certain amount, blockers are added. Three triangles that interlock are drawn inside half a diamond. There are different ways of designing such diamonds. Knowing the initial and final angle of the diamonds, only three other parameters are required [A.1](#).

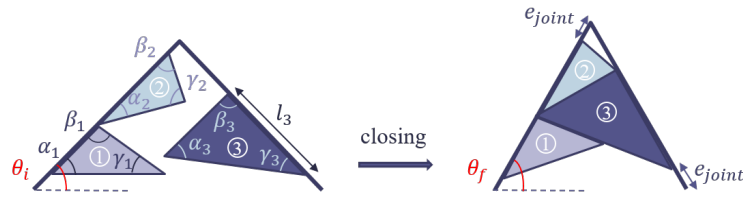


Figure A.1 Scheme for the construction of the blockers. Half of the diamond in its open state on the left and in its final state on the right

To have the final diamond as full of material as possible, α_1 has to be as large as possible. The limitation comes from the fact that in the open state, the tip of triangle 1 should not be in the other half of the diamond. α_1 is thus set to θ_i . For convenience, the two other values taken are γ_3 and l_3 .

Knowing all this values, the other can be deduced.

$$\alpha_1 + \beta_1 + \gamma_1 = 180 \quad (\text{A.1})$$

$$\alpha_2 + \beta_2 + \gamma_2 = 180 \quad (\text{A.2})$$

$$\alpha_3 + \beta_3 + \gamma_3 = 180 \quad (\text{A.3})$$

$$\beta_1 + \alpha_2 + \alpha_3 = 180 \quad (\text{A.4})$$

$$\alpha_2 + \theta_f = \beta_3 \quad (\text{A.5})$$

$$(\text{A.6})$$

A.2 Code for axisymmetric case

A.2.1 Construction of logarithmic spiral

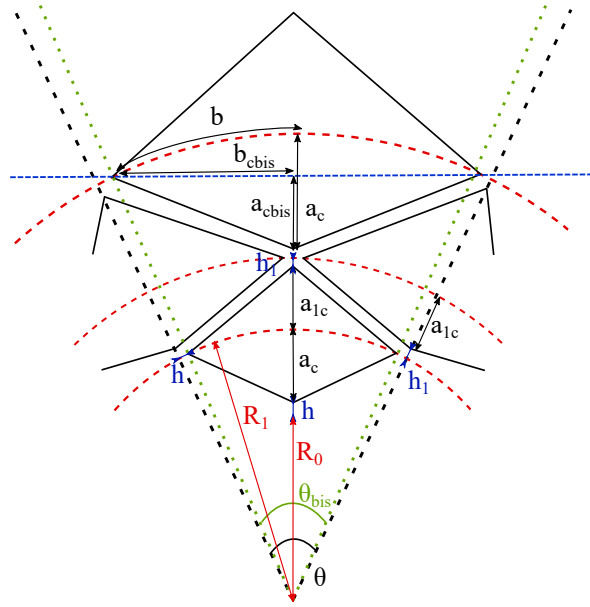


Figure A.2 Scheme for the construction of the diamonds in the case of the axisymmetric shapes

$2b$ is the distance between the two sides of the diamond along the arc of circle. e_p is the thickness of the diamonds and h the distance between the diamonds vertically and horizontally. e_p has a linear dependency with the length of the diamonds side. $e_p = \alpha l$ with $l = b\sqrt{C^2 + 1}$ and $h = Ae_p$, thus:

$$h = A\alpha b\sqrt{C^2 + 1} \quad (\text{A.7})$$

Looking at the scheme A.2, this equation can be derived:

$$(2b + 2h) = (R + h + a_c)\theta \quad (\text{A.8})$$

$$(2b + 2A\alpha b\sqrt{C^2 + 1}) = (R + A\alpha b\sqrt{C^2 + 1} + Cb)\theta \quad (\text{A.9})$$

Thus

$$b = \frac{R\theta}{2 - C\theta + A\alpha(2 - \theta)\sqrt{C^2 + 1}} \quad (\text{A.10})$$

and then $R_1 = R + h + a_c$ with $a_c = Cb$

The operation is repeated for the second ring of diamonds that are is shifted of half a diamond.

In reality the length of the diamonds side is not $l = b\sqrt{C^2 + 1}$ but $l_c = \frac{a_{cbis}}{b_{cbis}}$ with a_{cbis} and b_{cbis} respectively the half vertical and horizontal straight diagonal.

Moreover from one ring to another a_c is conserve between the half top of the lower diamond and the half bottom of the higher diamond (see A.2). Indeed, all the point are set in a way that every summit and the center of the diamond of the next ring are aligned on the same circle centered at the center of the figure.

When one portion is drawn, it is then repeated $N = \frac{\theta}{360}$ times.

This description of the drawing can be used to designed the desired shapes. $a_c, a_{c1} \dots$ correspond to the open diamond. When they are closed, the a_{cfin} measured is different and the summit of the diamonds are aligned on a different circle with radius R_f

A.2.2 Algorithm axisymmetric shapes

Once the logarithmic spiral is drawn, the blockers with a specific size have to be drawn. A function takes the profile and the positions of specific points to determine the strain to apply in each diamonds. Every length used here correspond to the final state when the diamonds are closed.

Inputs:

- *profile* : discrete or continuous profile of the desired shape ($Rbis, Ht$).
- $Rbis_i, Ht_i$: coordinate of the initial point on the profile.
- $H1$: correspond to h the distance in between diamonds.
- n : number of diamonds per ring.
- $l1, l2$: the upper and lower side of the diamond.
- $af1$: the final length of the upper half diagonal of the diamonds from the previous ring.
- $Rf1$: length from the center of the sample to the initial point.
- j : taken into account when the number of diamonds is doubled not to have too big diamonds

Outputs:

- $af2$: length of the upper vertical half of the actual diamond from the arc of circle.
- $Rbis_{f1}, Ht_{f1}$: coordinate on the profile of the upper corner of the diamond.
- $bf, bbisf$: respectively the final distance of the half horizontal diagonal as an arc of circle and straight line.
- $abisf1, abisf2$: respectively the lower and upper vertical half of the diamonds taken from $bbisf$.
- $Rf2$: length from the center of the sample to the upper corner of the diamond.

Code for sample drawing

In the function the point closer to the center is supposed fixed, all the other move when the cells close. The function take the initial point on the profile, the lower vertical half diagonal is know from the previous ring. With this length a new point is created of the profile, it determines a strain for the selected ring. Knowing the strain for the cell, the length of the upper half vertical diagonal can be calculated and positioned on the profile.

Going from a ring to another, every diamonds can be created and the final shape can be obtained. When the strain for every ring is known, it can be converted to a size of blockers thanks to the code detailed just before.

RÉSUMÉ

Des matériaux qui seraient capables de changer de forme par eux-mêmes peuvent trouver des applications dans de nombreux domaines technologiques. Par exemple, en "soft robotics", où changer de forme de manière continue permet d'attraper des objets fragiles, de se faufiler dans des espaces difficiles d'accès ou d'assister des opérations chirurgicales. Mais le passage d'une surface plane à une forme en trois dimensions ne peut se faire qu'à des conditions géométriques bien précises : il n'est pas possible de changer la courbure de Gauss d'une surface sans modifier les distances dans son plan. Il est ainsi possible d'utiliser cette propriété pour changer de forme en variant localement la direction et/ou l'intensité de déformations spontanées. Dans ce travail de thèse, nous avons développé des solutions simples pour créer des objets plans capables de changer de forme, en utilisant des matériaux actifs (capables de se déformer en réponse à un stimulus), et en contraignant leur déformation par couplage avec des structures déformables obtenues par des méthodes de prototypage rapide (impression 3D, découpeuse laser...). Nous avons pour cela utilisé des structures cellulaires (contenant un motif qui se répète) dans différentes configurations. Dans un premier temps, un mélange élastomère/éthanol a été utilisé comme matrice active qui gonfle quand elle est chauffée. De fins réseaux cellulaires inextensibles ont été emprisonnés dans cette matrice pour contraindre son gonflement dans certaines directions de l'espace et induire un changement de forme. Dans une deuxième partie, au lieu d'utiliser une matrice extérieure comme moteur de la déformation (croissance/rétrécissement), des réseaux plus épais (~ 1cm) sont directement actionnés. Pour changer de forme, les cellules de ces structures sont fermées, soit en y faisant le vide, soit en utilisant des fils tendus à travers la structure. Enfin, dans un dernier temps, des réseaux cellulaires fins sont actionnés par des films de savon, la tension de surface permettant la fermeture des cellules. Dans les trois cas, la présence de réseaux cellulaires permet de programmer localement l'intensité ou la direction de la déformation des structures planes pour en faire des formes 3D. Des formes simples comme des cônes ou des anti-cônes ont été obtenues avec les trois techniques. De plus, dans le cas des structures plus épaisses actionnées par des fils, il est aussi possible d'obtenir des formes plus complexes et de résoudre le problème inverse dans certains cas (programmer la forme finale dans le design initial).

MOTS CLÉS

élasticité, géométrie, matériaux programmables, changement de forme

ABSTRACT

Materials that are able to change shape by themselves find applications in many fields. For example, in soft robotics, where changing shape in a continuous way allows to catch fragile objects, to sneak into narrow spaces or to assist surgical operations. But the change from a flat surface to a three-dimensional shape can only be done under specific geometrical conditions: it is not possible to change the Gaussian curvature of a surface without changing the distances in its plane. It is thus possible to use this property to change shape by locally varying the direction and/or intensity of spontaneous deformations. In this thesis, we have developed simple solutions to create planar objects capable of shape changing, by using simple active materials (deforming in response to a stimulus), and by constraining their deformation by coupling them to deformable structures obtained by rapid prototyping methods (3D printing, laser cutter...). We have used cellular structures (containing a repeating pattern) in different configurations. In a first part, an elastomer/ethanol mixture has been used as an active matrix which swells when heated. Thin inextensible cellular networks trapped in this matrix constrain its swelling in certain spatial directions and allow for shape change. In a second part, instead of using an external matrix as a driver for deformation (growth/shrinkage), thicker networks (~ 1cm) were directly actuated. To change shape, cells of these structures were closed, either by using a vacuum pump or by using wires stretched across the structure. Finally, in a last part, thin cellular networks were actuated by soap films, the surface tension allowing the closure of the cells. In all three cases, the presence of cellular networks allowed to locally program the density or direction of the deformation of the planar structures into 3D shapes. Simple shapes such as cones or anti-cones were obtained with the three techniques. Moreover, in the case of thicker structures driven by wires, it is also possible to obtain more complex shapes and to solve the inverse problem in some cases (programming the final shape in the initial design).

KEYWORDS

elasticity, geometry, morphable materials, shape changing